# A PETROLOGIC STUDY OF BASALTS FROM THE MAGIC MOUNTAIN HYDROTHERMAL AREA, SOUTHERN EXPLORER RIDGE, NORTHEAST PACIFIC OCEAN

by

GREGORY THOMAS FRANCIS SHEA

B.Sc.(Honours), University of Western Ontario

A THESIS SUBMITTED IN PARTIAL FULFILMENT OF

THE REQUIREMENTS FOR THE DEGREE OF

MASTER OF SCIENCE

in

THE FACULTY OF GRADUATE STUDIES

Department of Geological Sciencies

We accept this thesis as conforming

to the required standard

THE UNIVERSITY OF BRITISH COLUMBIA

April 1987

In presenting this thesis in partial fulfilment of the requirements for an advanced degree at the University of British Columbia, I agree that the Library shall make it freely available for reference and study. I further agree that permission for extensive copying of this thesis for scholarly purposes may be granted by the head of my department or by his or her representatives. It is understood that copying or publication of this thesis for financial gain shall not be allowed without my written permission.

Department of Geological Sciences.

The University of British Columbia
1956 Main Mall
Vancouver, Canada
V6T 1Y3

Date April 27, 1987.

## Abstract

The Magic Mountain Hydrothermal Area (MMA) is a 5 km portion of the Southern Explorer Ridge (SER) centered at 49°46′ and 130°20′W. It is a region of active hydrothermal activity located near the culmination of an unusually high standing spreading centre.

Seafloor photographs, conductivity-temperature surveys and acoustic images have been used to determine the nature and extent of axial volcanism and tectonism as well as the associated hydrothermal activity. Major element and trace element whole rock analyses were obtained by x-ray flourescence spectrometry (XRF) for 25 recently formed basalts collected by submersible from the MMA. These were compared with analyses of basalts dredged from other locations on the ridge axis. The mineral phases of selected samples were analysed by electron microprobe.

Basalt chemical variations observed along axis reveal that some of the MMA samples are the most highly fractionated and incompatible-element-enriched basalts so far obtained from the SER. These trends, along with variations in ridge morphology and lava flow type, indicate that the volcanism of the MMA is affected by a hot spot centred at the axial topographic high five km to the north. This hot spot may be associated with the propagation of the ridge segment.

Several quantitative tests of fractional crystallization indicate that the 25 MMA basalts represent at least 13 discrete lavas derived from at least 5 distinct source magmas. Mixing between magmas is indicated by disequilibrium mineral textures and compositions observed in some samples.

A relationship between hot spot activity and degree of magmatism with the location and duration of axial hydrothermal activity on spreading centres is indicated by these findings. Further investigation of these relationships as well as the

relationship between the tectonic processes of ridge propagation and hot spot activity is recommended.

Table of Contents

## LIST OF TABLES

Table Page

## LIST OF FIGURES

Figure Page

Acknowledgements

In coming to the land of the lotus eaters, I was struck by much of its fabled beauty ... the sea, the mountains, the flowers. The most unexpected and greatest pleasure was the opportunity to meet and work with some very fine people. I would like to express my gratitude to Dr. R. L. (Dick) Chase for taking me on, both as a student and a friend. Both he and his family provided much encouragement and moral support. Financial support was generously provided from an NSERC strategic grant jointly administered by Dr. Chase and Dr. S. D. Scott of the University of Toronto.

I am greatful to Drs. Kelly Russell and Peter Michael for their insights and for their patience in rendering unto me some 'secrets of the petrology trade'. For my data collection and analysis, I was lucky to be guided by a number of skillful craftsmen; thanks to Drs. Dick Armstrong, Cathy Hickson and Stanya Horsky. The geology department is blessed with a first rate technical staff: thanks to Duke, Doug, Ed, Gord, John, Mark, Ray and Yvonne and all the office staff.

My primary fuel was the support of my friends; many thanks to Urs 'the swiss hockey puck', Dave 'the wandering leprechaun', M.C., Cliff, Pat, Joe, Maureen, Liz, Wendy, Al and the rest of the St. Ignatius crew. Thanks most of all to my most supportive and inspiring friends, my folks.

# 1. INTRODUCTION

## 1.1 LOCATION AND ACCESS

The Southern Explorer Ridge (SER) is an unusually high standing mid-oceanic spreading centre located in the North-East Pacific Ocean, approximately 250 km off the west coast of Vancouver Island, British Columbia (figure 1).

In the summer of 1984, the third in a series of expeditions by project CASM (Canadian-American Sea Mount) was undertaken to survey the topographic high of the ridge crest. Hydrothermal waters were detected and massive sulphide deposits were photographed in the vicinity of the culmination (Chase *et al.*, 1984). During the same summer, two follow-up expeditions to the area were undertaken with the Canadian submersible PISCES 4; the SCHISM expedition in June (Tunnicliffe *et al.*, 1986) and the CASM 4 expedition in August (Scott *et al.*, 1985). All dives were made along a 6 kilometer portion of the ridge axis, in the area where hydrothermal vent waters were detected, centred at 49°46′ N and 130°20′ W.

The area covered during these dives comprised the study area of this thesis. During these dives, many hydrothermal vents and associated base metal massive sulphide deposits were discovered and sampled. Sixty of these deposits have been observed or photographed in the area to date. These deposits are being studied by Dr. Steven Scott and associates at the University of Toronto.

The first large active hydrothermal vent field encountered was dominated by a ten metre tall 'black smoker' from which fluids issued with temperatures in excess of 250°C. This spectacular structure was named the 'Magic Mountain Vent' by Tunnicliffe *et al.* (1986). Consequently, the study area is referred to as the Magic Mountain Area (MMA). Twenty four basalt fragments were collected during the dives to the MMA. These samples, along with a basalt that fell into the camera frame

during a photo run (sample CASM-3) constitute the samples of the study suite (see Chapter 3).

## 1.2 PREVIOUS INVESTIGATIONS

The history of investigation in the Explorer region can be conveniently separated into two phases; the period before and the period after the release of high-resolution SEABEAM bathymetry maps in the spring of 1984 (Malahoff *et al.*, 1984, figure 3). In the previous 15 years, intermittent and independent geological and geophysical studies had been undertaken by various groups. The understanding of the geology and tectonics of the area prior to the release of the SEABEAM data is found in papers by Chase *et al.* (1975) and Riddihough (1977, 1984) Geophysical surveys of the region included magnetic, bathymetric, gravity, heat flow and seismic refraction studies (Srivastava 1973, Tiffin and Seemann 1975, Malacek and Clowes 1978, Hyndman *et al.* 1978, and Lister 1972). The petrology and geochemistry of the basalts dredged from the region between 1969 and 1979 is described in a MSc thesis by B.L. Cousens (1982) and by Cousens *et al.* (1984).

With the release of the SEABEAM bathymetry (contour interval=10m), it became obvious that the region had a much more varied topography and convoluted tectonic history than had been envisioned from the lower resolution bathymetry of Tiffin *et al.* (1975, contour interval=100m). The SEABEAM bathymetry revealed that a substantial part of the northern portion of the SER was less than 2000 m deep and was thus accessable to the PISCES 4 submersible. This, coupled with the fact that extensive hydrothermal activity had previously been observed on topographic highs on other spreading centres (see Chapter 6) led to the investigation for hydrothermal activity described previously.

## 1.3 PURPOSE OF STUDY

The present study involves the description and petrologic modelling of a series of fresh basalt samples collected by submersible from a portion of a volcanically active mid-ocean ridge axis. It is similar in nature, although much smaller in scale to studies on the Mid-Atlantic Ridge (Stakes *et al.*, 1984), the East Pacific Rise (Ballard *et al.*, 1981) and the Galapagos Spreading Centre (Byerly, 1980 and Perfit and Fornari, 1983).

The objectives of this study are:

1. Description of the chemical and petrographic variations of the lavas in the MMA.
2. Elucidation of some petrologic processes that may account for these variations.
3. Discussion of the relationships between the petrologic processes and tectonic processes and hydrothermal activity.

# 2. GEOLOGICAL SETTING

## 2.1 REGIONAL SETTING AND TECTONIC HISTORY

The regional setting of the SER is illustrated in figure 1. The SER, separating the Pacific Plate to the west and the Explorer microplate to the east, is one of a series of spreading centres constituting the Juan de Fuca System. From south to north, each segment of this system is variably displaced westward by transform faults and rotated clockwise as the system comes into closer proximity with the North American Plate. The proximity of the spreading centre to the convergent continental margin has resulted in complex translational and rotational movements of the plates.

### *Tectonic History*

Riddihough (1977, 1984) attempted to reconstruct recent plate movements by re-evaluating the data of the pioneering magnetic survey of Raff and Mason (1961). In Riddihough's model, the Explorer Ridge became separated from the Juan de Fuca Ridge at the initiation of the Sovanco Fracture Zone (see figure 1) about 8 Ma BP. Eventually, with the initiation of the Nootka Fault at between 3 and 4 Ma BP, the Explorer Plate became decoupled from the Juan de Fuca Plate. Subsequently, the rate of convergence of the Explorer Plate with North America decreased progressively from 50 mm/yr to about 25 mm/yr at the last measured epoch at 0.5 Ma. During this time, there was also a rapid decrease in the calculated spreading rate of the SER. The present direction of convergence of the Explorer Microplate with North America is calculated to be N 6°E. The rate of convergence is calculated to be 14 mm/yr.

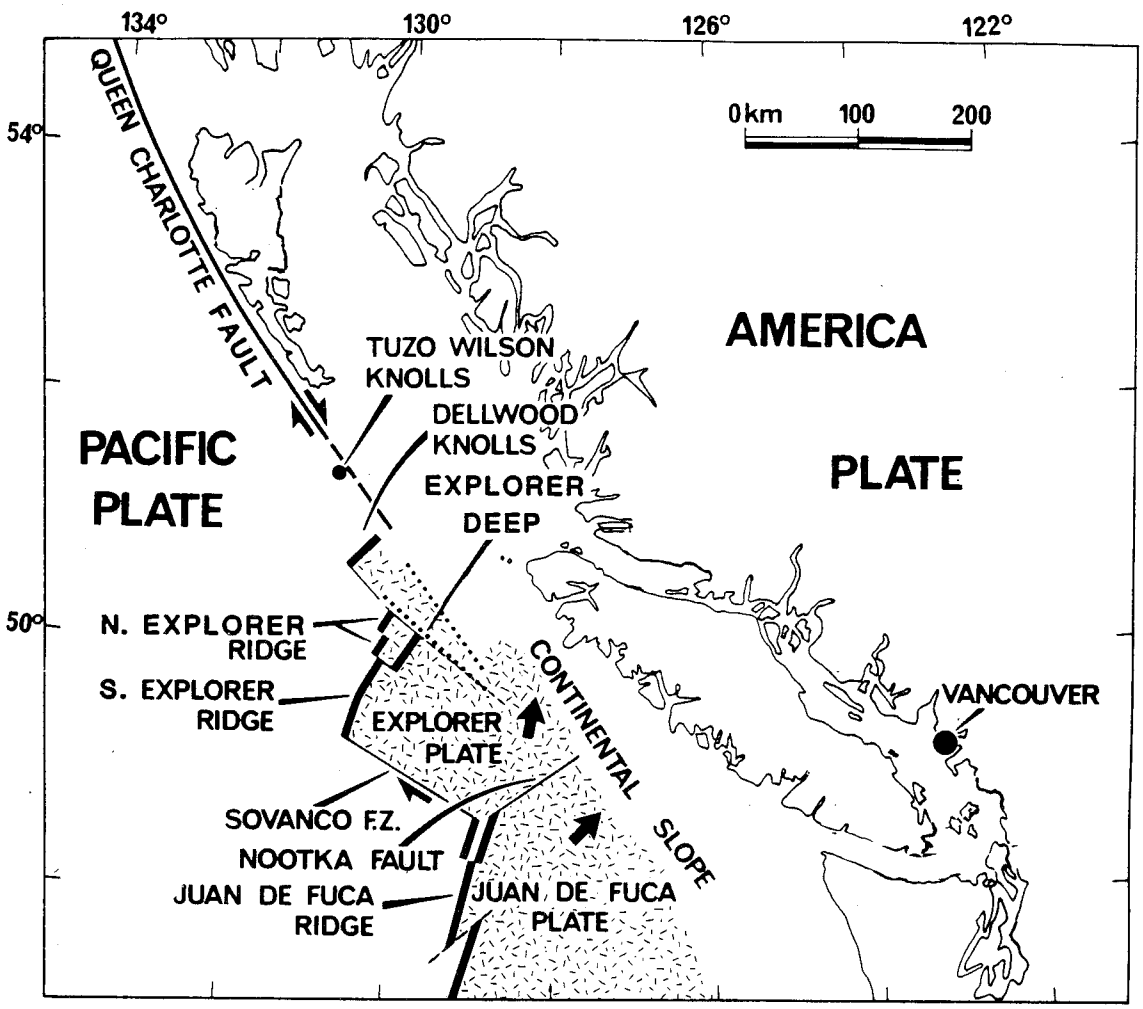


Figure 1: Major tectonic features of the northern Juan de Fuca Ridge system (modified from Davis *et al.*, 1984).

Riddihough (1984) explained these phenomena as an example of pivotal subduction (Menard, 1978) in which small plate systems, like the Juan de Fuca system, encounter the greatest resistance to subduction at the point where the youngest and thus warmest and most buoyant crust is being subducted. Thus, as the Explorer Plate became decoupled from the Juan de Fuca Plate, it no longer was subject to the pull of the larger, older (and thus cooler and more dense) Juan de Fuca Plate of the south.

A more detailed account of the tectonic evolution of the Explorer region is presented by Botros *et al.* (1986) and Botros and Johnson (*in review*). This study is based on new magnetic data along with SEABEAM (Malahoff *et al.*, 1984) and SeaMARC II side scan sonar data (Davis *et al.*, 1985).

Six stages in the evolution of the region are represented by diagrams in figure 2. There is close agreement with Riddihough's (1984) calculations for the time of the initiation of the Sovanco Fracture Zone (SFZ in fig. 2) at 7.4 Ma and the Nootka Fault (NF) at 4 Ma BP.

This model provides a more detailed account of complexities such as rate and asymmetry of axial spreading (indicated by the large arrows in fig. 2), and rate and direction of propagation (small dark arrows), and ridge segmentation. Between 4.8 and 2.5 Ma BP the Explorer Ridge is made up of three spreading segments. Each of these three segments undergoes a different subsequent development.

The southernmost, the Explorer Seamount Segment (ESS), was isolated from the system as the SFZ rotated clockwise and migrated north. This occured in responce to the strain resulting from a large 12° difference in azimuth of the Explorer and Juan de Fuca Ridges (Botros and Johnson, *in review*).

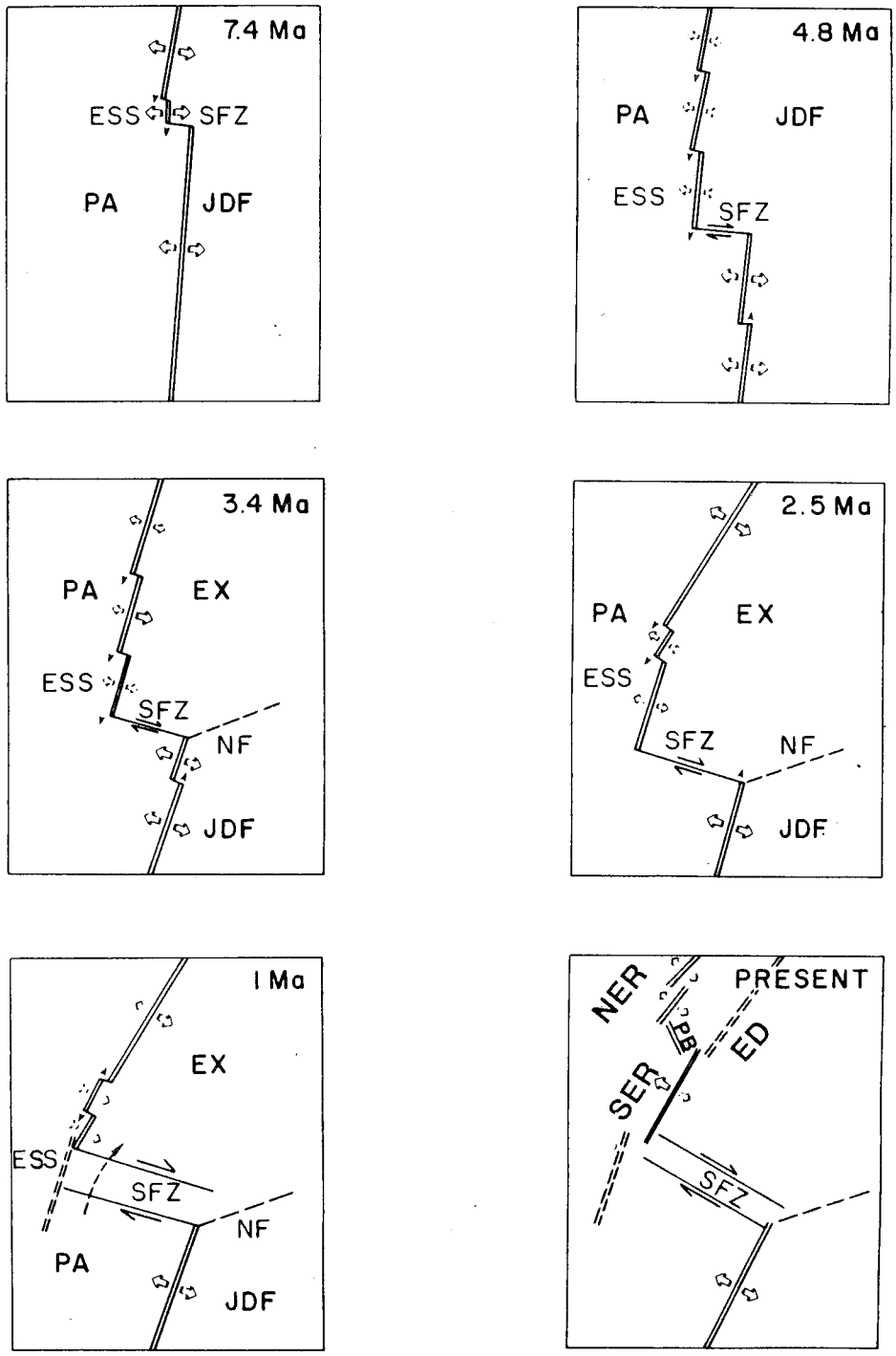


Figure 2: Model for the tectonic evolution of the Explorer region over the last 8 Ma. Feature labels and arrows explained in text (from Botros and Johnson, *in press*).

The central segment is what we today refer to as the Southern Explorer Ridge (SER). Botros and Johnson (*in review*) propose that this segment has undergone a recent (within the Brunhes) 'ridge jump' to the east. As the new locus of spreading is being established, the ridge propagates both north and south at about 30 mm/yr. During this propagation, the segment to the north (Explorer Deep in figure 1) is retreating. The following features are explained by this scenario:

1. the asymmetry of the Brunhes boundary about the SER.
2. the presence of highly magnetized extrusives and high amplitude magnetic anomalies in the northern portion of the SER.
3. the azimuth changes and lack of well established axial valleys in the northern and southern portions of the SER.
4. the development of an 'overlap spreading centre' morphology (Macdonald and Fox, 1983) between SER and the Explorer Deep (ED) to the north.

The southern tip of the ED appears in the SEABEAM data to extend to 22 km south of the northern tip of the SER (see following discussion on ridge morphology). Botros and Johnson (1986) suggest that there is a 'dueling propagator' relationship between the SER and Explorer Deep. This suggestion will be examined in light of the basalt geochemistry in Chapters 4 and 5.

Finally, the locus of spreading in the northernmost segment of the Explorer System has moved from the ED 40 km west to the Northern Explorer Ridge (NER). The NER, formerly referred to as the Explorer Rift, appears from the SEABEAM data to be made up of two en echelon spreading segments. Riddihough (1984) proposed that the ridge jump to the NER occurred at about 1 Ma. However, Botros and Johnson (*in review*) suggest the jump occured more recently at about 0.3 Ma BP. This would explain the fact that the Brunhes anomally of the ED is much wider than that of the NER. It is also consistent with the presence in both

the ED and NER of extensive basalt flows, shown in SeaMARC II images, from which very fresh basalts have been dredged (Cousens, 1982 and CASM 6 cruise, 1986).

The combined full spreading rate of the NER and ED during the Brunhes chron is calculated by Botros *et al.* (1986) to be 44 mm/yr and that of the SER is calculated to be 28 mm/yr. The NER is separated from the SER by a northwest trending pull-apart basin (PB in figure 2). SeaMARC II images indicate the presence of fresh basalt flows in this basin.

***Ridge Morphology***

The morphology of the Explorer area as depicted in the depth-enhanced SEABEAM bathymetry in figure 3, is examined in light of the findings of Botros *et al.* (1986). The SER extends 65 km from 49°18'N to 49°58'N. There are two points where the ridge changes orientation along its length, indicated by asterisks in figure 3. The southern 40% of the ridge segment is oriented at about N 10°E. The central 40% of the ridge, between 49°32' and 47'N, is oriented at N 20°E and the northern 20% is oriented at N 30°E. These reorientations result in an arcuate shape of the SER concave to the southeast.

Each of the reorientation points is associated with a change in morphology of the ridge. In the southern and northern portions, the ridge has a subdued and irregular relief and lacks a well developed axial valley. Small cone-shaped features less than 300 m across are developed on the axis, indicating that constructive volcanism is not extensive and is localized in time and space. This style of volcanism is characteristic of a spreading centre propagating into older cooler crust where large steady state magma chambers are not thermally stable (Hey and Wilson, 1982). The extent of volcanism and rifting is variable locally and an irregular axial topography results.

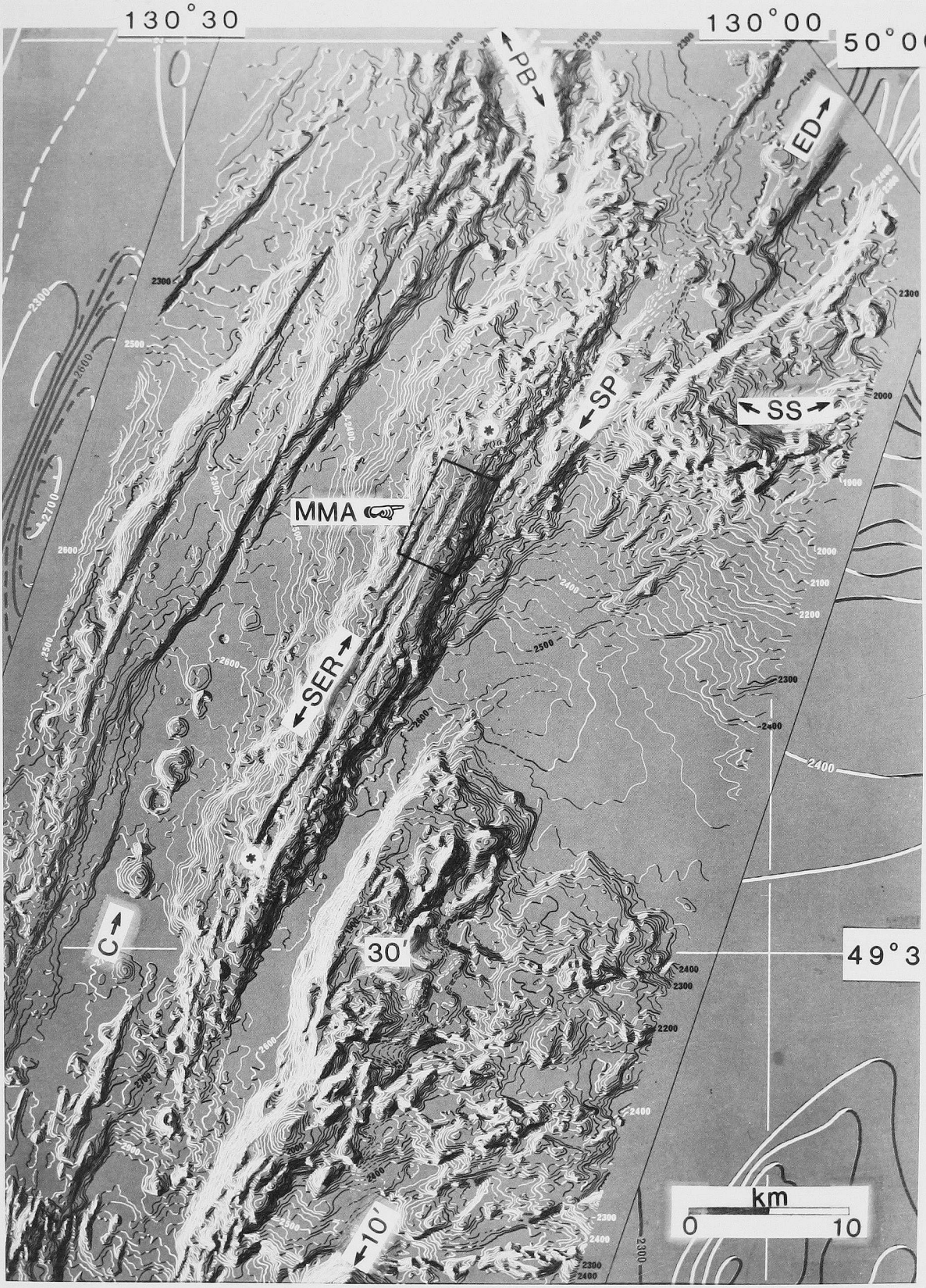


FIGURE 3: DEPTH ENHANCED SEABEAM BATHYMETRY OF THE EXPLORER REGION (MODIFIED FROM DAVIS ET AL., 1985). RECTANGLE ENCLOSES STUDY AREA; ABREVIATIONS DEFINED IN TEXT.

A thin ridge, parallel with the SER, is located between the MMA and Seminole Seamount (SS). This feature was originally named the Seminole Propagator (SP), but Botros *et al.* (1986) believe that this feature is more likely the bathymetric expression of the failing propagator tip of the Explorer Deep (ED) located to the north.

Morphology typical of a medium-spreading ridge (Macdonald *et al.*, 1982) is developed in the central portion of the SER. The axis rises about 600 m above the surrounding seafloor, with a well-defined axial valley between one and two km wide and 100 and 300 m deep. This indicates that the volcanism and rifting in the area are more evenly distributed and well established.

The axial valley becomes less pronounced and the ridge height increases northward through the central portion to the highest point on the ridge (1760 m depth) coincident with the point of re-orientation at 49°47'N. A shield volcano morphology is developed at this point.

The highest point on oceanic spreading centres is usually between 3000 and 2500 m deep (i.e. 800 to 1300 m deeper than the SER). Malacek and Clowes (1978) found that the crust of the SER is anomalously thick (8 to 10 km vs. normal 5 km) based on results of a seismic refraction profile passing across the ridge 20 km to the south of the topographic high. Thus the unusual height of the ridge may reflect in part an isostatic response of a thick crust.

A contributing factor to the crustal thickening may be an increased magma supply at the high point of the ridge due to the presence of an underlying mantle hot spot (Morgan, 1971). The Seminole Seamount, 15 km to the east of the high point, is elongated perpendicular to the trend of the SER. The morphology of the seamount is dominated by cone structures elongated parallel to its overall trend.

This morphology may result from eruptive products of a hot spot, centred on the SER, being carried away to the east on the moving plate.

The increased size of the Seminole Seamount approaching the SER (figure 3) may reflect an increased accumulation of materials resulting from the sudden decrease in the spreading rate east of the ridge since 1.5 Ma (Riddihough, 1977). The fact that the Seminole Seamount has not imparted a more recent magnetic signature onto the surrounding Explorer Plate (Botros, pers. comm.), is also consistent with the interpretation of hot spot genesis: the seamount and the surrounding plate were formed together on the spreading centre at the site of a hot spot.

The trend of the Scott Seamount chain, parallel to and south of the Dellwood Seamount chain (Seemann, 1982, regional bathymetry map) intersects the SER at the bathymetric high point and is parallel to the direction of Pacific plate motion (absolute). The seamounts may thus be products formed over the same hot spot as the Seminole Seamount. The greater length and more uniform dimensions of the Scott Seamounts than the Seminole Seamounts may possibly be attributed to asymetric spreading of the spreading centre. The present spreading rate east of the ridge is about 7 mm/yr, whereas the rate west of the ridge has been about 21 mm/yr over the past 3 to 4 Ma. (Botros, pers. comm.).

Two high-standing en echelon ridges trending parallel to the SER to the south and east (figure 3) have been informally named the 30 Minute (30′) and 10 Minute (10′) Ridges , referring to their latitudes above 49°N. They are both located outside of the Brunhes magnetic chron, both are seismically inactive and moderately sedimented. Dredged basalts are altered and encrusted with manganiferrous oxides. These ridges may have been active spreading centres which were abandoned as the locus of spreading jumped west and northward with time as the Explorer Plate

became decoupled from the Juan de Fuca Plate and began rotating and pivoting (Riddihough, 1984). In this way it is possible that the parallel line of volcanic cones (C in figure 3) 10 km to the west of the SER between 49°29′ and 41′N may be a manifestation of a very recent jump in spreading. This does not preclude the possibility of simultaneous spreading occuring at the SER, as is proposed for NER and ED.

Hey *et al.* (1980) proposed that many, if not all spreading centre jumps are a consequence of rift propagation which may be a mechanism by which spreading centres readjust to changes in the forces driving the plate motions. Thus, extensive ridge segmentation and migration may be the primary mechanism by which the large stresses and plate rotations of the Explorer region are accomodated. Schilling *et al.* (1982) have proposed that ridge propagation may be initiated by the presence of ridge centred hot spots. This possibility will be examined in more detail in Chapter 6, after presenting the petrography (Chapter 3), petrochemistry (Chapter 4) and the proposed petrogenesis (Chapter 5) of the MMA basalts.

***Summary***

Over the past 8 Ma, the Explorer region has had a complex tectonic history of jumps in locus of spreading, rift propagation and asymmetric spreading. The study area (MMA) is located on the SER, an arcuate 65 km spreading centre which appears to be propagating at both ends. The highest point of the segment, just north of the MMA, may lie above a mantle hot spot. The unusual morphology, asymmetric spreading and propagation of the SER results from regional tectonic stresses associated with the oblique convergence of the spreading system with the continental margin.

## 2.2 LOCAL GEOLOGY

### 2.2.1 SAMPLE LOCATIONS

Twenty four of the 25 samples from the study area were collected by the PISCES 4 submersible. The remaining sample (sample CASM-3) was found lodged in the frame for the ship-towed camera at the completion of a tow. The locations of these samples are shown in figure 4. The P1400 series of samples were collected on 6 dives during the SCHISM expedition and the P1500 series were collected on 4 dives during the CASM 4 expedition. A navigational fix was made of the sub from the tender ship after each sample was collected. The accuracy of this fix is affected by such factors as the length and angle to the horizontal of the signal path between the sub and the ship, and also the amount of attenuation and refraction that occurs as the signal passes through the different water layers of varying density. Considering all of these factors, the following estimates of sample location accuracy ($\pm 1\sigma$) were made:

1. $\pm 50$ m between samples collected on the same dive
2. $\pm 100$ m between samples collected on different dives of the same expedition
3. $\pm 200$ m between samples collected on different expeditions

The fact that the two samples P1490-5 and P1502-9, which plot close together, gave nearly identical chemical composition (see Ch. 4) corroborates the expected location accuracy.

The location of the sample recovered from the camera frame (CASM-3) is accurate to within 500 m. The samples P1501-S and P1489-4 fell onto the landing skids of the sub during the P1501 and P1489 dives. It can only be said that they were located in the vicinity of the other samples of their respective dives.

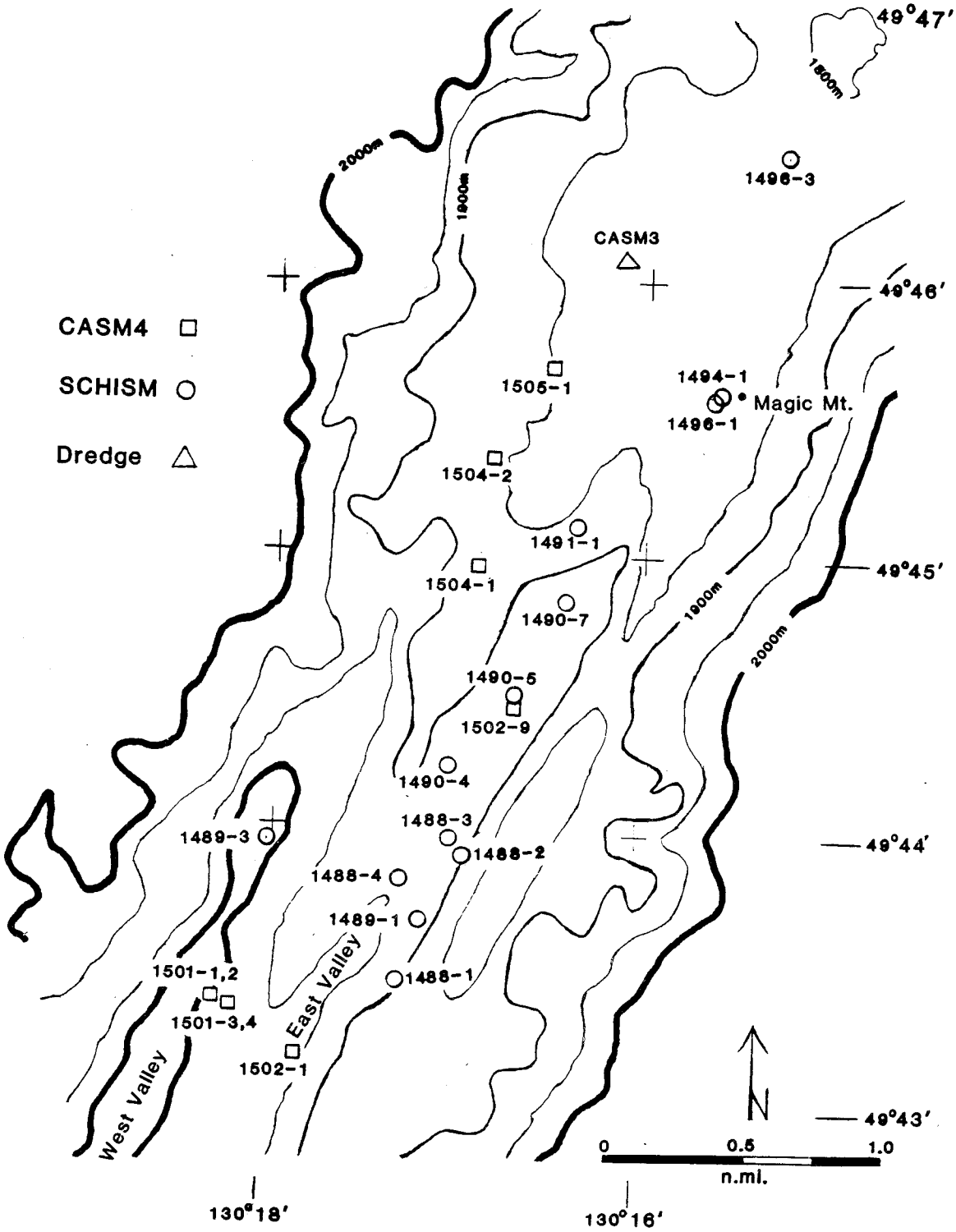


Figure 4: Local bathymetry and sample locations.

### 2.2.2 LOCAL BATHYMETRY

The local bathymetry is shown in figure 4 with the 50 m contours from the SEABEAM map (figure 3). In the south there are two well-defined rifted valleys (East Valley and West Valley), which become much less defined moving northward as the ridge axis domes and shoals to the high point, the summit of a 65 m high volcanic cone at 49°47'N. All of the samples were collected from within one kilometer of the ridge axis. Samples P1494-1 and P1496-1 are located adjacent to the Magic Mountain hydrothermal vent.

### 2.2.3 PHOTOGEOLOGY

The map of local geology (figure 5) was prepared by Tim McConachy at the University of Toronto from photos taken from a ship-towed camera. Seven tows were made during the CASM 3 cruise in 1984 and four during the CASM 5 cruise the following year. The camera was towed along the length of the axis with an average tow length of 4 km and with an average of 250 photos taken each tow. This provided coverage of a 2 km wide portion of the ridge axis between 49°42' and 49°47'N.

The density of the photo coverage was sufficient to resolve alternating bands of sheet, lobate and pillow flows trending parallel to the ridge axis (figure 5). Pillow flows are the most common, occuring both as elongate bulbous tubes (figure 6) and in broken pieces of talus (figure 7). Ropey sheet flows and lobate flows occur in lesser amounts (figure 8).

The abundance of sheet flows and collapsed lava lakes increases northward through the study area. The relative abundance of pillows versus sheet flows depends on a number of factors. Sheet lavas tend to dominate when lava viscosity is low, eruption rates are high and flows are poorly chanelled through large

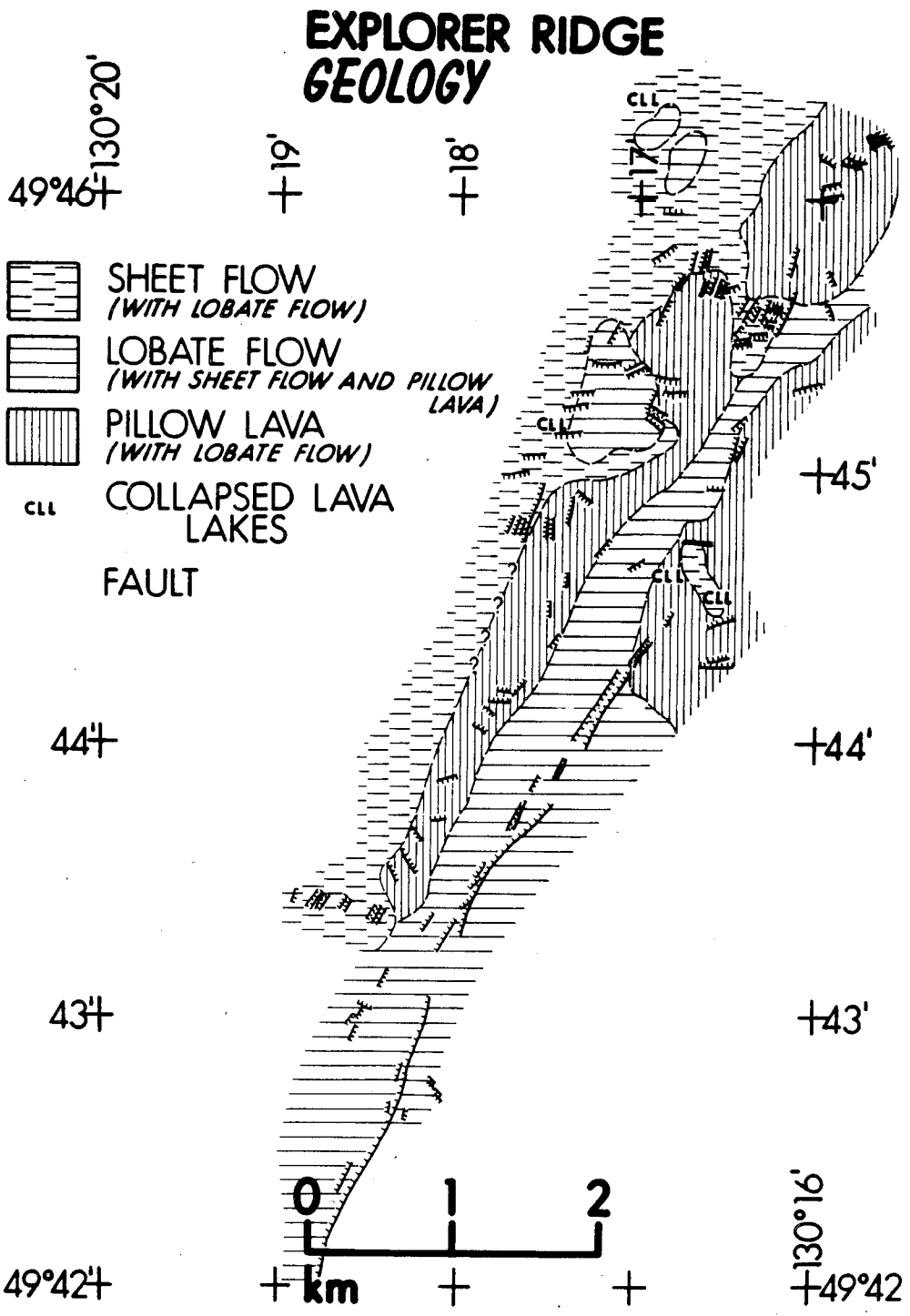


Figure 5: Local geology map compiled from photos from deep-towed camera (see text).

Figure 6: Basalt pillow tubes with characteristic radial fracturing (fieldwidth ≃ 2 m).

Figure 7: Basalt pillow talus. Heavier sediment cover indicates greater age of terrain (fieldwidth ≃ 4 m).

Figure 8: Basalt sheet flow. Notice light sediment cover (fieldwidth ≃ 4 m).

Figure 9: Corals on basalt pillows on the edge of a large fault scarp (fieldwidth ≃ 3 m).

fissures. The converse conditions tend to produce pillow flows, while lobate flows form in intermediate conditions (Holcomb and Clague, 1983). Thus the doming and shoaling of the ridge northwards may be an indication of increased eruption rates northward to the topographic high point.

Over 80% of the lava flows have less than 2% sediment cover, indicating that they have been extruded within the last 1000 years, assuming a maximum sedimentation rate of 4 cm/1000 yr (Lichtman *et al.*, 1984 and A.S.W. Denton, pers. comm.). The band of pillow lavas along the eastern extent of the study area is covered by 2% to 5% sediment except in pockets, where there is up to 20% sediment cover. The higher percentage of cover indicates that these pillows were formed before the central band of pillows. A collapsed lava lake within the older band of pillows to the east is very sparsely sedimented, indicating that it is quite young. Such lakes form as ponded sheet flows drain back into eruptive vents.

The large continuous fault scarp in the southern portion of the area lies within the East Valley and may well constitute the eastern wall of the East Valley (figures 4 and 8).

### 2.2.4 FAULTING AND HYDROTHERMAL ACTIVITY

The Magic Mountain vent is located in an area with many orthogonal faults (figures 5 and 9). The degree of hydrothermal activity and the number and size of sulphide bodies increases toward the high point of the region from the deeper rifted portion of the study area to the south. This increased activity may result from an increase in the heat supply due to convective cooling of a high level magma resevoir north of the study area. This hypothesis is evaluated in Chapter 6 in light of the chemical analysis of the MMA basalts.

***Summary***

25 fresh (less than 500 yr. old) basalt samples were collected from a region just south of the high standing point of the SER, which may be the site of a hot spot. This is suggested by increased hydrothermal activity and volcanism approaching the high point.

# 3. PETROGRAPHY

## 3.1 HAND SAMPLE DESCRIPTION

The samples include fresh angular fragments (4 to 10 cm) of basalt pillows or fragments of lobate and sheet flows. The description and location of each sample is listed in table 1.

The P1400 samples are predominantly pillow basalts that are moderately vesicular, microcrystalline and medium grey. Some samples have thin ferromanganese crusts. Red iron-oxide stains occur on some samples (figures 10 and 11). The P1500 samples, predominantly sheet flows and lobate basalts, are less vesicular, glassy and dark grey. They are quite fresh with little or no oxide accumulations (figure 12).

Seafloor photographs show that there is less than 5% sediment cover everywhere in the MMA. Thus, these flows were probably extruded within the last 1000 years (Chapter 2.2). The P1500 basalts (fresh lobate and sheet flows), most of which are from the western half of the study area, may be the product of recent volcanism characterized by a high magma supply rate. The more altered and MnO encrusted P1400 pillow flows located further to the east are inferred to be relatively older than the western flows, possibly having been erupted during an earlier, less-active period.

The CASM-3 sample is petrographically distinct from the other samples. It is a piece of a lava tube about 12 cm in diameter. The sample is rich in phenocrysts and glomerocrysts of plagioclase up to 1 cm in maximum dimension, in a light grey groundmass. Vesicles occur in concentric zones near the outer rim of the lava tube and in lines radiating from the core. This sample is unaltered and has a thick glassy rim with little or no oxide encrustation, indicating that it was recently formed (figure 13).

**Table 1: Hand Sample Descriptions and Locations**

| Sample | Description *(freshness/flow type; texture; vesicularity)* | Glass Rind *mm* | Oxide Rim *mm* | Latitude[1] 49°N + | Longitude *130°W* + | Depth *±5 m* |
|---|---|---|---|---|---|---|
| P1488-1 | *fresh pillow; abundant microphenocrysts in aphanitic ground mass; 5% vesicles with irregular size & shape in concentric zones* | *0* | *0* | 43.51 | 16.76 | ≈1850 |
| P1488-2 | *fresh lobe; sparce microphenocrysts; ves. like 88-1* | *2* | *4* | 43.90 | 17.40 | 1813 |
| P1488-3 | *fairly fresh pillow; microcrystalline; 1% vesicles 0.1-2 mm in diameter with regular shape and even distribution* | *0* | *0* | 43.97 | 17.40 | 1833 |
| P1488-4 | *fresh pillow; microcrystalline; ves. like 88-1* | *3* | *1* | 43.82 | 17.74 | 1945 |
| P1489-1 | *pillow like 88-3* | *3* | *0* | 43.68 | 17.65 | 1825 |
| P1489-3 | *pillow with 1 cm alteration rim; aphanitic + sparce plag phenos; ves. like 88-3* | *3* | *0* | 43.94 | 18.50 | 2011 |
| P1489-4 | *fresh pillow; 2% ves.; like 88-1* | *2* | *1* | ≈43 | ≈17 | ≈1900 |
| P1490-4 | *pillow like 88-3, 3 mm palagonite rim.* | *0* | *2* | 44.42 | 17.51 | 1917 |
| P1490-5 | *altered pillow; aphyric; ves. like 88-3 with uneven distribution* | *0* | *2* | 44.51 | 17.71 | 1899 |
| P1490-7 | *altered pillow; microcrystalline; 2% ves. like 88-1* | *1* | *2* | 44.83 | 16.91 | 1917 |
| P1491-1 | *pillow like 90-7 with even distribution of vesicles* | *0* | *0* | 45.09 | 16.81 | 1878 |
| P1494-1 | *fresh pillow; microcrystalline; 3% ves. with uneven size, shape, concentrated in pockets* | *0* | *0.3* | 45.58 | 16.13 | 1780 |
| P1496-1 | *fresh pillow; sparce microphenocrysts in glassy ground mass; 2% 0.1-10 mm elongate vesicules* | *0* | *0* | 43.51 | 16.76 | ≈1850 |

[1]decimal minutes north of 49°N and west of 130°W

**Table 1: Hand Sample Descriptions and Locations**

| Sample | Description (*freshness/flow type; texture; vesicularity*) | Glass Rind *mm* | Oxide Rim *mm* | Latitude[1] 49°N + | Longitude *130°W* + | Depth *±5 m* |
|---|---|---|---|---|---|---|
| P1496-3 | *fresh sheet flow; aphanitic; 3% vesicles 0.1 to 10 mm often elongated* | *1* | *1* | 46.41 | 15.85 | ≈1750 |
| P1501-1 | *very fresh lobe; aphyric, glassy to aphanitic; less than 1% ves. 0.1 to 0.2 mm evenly distributed, some 1 to 2 cm vesicles* | *4* | *0* | 43.41 | 18.78 | 1871 |
| P1501-2 | *very similar to 01-1* | *4* | *0* | 43.41 | 18.78 | 1871 |
| P1501-3 | *very similar to 01-1, some 4.0 cm elongate vesicles* | *2* | *0* | 43.37 | 18.63 | 1968 |
| P1501-4 | *like 01-1; mildly altered* | *4* | *0* | 43.37 | 18.63 | 1968 |
| P1501-S | *very fresh pillow; like 01-1* | *4* | *3* | ≈43.4 | ≈18.7 | ≈1900 |
| P1502-1 | *mod. altered lobe or sheet fragment; aphyric; 1% ves. up to 1 cm, concentrated in zones perpendicular to rim* | *0* | *1* | 43.21 | 18.29 | 1948 |
| P1502-9 | *fairly altered pillow; microcrystalline; 2% ves. less than 4mm even distribution in interior, sparce in outer 3cm of fragment* | *2* | *2* | 44.47 | 17.17 | 1884 |
| P1504-1 | *fairly altered pillow; aphyric; 2% elongate ves. concentrated in zone 2 cm from the rim* | *3* | *0* | 44.95 | 17.38 | 1849 |
| P1504-2 | *sheet very similar to 1501-4* | *7* | *1* | 45.33 | 17.30 | 1856 |
| P1505-1 | *lobe very similar to 1501-1* | *4* | *0* | 45.70 | 16.93 | 1801 |
| CASM-3 | *fresh elongate lava tube; plag porphyritic in microcrstalline groundmass; 2% ves. 0.1 to 4 mm wide, alternating ves. rich and ves. poor bands* | *2* | *0* | 46.07 | 15.90 | ≈1780 |

[1]decimal minutes north of 49°N and west of 130°W


Figure 10: Sample P1489-4: a moderately vesicular microcrystalline pillow basalt with ferromanganese oxide crust (black) and minor iron oxide staining (red-brown).


Figure 11: Sample P1490-5: a pillow basalt fragment with thin oxide crust. Note the light coloured thin zone of alteration on the rim of the cut surface.


Figure 12: Sample P1505-1: an aphyric glassy lobate flow with few vesicles and no visible alteration.


Figure 13: Sample CASM-3: a plagioclase porphyritic lava tube with concentrically zoned vesicles and a radial fracture pattern.

## 3.2 DESCRIPTION AND MODAL ANALYSES OF THIN SECTIONS

In thin section, the plagioclase, clinopyroxene and olivine crystals are unaltered. Minor iron-oxide stains are developed along fractures and in vesicles. Detailed petrographic descriptions for each sample are summarized in table 2. The modal analyses included in the table were determined in the manner described by Chayes (1956).

Zonation in the crystallinity of the groundmass, from glassy outer rims to variolitic inner rims to holocrystalline cores, typical of pillow basalts (Marshal and Cox, 1971) is observed in many of these samples. This zonation reflects increasing degrees of supercooling towards the rim as an extruded pillow is quenched by cold sea water (Bryan, 1972).

Microphenocrysts are easily identified in the quenched glassy rims (figure 14). They can be confused with microlites in the more crystalized interiors (figure 15). Consequently, the accuracy of the modal estimates varies with the degree of crystallinity of the mesostasis. The error was minimized by applying consistent size and shape criteria to discriminate between microlites and microphenocrysts for the analysis of each sample. These criteria, along with details on the method and accuracy of the modal analysis are presented in Appendix A.

Total crystallinity is less than 6% in all of the samples except CASM-3, which has 10.5% crystals comprised mostly of plagioclase glomerocrysts.

Plagioclase is present in all samples and is always the most abundant phase. It occurs most commonly as elongate to skeletal microphenocrysts, often associated with clinopyroxene and/or olivine microphenocrysts (figures 15 and 16). These textures indicate cotectic crystallization.

**Table 2: Mineral Modes and Petrographic Summary**

| Sample | Vesicle Free Mode (%) | | | | | Ves.% | Phenocryst Assemblage | | | | | | Groundmass Assemblage[1] | | | | |
|---|---|---|---|---|---|---|---|---|---|---|---|---|---|---|---|---|---|
| | PLAG XENO | PLAG | CPX | OLIV | Total | | PL+CPX | PL+OL | PL+PL | CPX+CPX | ophitic | PL+CPX+OL | PL | CPX | OL | oxide | glass |
| P1488-1 | 2.3 | 0.4 | 0.5 | 1.2 | 4.5 | 10.3 | ⊙ | ● | ⊙ | O | ● | O | ⊙ | O | | | ● |
| P1488-2 | 1.0 | 0.2 | 0.2 | 0.4 | 1.8 | 10.5 | ⊙ | ● | ⊙ | O | O | | ⊙ | | | | |
| P1488-3 | 2.0 | 0.3 | 0.4 | 0.3 | 3.0 | 5.5 | ⊙ | ● | ⊙ | | O | O | ⊙ | ⊙ | | ● | |
| P1488-4 | 1.6 | 0.1 | 0.3 | 0.5 | 2.5 | 10.7 | ⊙ | ● | ⊙ | | O | O | ⊙ | | | | |
| P1489-1 | 1.4 | 0.3 | 0.2 | 0.9 | 2.8 | 5.8 | O | ● | O | | ⊙ | O | O | | | | |
| P1489-3 | 0.2 | 0.1 | | | 0.3 | 2.3 | | | ⊙ | | | | ● | ● | O | ● | |
| P1489-4 | 2.2 | 0.1 | 1.7 | 0.1 | 4.1 | 6.1 | ● | O | O | | ⊙ | | ● | ● | | ⊙ | |
| P1490-4 | 2.7 | 0.7 | 2.0 | 0.2 | 5.6 | 3.1 | ● | O | O | | ⊙ | O | ● | ● | O | O | |
| P1490-5 | 2.4 | 0.4 | 1.7 | 0.3 | 4.8 | 3.6 | ● | ● | O | | ● | ⊙ | ⊙ | ⊙ | | ● | |
| P1490-7 | 2.0 | 0.3 | 1.5 | 0.1 | 3.9 | 2.5 | ● | ⊙ | O | O | ● | ⊙ | ⊙ | O | O | ● | |
| P1491-1 | 0.4 | 0.1 | 0.3 | 0.1 | 0.9 | 15.4 | ⊙ | O | | ⊙ | ⊙ | O | ● | ● | O | ● | |
| P1494-1 | 1.3 | | 0.5 | 0.2 | 2.0 | 11.4 | O | ⊙ | O | | ● | ● | ⊙ | O | | | ⊙ |
| P1496-1 | 1.6 | | 0.7 | 0.6 | 2.9 | 3.0 | O | ⊙ | | | ● | O | ⊙ | | | | ● |
| P1496-3 | 0.2 | 0.2 | | | 0.4 | 9.3 | | | ⊙ | | | | O | O | O | | |
| P1501-1 | tr | | | | tr | 2.0 | | | | | | | O | O | O | | |
| P1501-2 | | | | | | 3.0 | | | | | | | O | | O | | |
| P1501-3 | tr | | | | tr | 2.3 | | | | | | | O | | O | | |
| P1501-4 | tr | 0.1 | | | 0.1 | 2.0 | | | | | | | O | | O | | |
| P1501-S | tr | | | | tr | 2.0 | | | | | | | O | | O | | |
| P1502-1 | | | | | | 3.3 | | | | | | | O | | | ⊙ | |
| P1502-9 | 1.0 | 0.4 | 0.1 | | 1.6 | 4.1 | | | | | | | O | | | | O |
| P1504-1 | 0.5 | 0.1 | 0.3 | | 0.9 | 3.9 | O | | | | | ⊙ | O | ⊙ | O | | |
| P1504-2 | 0.7 | | 0.2 | | 0.9 | 1.3 | | | | ● | | | | | O | | ● |
| P1505-1 | 0.2 | 0.3 | | | 0.5 | 1.1 | | | | ● | | | O | O | O | | ● |
| CASM-3 | 2.0 | 8.2 | 0.1 | 0.2 | 10.5 | 16.1 | | | ● | | | | O | O | O | | |

[1]crystal abundance: ● = observed throughout, ⊙ = sparcely throughout, O = trace abundance

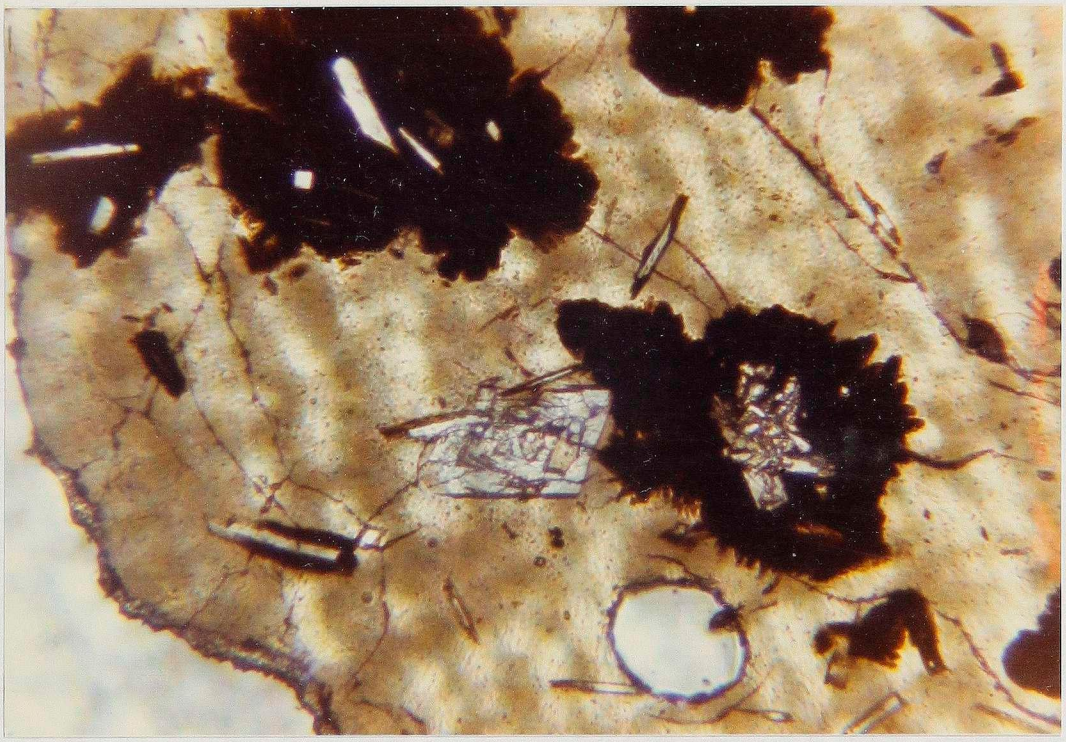

Figure 14: Sample P1496-1: quenched glass rim with early formed skeletal olivine and plagioclase; later formed plagioclase-clinopyroxene surrounded by red-brown devitrified glass (field of view (fov)=1.6mm).

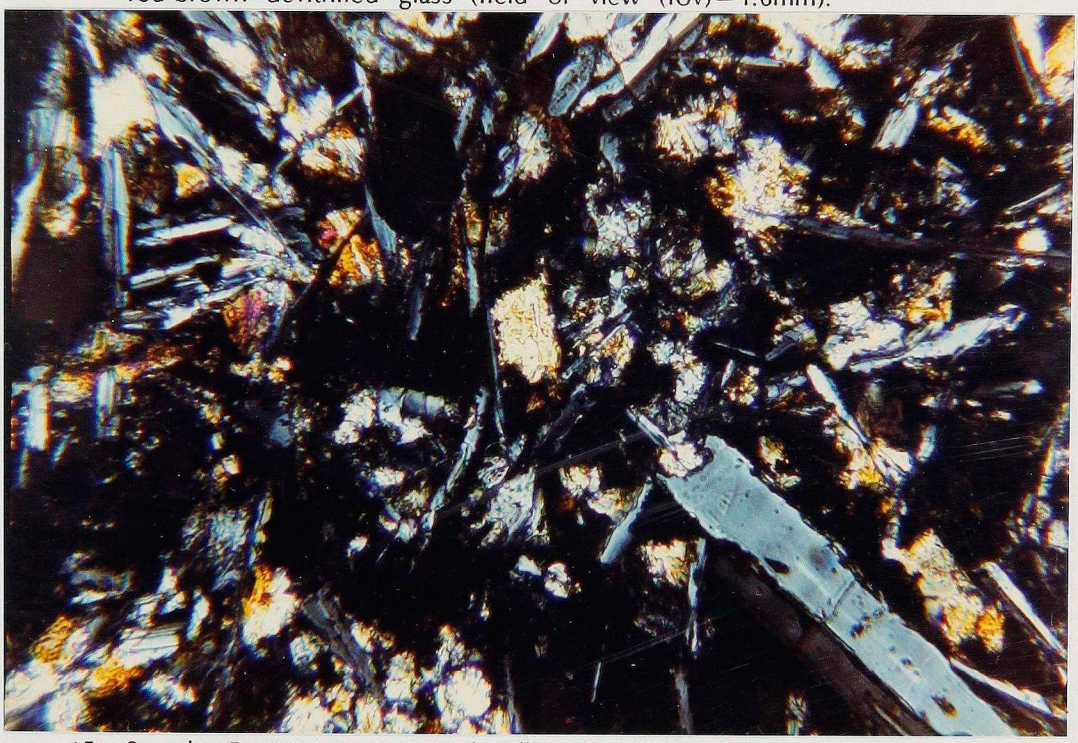

Figure 15: Sample P1490-4: interior of pillow basalt with holocrystalline groundmass consisting of skeletal plagioclase, anhedral clinopyroxene and trace amounts of olivine microlytes (fov=0.53mm).

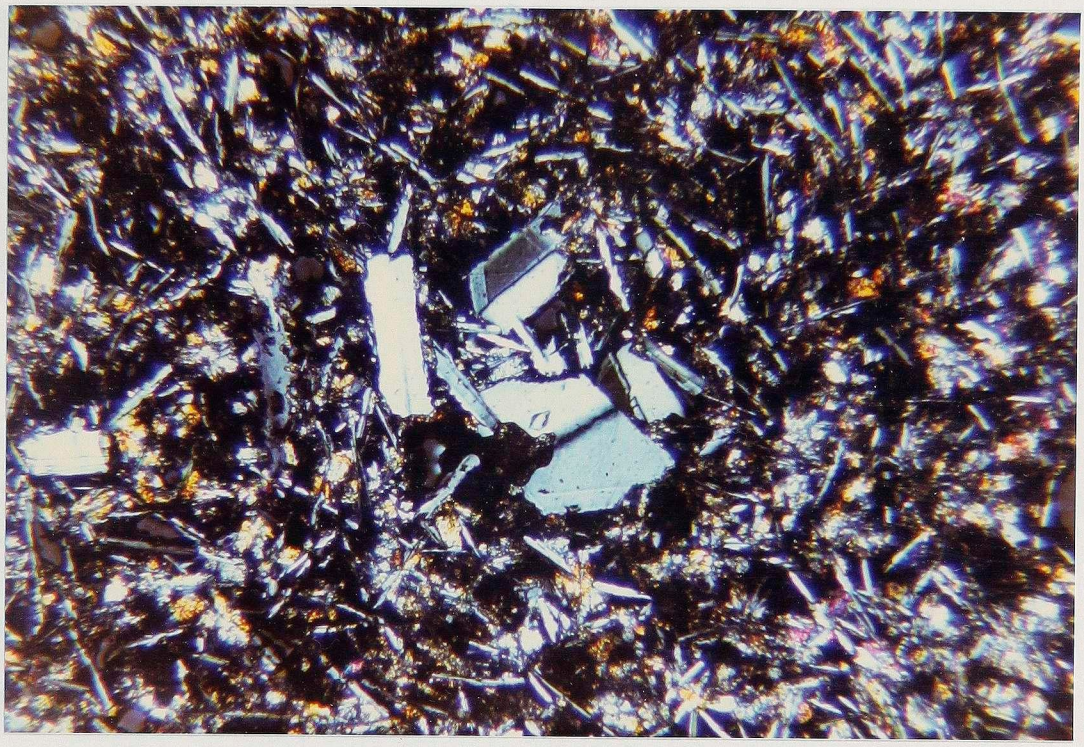

Figure 16: Sample P1490-4: earlier formed zoned and partially resorbed plagioclase in holocrystalline groundmass (fov=0.73mm).

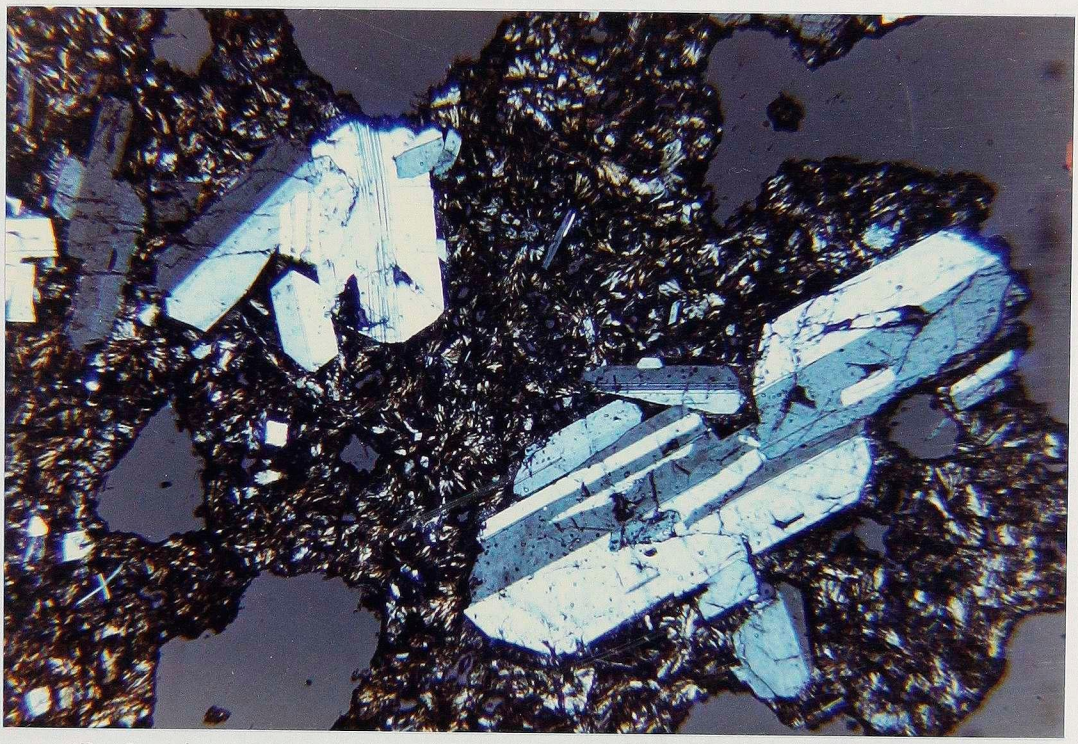

Figure 17: Sample CASM-3: plagioclase phenocrysts in synneusis relationship (fov=2.9mm).

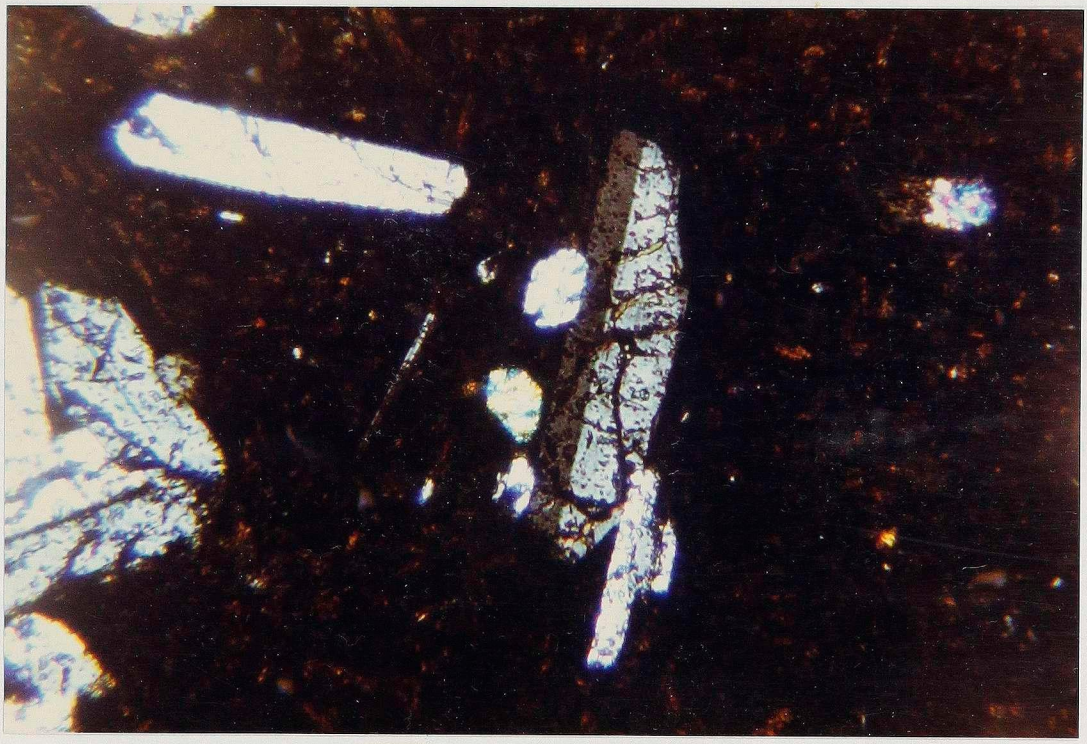

Figure 18: Sample CASM-3: partially resorbed inclusion rich plagioclase xenocryst with equant olivine microphenocrysts (fov=1.6mm).

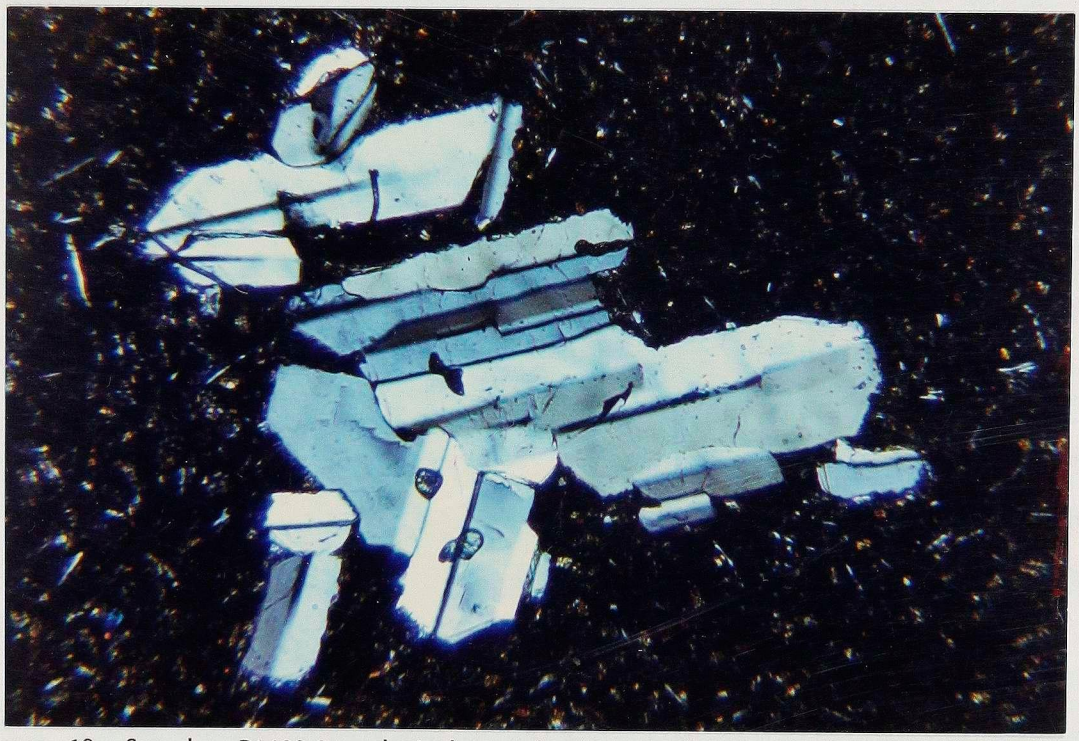

Figure 19: Sample P1489-3: plagioclase glomerocryst with partially resorbed rim (fov=2.9mm).

Plagioclase phenocrysts (>0.5 mm) occur in some, but not all samples. Normal chemical zonation from calcic cores to more sodic rims (typically a difference of between 5% to 10% An, cf. Chapter 4.2) is common in plagioclase. Phenocrysts are usually tabular in shape, and often occur with other plagioclase crystals in glomerocrysts or in a synneusis relationship (figures 17, 18 and 19). Some of these crystals have rounded and embayed oscillatory zoned cores rich in glass inclusions, suggesting that they are xenocrystic. Partially resorbed rims are also observed on some phenocrysts (figure 19).

Both phenocrysts and microphenocrysts typically have thin (10 to 20$\mu$m) rims with continuous chemical zonation outward to An values in the range of An 60 to 64.

Clinopyroxene is present in most samples, occurring as anhedral to subhedral microphenocrsts. Textures suggest that clinopyroxene crystallized after plagioclase and either after (figure 14) or concurrently with (figure 15) olivine. Clinopyroxene is also very common in the groundmass of holocrystalline samples, occurring as patchy to elongate crystals interlocking with acicular plagioclase microlites (figure 15). Bow tie intergrowths of clinopyroxene with fine plagioclase microlite laths are observed in some samples. Chemical zonation was not observed optically, although there are large and highly irregular zonations in most constituent elements (Chapter 4.2).

Olivine in most samples comprises less than 0.3% of the mode, occuring commonly as skeletal microphenocrysts (figure 14) and as subhedral equant microlites. Phenocrysts of olivine were only observed in the CASM-3 sample, occuring together with plagioclase crystals (figure 19).

Small amounts of opaque oxide crystals occur as very fine irregular grains in the groundmass of some more highly crystallized samples. Scanning electron

microscope (SEM) analyses reveal these to be titanium-rich magnetites.

Most of the samples are one of the four petrographic types summarized below. They are distinguished by degree of crystallinity, the relative abundance of olivine and clinopyroxene and by mineral associations:

1. ***aphyric:*** less than 0.3% total crystals composed almost entirely of small well-formed plagioclase laths. Vesicularity is low (less than 3%). The groundmass is glassy to variolitic containing acicular plagioclase microlites and trace amounts of equant olivine and clinopyroxene microlites.

2. ***moderately phyric, clinopyroxene rich:*** 0.3 to 5.6% crystals consisting of plagioclase occuring in glomerocrysts or in an ophitic relationship with clinopyroxene (± olivine), or occasionally as tabular xenocrysts; vesicle content 3 to 15%; groundmass variolitic to holocrystalline.

3. ***moderately phyric, olivine rich:*** 1.8 to 4.5% crystals consisting of plagioclase commonly in glomerocrysts with olivine and less commonly with clinopyroxene. Tabular plagioclase xenocrysts are more common, often clustered. Vesicle content 5 to 10%; groundmass variolitic to hyalocrystalline; olivine and clinopyroxene microlites rare.

4. ***crystal cumulate:*** (CASM-3 only) 10.5% crystals, most of which are tabular plagioclase xenocrysts usually in glomerocrysts (± olivine xenocrysts). Many of these crystals contain abundant glass inclusions. Smaller elongate laths of plagioclase are also present, often with small late formed anhedral clinopyroxene crystals and euhedral olivine microlites; vesicle content 16%, groundmass variolitic.

The petrographic type of each sample is indicated in the final column of table 2. By examining the sample location map (figure 4), one can see that samples that are petrographically similar are commonly spacially close as well. These similarities will be considered along with chemical affinities in establishing comagmatic groupings in Chapter 5.

# 4. PETROCHEMISTRY

## 4.1 WHOLE ROCK CHEMISTRY

Analyses for ten major and ten trace elements were determined by x-ray flourescence spectrometry (XRF) using the Department of Oceanography's Phillips PW1400 XRF spectrometer. Fused glass disks were analysed for the major elements and pressed-powder pellets for the trace elements and sodium ($Na_2O$). Details on the sample preparation are presented in Appendix B. A discussion of the analytical procedures, run conditions, data reduction and error analysis for the major and trace elements are included in Appendices C and D respectively.

The XRF instrument conditions for both the major and trace element analyses are listed in table 3. The major and trace element analyses are presented in table 4, along with the calculated CIPW norms. Total iron contents are reported as FeO. This table also includes total error estimates and detection limits. The total error for major elements is effectively constant across the compositional range. The total error for some of the trace elements varies with composition, thus individual error estimates were made for each analysis. Details on the calculations for total error and detection limits are included in Appendices C and D.

### 4.1.1 NORMATIVE CALCULATIONS

CIPW norms were calculated using the program CHEMPLOT which was modified by C.J. Hickson from an earlier program by Graham Nixon. The results are included in table 4 expressed in weight percent.

TABLE 3: ANALYTICAL PARAMETERS FOR MAJOR AND TRACE ELEMENTS BY X-RAY FLUORESCENCE SPECTROMETRY

| ELEMENT | LINE | FILT | COLL[1] | DET[2] | XTL | UPL[3] | LWL[4] | Kv | Ma | λ (Å) | PEAK ANGLE° | BACKGROUND °+OFF | BACKGROUND °-OFF | COUNT TIME(s) PEAK | COUNT TIME(s) BACK |
|---|---|---|---|---|---|---|---|---|---|---|---|---|---|---|---|
| Si | Kα | *No* | C | F | T/RAP | 80 | 20 | 60 | 40 | 7.126 | 32.230 | 2.30 | 0.00 | 40 | 20 |
| Ti | Kα | *No* | C | F | LiF 200 | 75 | 25 | 60 | 40 | 2.750 | 86.270 | 0.00 | 1.00 | 40 | 10 |
| Al | Kα | *No* | C | F | T/RAP | 80 | 20 | 60 | 40 | 8.339 | 37.875 | 1.00 | 0.00 | 80 | 20 |
| Fe | Kα | *No* | C | F | LiF 200 | 85 | 15 | 60 | 40 | 1.937 | 57.670 | 0.00 | 1.60 | 40 | 20 |
| Mn | Kα | *No* | C | F | LiF 200 | 75 | 15 | 60 | 40 | 2.103 | 63.210 | 1.50 | 0.00 | 40 | 10 |
| Mg | Kα | *No* | C | F | T/RAP | 80 | 20 | 30 | 60 | 9.889 | 45.210 | 0.00 | 1.20 | 200 | 100 |
| Ca | Kα | *No* | F | F | LiF 200 | 80 | 20 | 50 | 20 | 3.360 | 113.16 | 1.40 | 0.00 | 40 | 20 |
| Na | Kα | *No* | C | F | T/RAP | 80 | 20 | 30 | 60 | 11.909 | 55.250 | 0.00 | 1.70 | 200 | 100 |
| K | Kα | *No* | F | S | LiF 200 | 80 | 20 | 60 | 40 | 3.744 | 136.78 | 2.00 | 0.00 | 40 | 20 |
| P | Kα | *No* | C | F | Ge | 80 | 20 | 30 | 60 | 6.155 | 141.12 | 0.00 | 1.50 | 200 | 100 |
| Ba | Lα | *No* | F | F | LiF 200 | 80 | 20 | 60 | 40 | 2.776 | 87.220 | 1.20 | 0.00 | 400 | 400 |
| Cr | Kα | *No* | C | F | LiF 200 | 80 | 20 | 60 | 40 | 2.291 | 69.520 | 1.00 | 0.00 | 80 | 40 |
| Cu | Kα | *Yes* | C | F S | LiF 200 | 80 | 20 | 60 | 40 | 1.542 | 45.060 | 0.00 | 0.62 | 80 | 40 |
| Nb | Kα | *No* | F | S | LiF 200 | 62 | 20 | 60 | 40 | 0.748 | 21.430 | 0.40 | 0.40 | 400 | 400 |
| Ni | Kα | *No* | F | F S | LiF 200 | 80 | 20 | 60 | 40 | 1.659 | 48.670 | 1.20 | 0.60 | 80 | 40 |
| Rb | Kα | *No* | F | S | LiF 200 | 80 | 20 | 60 | 40 | 0.927 | 26.660 | 0.40 | 0.90 | 400 | 400 |
| Sr | Kα | *No* | F | S | LiF 200 | 75 | 25 | 60 | 40 | 0.877 | 25.175 | 0.60 | 0.60 | 80 | 40 |
| V | Kα | *No* | C | F | LiF 200 | 80 | 20 | 60 | 40 | ?.000 | 77.135 | 4.00 | 2.60 | 80 | 40 |
| Y | Kα | *No* | F | S | LiF 200 | 80 | 20 | 60 | 40 | 0.831 | 23.800 | 0.60 | 0.60 | 80 | 40 |
| Zr | Kα | *No* | F | S | LiF 200 | 80 | 20 | 60 | 40 | 0.788 | 22.580 | 0.74 | 0.74 | 80 | 40 |

[1]collimator: C=coarse F=fine [2]detector: F=flow S=scintillation [3]upper level window [4]lower level window

## TABLE 4: CHEMICAL ANALYSIS AND NORMS

| SAMPLE | | P1488-1 | P1488-2 | P1488-3 | P1488-4 | P1489-1 | P1489-3 | |
|---|---|---|---|---|---|---|---|---|
| **Wt%** | %error | | | | | | | Det. |
| $SiO_2$ | 0.45 | **50.34** | **50.64** | **50.43** | **50.20** | **50.40** | **50.72** | 0.73 |
| $TiO_2$ | 0.49 | **1.71** | **1.71** | **1.71** | **1.71** | **1.72** | **1.70** | 0.01 |
| $Al_2O_3$ | 0.88 | **15.06** | **14.72** | **14.72** | **14.44** | **14.88** | **14.44** | 0.24 |
| FeO* | 0.15 | **10.66** | **10.67** | **10.64** | **10.55** | **10.65** | **10.65** | 0.13 |
| MnO | 4.40 | **0.20** | **0.21** | **0.21** | **0.20** | **0.21** | **0.20** | 0.01 |
| MgO | 2.40 | **6.94** | **6.95** | **6.98** | **6.99** | **6.92** | **6.91** | 0.12 |
| CaO | 0.40 | **11.14** | **11.22** | **11.20** | **11.36** | **11.18** | **11.06** | 0.13 |
| $Na_2O$ | 1.48 | **3.00** | **2.89** | **2.86** | **2.60** | **3.08** | **2.56** | 0.24 |
| $K_2O$ | 1.77 | **0.42** | **0.41** | **0.45** | **0.42** | **0.42** | **0.46** | 0.04 |
| $P_2O_5$ | 2.80 | **0.24** | **0.24** | **0.23** | **0.23** | **0.24** | **0.23** | 0.01 |
| TOTAL | | **99.71** | **99.66** | **99.43** | **98.70** | **99.68** | **98.60** | |
| **ppm** | | | | | | | | |
| Ba | | **86.** ± 8. | **80.** ± 9. | **74.** ± 10. | **75.** ± 9. | **74.** ± 9. | **80.** ± 8. | 2.5 |
| Cr | | **86.** ± 3. | **89.** ± 4. | **85.** ± 2. | **88.** ± 3. | **88.** ± 3. | **114.** ± 4. | 2.0 |
| Cu | | n.d. | **33.** ± 4. | n.d. | n.d. | n.d. | **49.** ± 5. | 2.7 |
| Nb | | **14.2** ± 0.5 | **13.3** ± 0.4 | **13.5** ± 0.4 | **13.9** ± 0.5 | **13.6** ± 0.5 | **13.7** ± 0.5 | 0.5 |
| Ni | | **64.** ± 6. | **63.** ± 6. | **61.** ± 5. | **61.** ± 5. | **59.** ± 4. | **61.** ± 4. | 2.3 |
| Rb | | **6.6** ± 1.0 | **6.3** ± 1.0 | **6.4** ± 1.0 | **6.3** ± 1.0 | **6.5** ± 1.0 | **6.2** ± 1.0 | 2.1 |
| Sr | | **177.** ± 10. | **173.** ± 10. | **172.** ± 10. | **174.** ± 12. | **173.** ± 11. | **169.** ± 12. | 2.4 |
| V | | **200.** ± 10. | **177.** ± 8. | **161.** ± 8. | **125.** ± 6. | **125.** ± 6. | **178.** ± 9. | 1.1 |
| Y | | **35.** ± 2.1 | **35.** ± 2.1 | **35.** ± 2.1 | **36.** ± 2.1 | **35.** ± 2.1 | **37.** ± 2.2 | 2.3 |
| Zr | | **135.** ± 3. | **132.** ± 3. | **134.** ± 3. | **133.** ± 4. | **132.** ± 4. | **132.** ± 4. | 3.0 |
| **CIPW Norm** | | (wt%) | | | | | | |
| q | | 0.00 | **0.00** | **0.00** | **0.00** | **0.00** | **0.00** | |
| or | | 2.49 | **2.43** | **2.67** | **2.51** | **2.49** | **2.75** | |
| ab | | 25.44 | **24.52** | **24.32** | **22.27** | **26.12** | **21.95** | |
| an | | 26.43 | **26.04** | **26.12** | **26.81** | **25.53** | **26.90** | |
| di | | 22.54 | **23.21** | **23.22** | **23.63** | **23.45** | **22.35** | |
| hy | | 9.23 | **12.55** | **11.85** | **18.18** | **7.90** | **20.78** | |
| fo | | 4.51 | **3.18** | **3.48** | **1.84** | **4.82** | **0.13** | |
| fa | | 4.32 | **3.03** | **3.31** | **1.73** | **4.62** | **0.12** | |
| mt | | 1.23 | **1.24** | **1.24** | **1.22** | **1.24** | **1.19** | |
| il | | 3.25 | **3.26** | **3.26** | **3.29** | **3.27** | **3.27** | |
| ap | | 0.56 | **0.58** | **0.54** | **0.54** | **0.58** | **0.54** | |

## TABLE 4: CHEMICAL ANALYSIS AND NORMS

| SAMPLE | | P1489-4 | P1490-4 | P1490-5 | P1490-7 | P1491-1 | P1494-1 | |
|---|---|---|---|---|---|---|---|---|
| **Wt%** | %error | | | | | | | Det. |
| $SiO_2$ | 0.45 | 50.38 | 49.99 | 51.10 | 49.68 | 49.52 | 50.07 | 0.73 |
| $TiO_2$ | 0.49 | 2.11 | 1.61 | 2.35 | 1.76 | 1.46 | 1.77 | 0.01 |
| $Al_2O_3$ | 0.88 | 13.96 | 15.07 | 14.25 | 14.23 | 14.91 | 14.33 | 0.24 |
| FeO* | 0.15 | 11.96 | 10.21 | 12.55 | 10.95 | 9.78 | 10.60 | 0.13 |
| MnO | 4.40 | 0.23 | 0.20 | 0.23 | 0.20 | 0.17 | 0.19 | 0.01 |
| MgO | 2.40 | 5.65 | 6.94 | 5.44 | 6.68 | 7.66 | 6.50 | 0.12 |
| CaO | 0.40 | 10.47 | 11.29 | 9.92 | 11.20 | 11.96 | 11.06 | 0.13 |
| $Na_2O$ | 1.48 | 2.87 | 3.12 | 3.28 | 3.17 | 2.64 | 2.90 | 0.24 |
| $K_2O$ | 1.77 | 0.56 | 0.55 | 0.75 | 0.40 | 0.42 | 0.55 | 0.04 |
| $P_2O_5$ | 2.80 | 0,31 | 0.22 | 0.35 | 0.25 | 0.20 | 0.26 | 0.01 |
| TOTAL | | 98.50 | 99.20 | 100.22 | 98.52 | 98.72 | 98.23 | |
| **ppm** | | | | | | | | |
| Ba | | 106 ± 3 | 124 ± 4 | 158 ± 4 | 72 ± 2 | 69 ± 2 | 117 ± 3 | 2.5 |
| Cr | | 47 ± 1 | 58 ± 2 | 38 ± 1 | 95 ± 3 | 272 ± 8 | 40 ± 1 | 2.0 |
| Cu | | 52 ± 4 | 67 ± 4 | 42 ± 3 | 62 ± 4 | 81 ± 5 | 64 ± 4 | 2.7 |
| Nb | | 19.1 ± 0.6 | 17.9 ± 0.6 | 23.6 ± 0.7 | 14.4 ± 0.5 | 14.3 ± 0.5 | 20.3 ± 0.5 | 0.5 |
| Ni | | 41 ± 3 | 50 ± 3 | 39 ± 3 | 62 ± 4 | 90 ± 5 | 53 ± 4 | 2.3 |
| Rb | | 8.6 ± 1.0 | 6.4 ± 1.0 | 10.7 ± 0.9 | 6.7 ± 1.0 | 6.0 ± 1.0 | 8.4 ± 1.0 | 2.1 |
| Sr | | 173 ± 6 | 190 ± 6 | 185 ± 6 | 171 ± 5 | 164 ± 5 | 197 ± 6 | 2.4 |
| V | | 403 ± 13 | 331 ± 11 | 443 ± 14 | 348 ± 11 | 305 ± 10 | 355 ± 11 | 1.1 |
| Y | | 43 ± 2.4 | 31 ± 1.9 | 43 ± 2.4 | 37 ± 2.2 | 32 ± 1.9 | 35 ± 2.1 | 2.3 |
| Zr | | 170 ± 3 | 190 ± 3 | 185 ± 3 | 171 ± 3 | 164 ± 3 | 197 ± 4 | 3.0 |
| **CIPW Norm** | | (wt%) | | | | | | |
| q | | 0.00 | 0.00 | 0.00 | 0.00 | 0.00 | 0.00 | |
| or | | 3.36 | 3.27 | 4.42 | 2.40 | 2.51 | 3.31 | |
| ab | | 24.63 | 26.59 | 27.66 | 27.19 | 22.61 | 24.96 | |
| an | | 23.88 | 25.67 | 21.86 | 23.73 | 27.92 | 24.87 | |
| di | | 22.22 | 24.09 | 20.74 | 25.53 | 25.24 | 24.08 | |
| hy | | 19.19 | 3.18 | 14.34 | 4.71 | 7.02 | 11.64 | |
| fo | | 0.14 | 6.47 | 1.70 | 5.52 | 5.72 | 2.91 | |
| fa | | 0.18 | 5.97 | 2.30 | 5.63 | 4.66 | 2.92 | |
| mt | | 1.62 | 1.17 | 1.72 | 1.32 | 1.04 | 1.28 | |
| il | | 4.06 | 3.08 | 4.45 | 3.39 | 2.81 | 3.42 | |
| ap | | 0.73 | 0.52 | 0.81 | 0.59 | 0.47 | 0.62 | |

## TABLE 4: CHEMICAL ANALYSIS AND NORMS

| SAMPLE | | P1496-1 | P1496-3 | P1501-1 | P1501-2 | P1501-3 | P1501-4 | |
|---|---|---|---|---|---|---|---|---|
| **Wt%** | %error | | | | | | | Det. |
| $SiO_2$ | 0.45 | 50.53 | 49.93 | 50.88 | 50.62 | 50.17 | 50.29 | 0.73 |
| $TiO_2$ | 0.49 | 1.77 | 1.60 | 2.14 | 2.17 | 2.15 | 2.15 | 0.01 |
| $Al_2O_3$ | 0.88 | 14.54 | 14.47 | 14.04 | 14.23 | 14.04 | 13.95 | 0.24 |
| FeO* | 0.15 | 10.87 | 10.47 | 12.13 | 12.20 | 12.26 | 12.12 | 0.13 |
| MnO | 4.40 | 0.19 | 0.19 | 0.17 | 0.18 | 0.18 | 0.16 | 0.01 |
| MgO | 2.40 | 6.67 | 7.00 | 5.94 | 5.90 | 5.81 | 5.75 | 0.12 |
| CaO | 0.40 | 11.12 | 11.29 | 10.12 | 10.12 | 10.16 | 10.19 | 0.13 |
| $Na_2O$ | 1.48 | 2.89 | 2.83 | 3.00 | 3.17 | 3.08 | 2.97 | 0.24 |
| $K_2O$ | 1.77 | 0.54 | 0.53 | 0.57 | 0.62 | 0.53 | 0.56 | 0.04 |
| $P_2O_5$ | 2.80 | 0.26 | 0.24 | 0.29 | 0.30 | 0.30 | 0.29 | 0.01 |
| TOTAL | | 98.50 | 99.20 | 100.22 | 98.52 | 98.72 | 98.23 | |
| **ppm** | | | | | | | | |
| Ba | | 141 ± 8 | 119 ± 6 | 129 ± 7 | 94 ± 5 | 94 ± 5 | 102 ± 5 | 2.5 |
| Cr | | 49 ± 2 | 48 ± 2 | 48 ± 2 | 44 ± 1 | 42 ± 1 | 46 ± 1 | 2.0 |
| Cu | | 76 ± 5 | 73 ± 5 | 56 ± 4 | 51 ± 4 | 59 ± 4 | 58 ± 4 | 2.7 |
| Nb | | 19.8 ± 0.6 | 19.6 ± 0.6 | 19.1 ± 0.6 | 18.5 ± 0.6 | 19.5 ± 0.6 | 19.8 ± 0.6 | 0.5 |
| Ni | | 52 ± 3 | 61 ± 4 | 40 ± 3 | 36 ± 3 | 43 ± 3 | 36 ± 3 | 2.3 |
| Rb | | 9.3 ± 1.0 | 8.8 ± 1.0 | 9.1 ± 1.0 | 8.8 ± 1.0 | 9.3 ± 1.0 | 9.2 ± 1.0 | 2.1 |
| Sr | | 190 ± 6 | 202 ± 6 | 170 ± 5 | 170 ± 5 | 172 ± 5 | 169 ± 5 | 2.4 |
| V | | 364 ± 12 | 342 ± 11 | 393 ± 13 | 385 ± 12 | 390 ± 12 | 399 ± 13 | 1.1 |
| Y | | 32 ± 1.8 | 32 ± 1.9 | 42 ± 2.4 | 42 ± 2.4 | 42 ± 2.4 | 41 ± 2.3 | 2.3 |
| Zr | | 136 ± 2 | 126 ± 2 | 170 ± 3 | 170 ± 3 | 173 ± 3 | 170 ± 3 | 3.0 |
| **CIPW Norm** | | (wt%) | | | | | | |
| q | | 0.00 | 0.00 | 0.00 | 0.00 | 0.00 | 0.00 | |
| or | | 3.21 | 3.18 | 3.39 | 3.68 | 3.17 | 3.36 | |
| ab | | 24.58 | 24.28 | 25.54 | 26.92 | 26.38 | 25.50 | |
| an | | 25.23 | 25.56 | 23.29 | 22.85 | 23.19 | 23.41 | |
| di | | 23.52 | 24.39 | 21.01 | 21.24 | 21.47 | 21.57 | |
| hy | | 12.12 | 9.43 | 19.04 | 13.79 | 15.39 | 18.01 | |
| fo | | 3.01 | 4.28 | 0.62 | 2.27 | 1.73 | 0.75 | |
| fa | | 3.04 | 4.04 | 0.76 | 2.79 | 2.18 | 0.94 | |
| mt | | 1.30 | 1.21 | 1.59 | 1.62 | 1.64 | 1.63 | |
| il | | 3.38 | 3.08 | 4.09 | 4.14 | 4.13 | 4.14 | |
| ap | | 0.61 | 0.57 | 0.68 | 0.70 | 0.71 | 0.69 | |

## TABLE 4: CHEMICAL ANALYSIS AND NORMS

| SAMPLE | | P1501-S | P1502-1 | P1502-9 | P1504-1 | P1504-2 | P1505-1 | |
|---|---|---|---|---|---|---|---|---|
| **Wt%** | %error | | | | | | | Det. |
| $SiO_2$ | 0.45 | 49.97 | 50.11 | 50.16 | 49.94 | 49.70 | 49.95 | 0.73 |
| $TiO_2$ | 0.49 | 2.16 | 2.16 | 2.34 | 1.63 | 1.60 | 1.58 | 0.01 |
| $Al_2O_3$ | 0.88 | 13.98 | 13.87 | 13.94 | 14.67 | 14.83 | 14.66 | 0.24 |
| FeO* | 0.15 | 12.16 | 12.02 | 12.38 | 10.35 | 10.25 | 10.51 | 0.13 |
| MnO | 4.40 | 0.17 | 0.22 | 0.17 | 0.15 | 0.16 | 0.16 | 0.01 |
| MgO | 2.40 | 5.76 | 5.62 | 5.62 | 6.84 | 7.27 | 7.23 | 0.12 |
| CaO | 0.40 | 10.17 | 10.10 | 9.83 | 11.36 | 11.47 | 11.42 | 0.13 |
| $Na_2O$ | 1.48 | 3.32 | 3.27 | 3.29 | 3.14 | 2.97 | 2.89 | 0.24 |
| $K_2O$ | 1.77 | 0.56 | 0.57 | 0.69 | 0.57 | 0.53 | 0.47 | 0.04 |
| $P_2O_5$ | 2.80 | 0.29 | 0.32 | 0.32 | 0.23 | 0.22 | 0.21 | 0.01 |
| TOTAL | | 98.54 | 98.26 | 98.74 | 98.88 | 99.00 | 99.08 | |
| **ppm** | | | | | | | | |
| Ba | | 109 ± 6 | 105 ± 6 | 145 ± 8 | 94 ± 5 | 94 ± 5 | 102 ± 5 | 2.5 |
| Cr | | 46 ± 1 | 41 ± 1 | 47 ± 1 | 48 ± 2 | 63 ± 2 | 69 ± 2 | 2.0 |
| Cu | | 53 ± 4 | 60 ± 4 | 54 ± 4 | 63 ± 4 | 64 ± 4 | 71 ± 5 | 2.7 |
| Nb | | 19.5 ± 0.6 | 19.6 ± 0.6 | 24.5 ± 0.7 | 19.7 ± 0.6 | 17.5 ± 0.6 | 18.1 ± 0.6 | 0.5 |
| Ni | | 36 ± 3 | 42 ± 3 | 41 ± 3 | 50 ± 3 | 50 ± 3 | 54 ± 4 | 2.3 |
| Rb | | 9.0 ± 1.0 | 9.1 ± 1.0 | 11.2 ± 0.9 | 9.0 ± 1.0 | 8.9 ± 1.0 | 8.5 ± 1.0 | 2.1 |
| Sr | | 170 ± 5 | 178 ± 6 | 183 ± 6 | 196 ± 6 | 185 ± 6 | 186 ± 6 | 2.4 |
| V | | 380 ± 12 | 400 ± 13 | 413 ± 13 | 356 ± 11 | 343 ± 11 | 335 ± 11 | 1.1 |
| Y | | 41 ± 2.3 | 42 ± 2.3 | 43 ± 2.4 | 30 ± 1.8 | 30 ± 1.8 | 30 ± 1.8 | 2.3 |
| Zr | | 170 ± 3 | 170 ± 3 | 188 ± 3 | 122 ± 2 | 114 ± 2 | 115 ± 2 | 3.0 |
| **CIPW Norm** | | (wt%) | | | | | | |
| q | | 0.00 | 0.00 | 0.00 | 0.00 | 0.00 | 0.00 | |
| or | | 3.35 | 3.42 | 4.13 | 3.40 | 3.16 | 2.80 | |
| ab | | 28.48 | 28.12 | 28.16 | 26.85 | 25.37 | 24.66 | |
| an | | 21.88 | 21.82 | 21.47 | 24.50 | 25.80 | 25.84 | |
| di | | 22.72 | 22.42 | 21.41 | 25.45 | 24.79 | 24.52 | |
| hy | | 9.50 | 12.33 | 11.90 | 2.65 | 3.57 | 7.15 | |
| fo | | 3.37 | 2.33 | 2.62 | 6.32 | 6.68 | 5.37 | |
| fa | | 4.23 | 2.97 | 3.37 | 5.96 | 5.91 | 4.92 | |
| mt | | 1.63 | 1.64 | 1.69 | 1.20 | 1.14 | 1.20 | |
| il | | 4.16 | 4.17 | 4.50 | 3.13 | 3.07 | 3.03 | |
| ap | | 0.69 | 0.76 | 0.75 | 0.54 | 0.52 | 0.52 | |

## TABLE 4: CHEMICAL ANALYSIS AND NORMS

| SAMPLE | | CASM-3 | | | |
|---|---|---|---|---|---|
| **Wt%** | %error | | | | Det. |
| $SiO_2$ | 0.45 | **49.66** | | | 0.73 |
| $TiO_2$ | 0.49 | **1.30** | | | 0.01 |
| $Al_2O_3$ | 0.88 | **16.14** | | | 0.24 |
| FeO* | 0.15 | **8.72** | | | |
| MnO | 4.40 | **0.16** | | | 0.01 |
| MgO | 2.40 | **7.01** | | | 0.12 |
| CaO | 0.40 | **12.22** | | | 0.13 |
| $Na_2O$ | 1.48 | **2.32** | | | 0.24 |
| $K_2O$ | 1.77 | **0.40** | | | 0.04 |
| $P_2O_5$ | 2.80 | **0.18** | | | 0.01 |
| TOTAL | | **98.11** | | | |
| **ppm** | | | | | |
| Ba | | **93** | ± | 3 | |
| Cr | | **272** | ± | 8 | |
| Cu | | **80** | ± | 5 | |
| Nb | | **15.4** | ± | 0.5 | |
| Ni | | **59** | ± | 4 | |
| Rb | | **9.7** | ± | 1.0 | |
| Sr | | **198** | ± | 6 | |
| V | | **302** | ± | 10 | |
| Y | | **25.2** | ± | 1.3 | |
| Zr | | **98** | ± | 2 | |
| | **CIPW Norm** | (wt%) | | | |
| q | | 0.00 | | | |
| or | | 2.41 | | | |
| ab | | 20.00 | | | |
| an | | 33.04 | | | |
| di | | 22.52 | | | |
| hy | | 14.31 | | | |
| fo | | 2.15 | | | |
| fa | | 1.71 | | | |
| mt | | 0.92 | | | |
| il | | 2.52 | | | |
| ap | | 0.43 | | | |

*Iron Oxidation State*

Wet chemical iron analyses were obtained for 13 basalts from the Explorer Region (Michael and Chase, *in press*) The proportion of ferrous iron ($Fe^{2+}/Fe^*$, where Fe* is total Fe expressed as $Fe^{2+}$) vary inversely with degree of fractionation (Mg#) according to the following relation:

$$Fe^{2+}/Fe^* = 0.85 + 0.003*Mg\#$$

Mg# is the molecular ratio of 100Mg/(Mg+Fe*).

The values for FeO and $Fe_2O_3$ obtained using this relation were entered into the normative calculation. All of the basalts were determined to be hypersthene or olivine normative, while none of the basalts were determined to be quartz normative.

It is interesting to point out that when one applies Irving and Baragar's method of iron oxidation states (1971), 17 of the 25 samples are calculated to be quartz normative. Five samples were determined to be quartz normative applying the value of $Fe^{2+}/Fe^*=0.90$ (a commonly assumed oxidation value for MORBS) Thus, iron oxidation states should be determined analytically in order to obtain accurate normative results. Such determinations would also increase the accuracy of thermodynamic calculations, such as those discussed in Chapter 5.

## 4.1.2 MAJOR ELEMENT VARIATION

The overall major element variations in the sample suite are shown in a series of diagrams (figure 20) in which the wt% oxide analyses of each element are plotted against the wt% of MgO. The samples range from moderately fractionated (7.66 wt% MgO in sample P1491-1) to highly fractionated (5.44 wt% MgO in sample P1490-5).

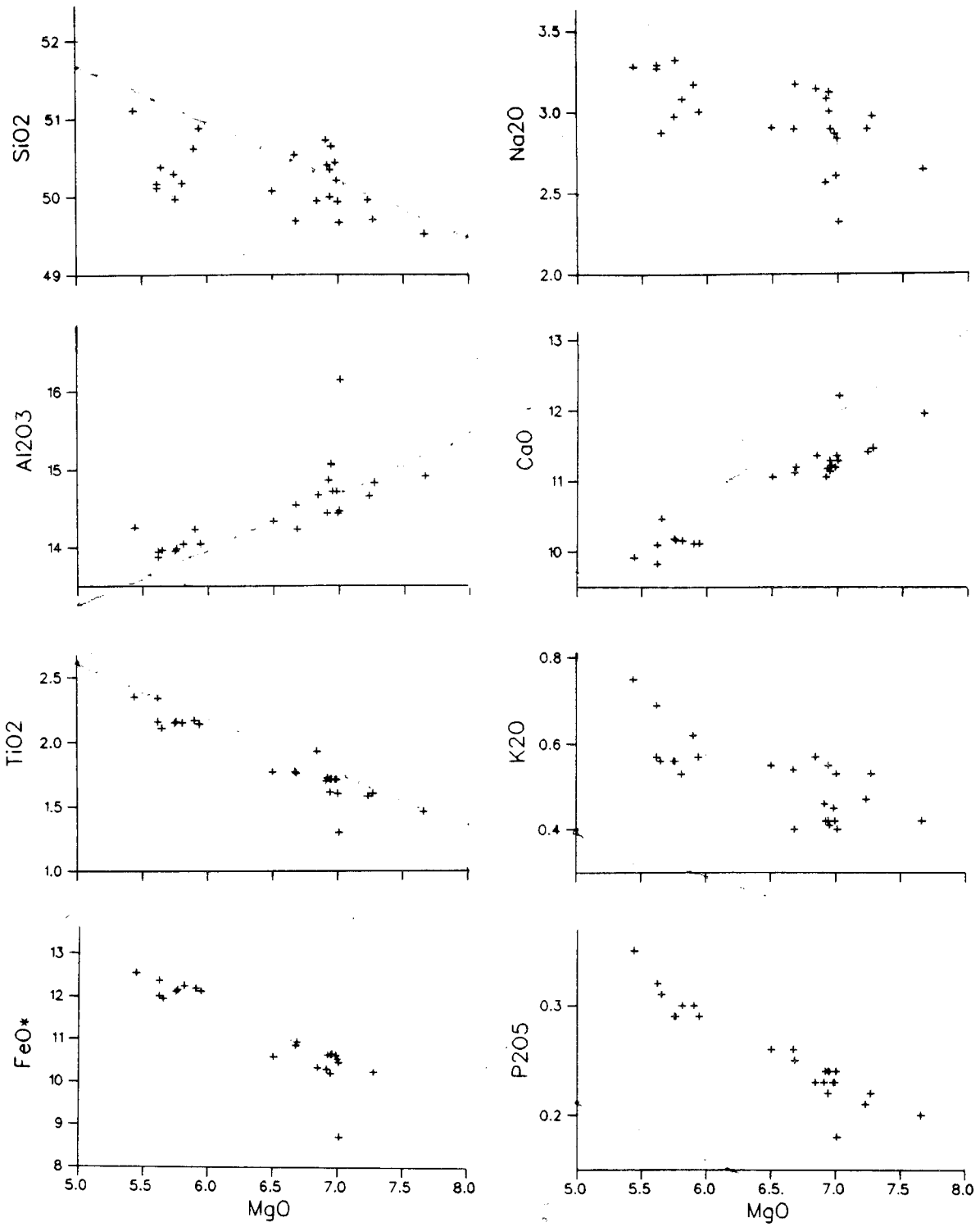


Figure 20: Major element variation diagrams (wt% oxide) for basalts from the MMA.

These compositional trends are very similar to those observed for basalts from the Galapagos Spreading Centre at 95° and 85°W (Byerly, 1980). Basalts from both the MMA and the Galapagos Spreading Centre have large enrichments in Fe and Ti. Byerly (1980) attributed these enrichments to extensive fractional crystallization of plagioclase and lesser amounts of clinopyroxene and olivine. The process of fractional crystallization will be examined in greater detail in Chapter 5.

The MMA basalts are more enriched than the Galapagos Spreading Centre rocks in incompatible elements such as K and P. Lavas from 91°W on the Galapagos Spreading Centre have similar incompatible element enrichments, however. These enrichments were attributed by Schilling *et al.* (1982) to the influence of the Galapagos hot spot nearby.

### 4.1.3 RESULTS: A COMPARISON OF MMA AND SER BASALT CHEMISTRY

The basalts sampled from the MMA include both the most fractionated and incompatible element enriched samples yet retrieved from the SER. Degree of fractionation and incompatible element enrichment of basalts sampled from various locations along the length of the SER are illustrated in figures 21 and 22, respectively. In these diagrams, a representative selection of 12 MMA samples are plotted along with analyses of 10 samples dredged from other locations along the SER during the CASM 5 expedition of July, 1985. The MMA sample points are located between 49°43' and 49°47'N latitude, indicated by the filled points in the figures. The magnesium, iron and titanium contents for the 10 CASM 5 samples were determined by electron microprobe analysis of fresh glass selvages by Tim O'Hearn at the Smithsonian Institute in Washington, D.C. (Michael and Chase, *in press*) The standardizations and instrument conditions were as specified by Melson *et al.* (1976). Niobium and zirconium were analysed by x-ray fluorescence in the same

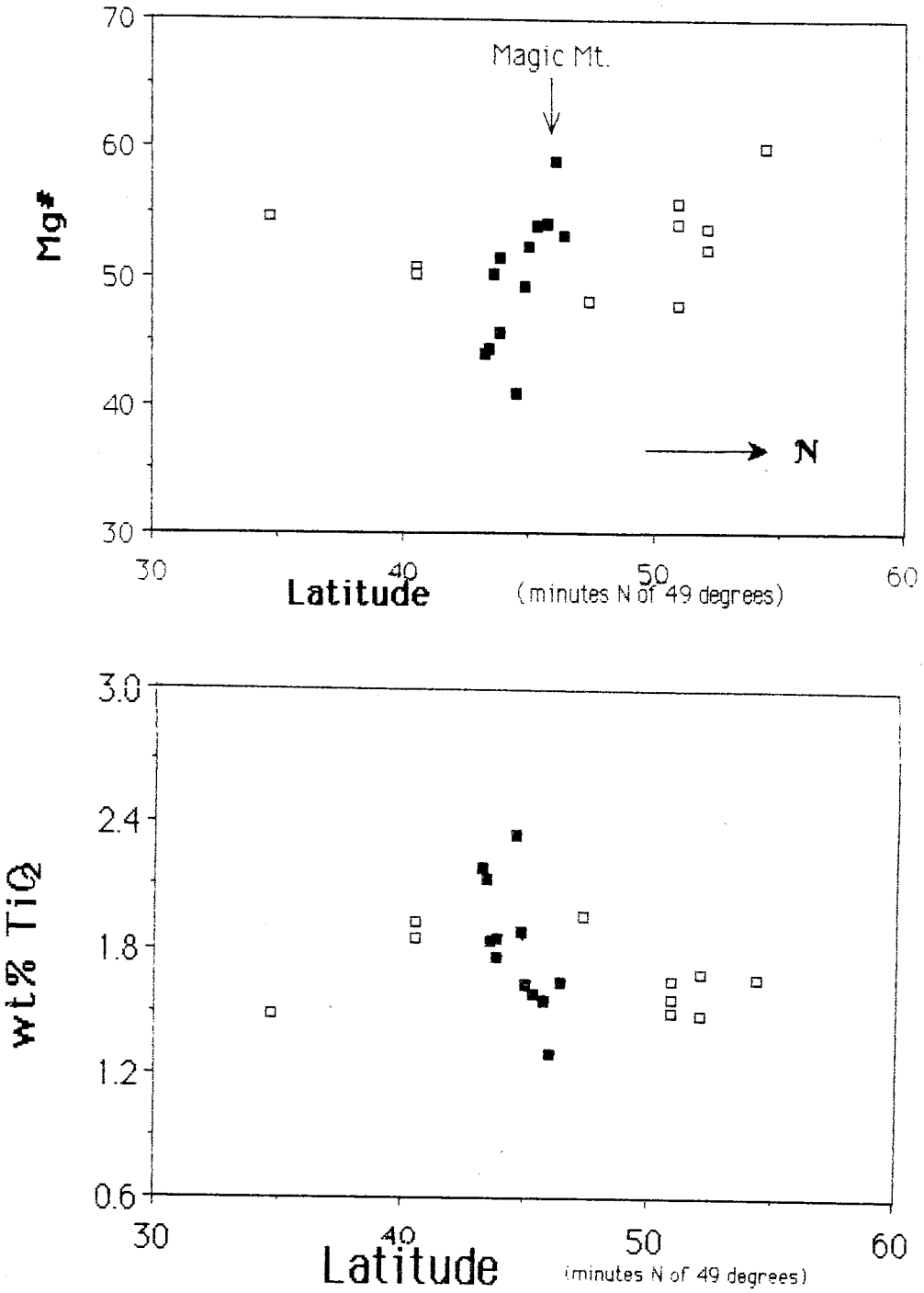


Figure 21: Chemical variations along axis indicating extent of fractional crystallization (see text); filled symbols for MMA basalts, open symbols for samples from other locations on the axis.

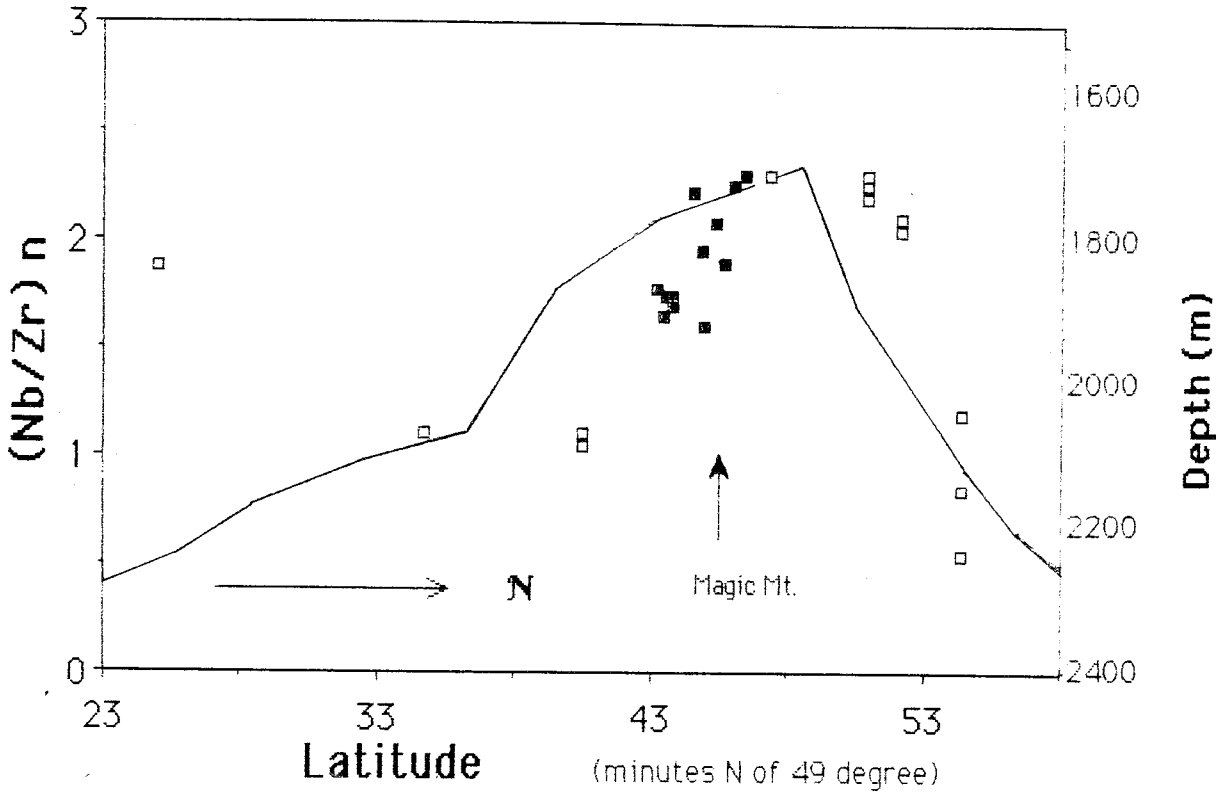


Figure 22: variation along axis of incompatible element enrichment as indicated by $(Nb/Zr)_n$ (see text); closed symbols represent MMA basalts; solid line represents axial depth.

run as the P1400 samples (P. J. Michael, *in review*).

In figure 21, the wt% $TiO_2$ and the Mg# were plotted against sample latitude as indices of the degree of fractional crystallization. The observed enrichment patterns are typical of propagating ridges. In studying the chemistry of lavas from a number of propagating ridges, Sinton *et al.* (1983) found that both the maximum degree of differentiation (i.e. highest wt% $TiO_2$, lowest Mg#) and the maximum degree of compositional variability occur within 50 km of the tip of a propagating ridge and thereafter diminish with increasing distance. Both these features are also observed in the MMA samples on the SER, supporting the conclusion of Botros and Johnson (1986) based on geophysical data that the SER is propagating northward (see Chapter 2). Magma diversity and fractional crystallization are discussed more thoroughly in Chapter 5.1

In figure 22, the chondrite-normalized Nb/Zr ratio (Nb/Zr)n is plotted against sample latitude. The chondritic Nb/Zr value used was 0.0059 (c.f. Sun *et al.*, 1979). Ratios of (Nb/Zr)n greater than 1.2 indicate significant extents of incompatible-element-enrichment. The MMA basalts are all enriched, having (Nb/Zr)n values between 1.2 and 2.4.

The depth profile along the crest of the SER is shown by the solid line in figure 15. There is good correlation between ridge height and the normalized Nb/Zr ratio. As in figure 21, both the maximum values and the greatest variability in values are observed in the MMA. This pattern may be in part due to an increased sample density in the MMA. This possibility can only be evaluated by obtaining more samples from other locations along the ridge axis.

It is interesting to note, however, that within the MMA itself there is a systematic increase in the Nb/Zr ratio with decreasing ridge depth. Moving from the

south of the study area where a normal ridge axial valley is present, the Nb/Zr values increase to the north where the ridge shoals and sheet flows become more abundant. These changes could reflect the increasing contribution of incompatible element enriched magmas from a mantle plume just north of the study area. The evidence for a mantle plume and for ridge propagation will be discussed further in Chapter 6.

## 4.2 MINERAL CHEMISTRY

Mineral analyses by electron microprobe were obtained for 11 of the 25 samples from the study area. Precision estimates ($2\sigma$) from repeated analyses of mineral standards were 0.5 mole % An for plagioclase and 0.4 mole % Fo for olivine. The $2\sigma$ precision estimate for the Mg# of clinopyroxene was 0.7.

A representative selection of plagioclase, clinopyroxene and olivine analyses are included in tables in Appendix E. This appendix also includes details on the analysis and data reduction. The plagioclase and clinopyroxene analyses are represented visually in ternary diagrams in figures 23 and 24, respectively. The measured plagioclase compositions are compared with the calculated equilibrium compositions in figure 33 in Chapter 5. Diagrams for individual samples are included in Appendix E. In the following discussion of mineral chemistry, the plagioclase compositions cited in the text have the analysis number provided in brackets to allow for reference to the mineral tables in Appendix E.

### 4.2.1 FELDSPAR CHEMISTRY

Feldspar compositions ranged from An 49.8 (microphenocryst core, P1491-1, anal. #15) to An 88.0 ('xenocryst' core, P1488-3, anal. #1). The analyses are most concentrated in the ranges An 68 to 71 and An 78 to 82 (figure 23). The low An range corresponds to the core compositions of the skeletal equilibrium

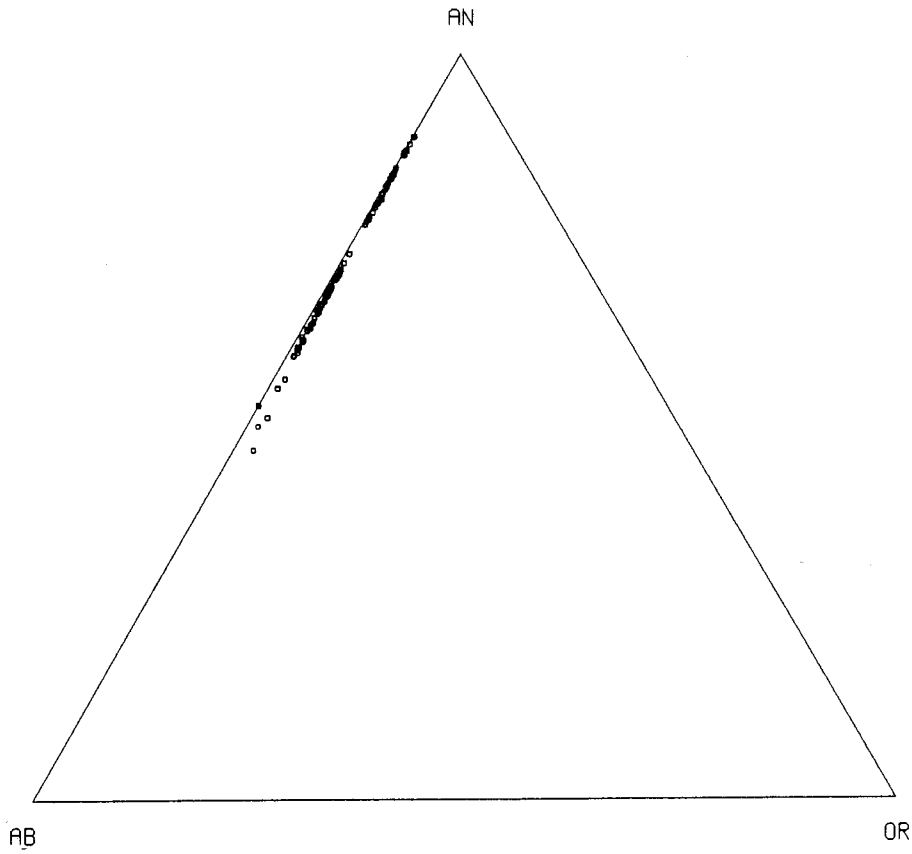


Figure 23: Ternary composition diagram for 118 plagioclase analyses.

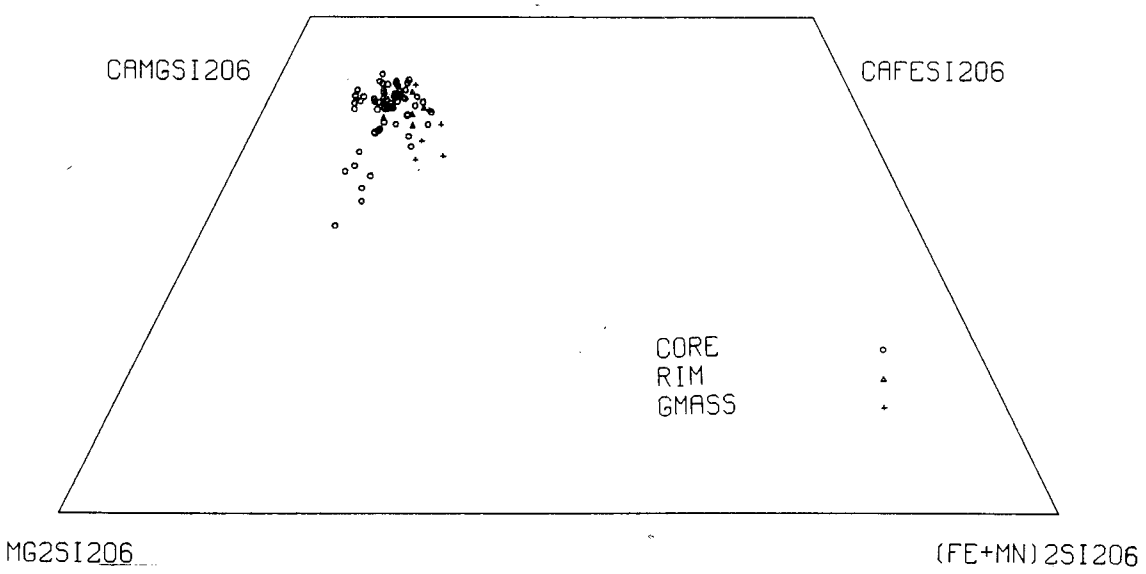


Figure 24: Ternary composition diagram for 75 clinopyroxene analyses.

microphenocrysts observed throughout the sample suite. The latter range corresponds to core compositions of the xenocrysts found in some of the samples (Chapter 3 and figure E-1, Appendix E).

Normal zoning of 4 to 10 mole% An is often observed in both microphenocrysts and phenocrysts in thin outer rims (50 to 300 $\mu$m). The xenocrysts tend to have similar zonation patterns with larger overall compositional ranges. For example, in sample P1490-4, a well formed optically zoned phenocryst is observed with an An 82 core (#7) and an An 65 rim (#9) (figure 16). The rim compositions are usually close to the compositions of the microlites in the groundmass. This zonation is indicative of changing magma composition, probably due to fractional crystallization (see Chapter 5.1). In sample P1491-1, plagioclase crystals with complex chemical zoning and disequilibrium textures are observed (figure 33, Chapter 5). Similar properties in plagioclase xenocrysts were cited as evidence of magma mixing in lavas from the Mid-Atlantic Ridge at 45° N by Kuo and Kirkpatrick (1982). A more detailed discussion of magma mixing is provided in Chapter 5.3.

Of the 118 plagioclase analyses obtained, none had An contents between An 71.5 and 78. This may reflect a short time of residence in an environment with temperature and pressure conditions between those forming the high and low An samples, or a slow growth rate in such an environment.

The $K_2O$ content in the feldspars ranges from 0.02 to 0.23 wt%. This produces 0.10 to 1.31% orthoclase (Or) component. The Or component varies inversely with the An component.

Contents of $FeO_T$ range from 0.40 to 1.10 wt%, varying inversely with An content. Magnesium content ranges from 0.10 to 0.35 wt% MgO, varying directly

with An content. Most of the iron present in basaltic plagioclases is in the trivalent form, substituting for Al in the tetrahedral site, whereas the magnesium and divalent iron substitute for calcium in the octahedral site (Deer *et al.*, 1966). In table E-1, the ternary feldspar components were calculated with all the iron as trivalent iron.

### 4.2.2 PYROXENE CHEMISTRY

The pyroxenes are all augites. The measured CaO contents ranged from 15.6 to 21.5 wt%. The Mg# generally decreases from core to rim within a grain. Measured values ranged from 85.5 to 70.2. The lowest Mg#s (highest iron contents) were measured in groundmass microlites of some of the more fractionated samples. Chromium contents ranged from 0.05 to 0.50 wt% $Cr_2O_3$, varying systematically with Mg#.

Significant amounts of $TiO_2$ (0.4 to 1.92 wt%) and $Al_2O_3$ (1.4 to 6.65 wt%) were measured, occurring most abundantly in microlites and microphenocryst rims, although core-rim chemical variations are irregular in most grains. This variation may result from rapid, poorly ordered crystal growth caused by variations in cooling rate and degree of supercooling (Grove and Bence, 1977). Nearly vertical composition trends in the ternary diagrams, such as those observed in many of the MMA samples (figure E2, Appendix E), were proposed by Smith and Lindsley (1971) to occur during quenching of a basaltic melt.

### 4.2.3 OLIVINE CHEMISTRY

Microphenocryst core compositions of olivine range from Fo 73 (P1490-5) to Fo 83.5 (CASM3), varying systematically with the Mg# of the sample. Compositions vary little within and between grains of individual samples.

Normal zoning (approx. 1 to 2.5 Fo) is commonly observed in rims less than 20 μm thick. The largest zonation measured was from an Fo 80.8 mantle to an Fo 68.7 rim observed over an 8 μm distance (sample 904). These rims are observed partially surrounding fine matrix crystals and thus appear to be formed during rapid crystallization following extrusion.

MnO contents range from 0.05 to 0.47 wt%. Most crystals have between 0.2 and 0.3 wt% MnO, varying directly with iron content. CaO contents range from 0.27 to 0.44 wt% and show no relationship to iron or magnesium content. NiO contents (determined for the CASM 4 samples only) were observed to range from 0.05 to 0.16 wt%. There is no correlation with Fo content.

# 5. PETROGENESIS

The primary goal of this petrogenetic analysis is to determine the extent to which petrographical and petrochemical variations, as described in the preceeding two chapters, reflect magma diversity in the MMA. The process of fractional crystallization is examined in some detail. Evidence for magma mixing will also be discussed. In section 5.1, the samples are separated into groups which are closely located and share common petrographic and chemical features. Samples from each group are tested to see if they can be related by fractional crystallization. In section 5.2, the observed phase compositions and the crystallization sequences inferred from petrography are compared with those predicted from thermodynamic calculations. Evidence for magma mixing is presented in section 5.3.

## 5.1 FRACTIONAL CRYSTALLIZATION AND MAGMA DIVERSITY

### 5.1.1 ELEMENT RATIO DIAGRAMS

Petrographic and mineralogical evidence suggest fractional crystallization occured in many MMA samples (c.f. Chapters 3 and 4.2). Fractional crystallization was initially evaluated by using element-ratio diagrams (Pearce, 1968). An explanation of the design and use of these diagrams is provided in Appendix F.

Appropriate chemical indices were chosen for the fractionation of various combinations of the three observed phases: plagioclase, clinopyroxene and olivine (Russell and Nicholls, 1987). For each test, the fractionation index is plotted on the y axis. Si/K, an index of total silicate fractionation, is plotted on the x axis. Thus, if the test index describes the chemical effects of all of the phases fractionating from the magma, the sample analyses will plot as a series of points on a line with a slope of one. If the index does not describe the effects of the fractionating phases, a line with a slope less than one results.

**Table 5: Slopes from Element Ratio Fractionation Tests**

| Test | Index (vs. Si/K) | Calc. Slope ±3SD |
|---|---|---|
| plag alone | 2(Na+Al)/K | 0.555 ± 0.055 |
| cpx alone | (2Ca+Na-Al)/K | 0.319 ± 0.046 |
| oliv. alone | 1/2(Fe+Mg)/K | 0.198 ± 0.015 |
| plag &/or cpx | (2Ca+3Na)/K | 0.875 ± 0.090 |
| plag &/or oliv | (plag+oliv)/K | 0.753 ± 0.072 |
| plag &/or cpx &/or oliv | (2Ca+3Na+oliv)/K | 1.070 ± 0.099 |

Initially, the MMA samples were analysed in a series of tests for fractional crystallization of one, two and three-phases. The indices used for each test, as well as the calculated slopes of each trend are listed in table 5.

A slope of 1.07 in the three-phase test indicates that all three-phases are involved in fractional crystallization. The slopes of the other tests indicate that the proportions of fractionating phases (largest to smallest) were plagioclase, clinopyroxene and olivine. This is the same order of abundance observed petrographically in the basalts (Chapter 3).

There is significant scatter in the data of the three-phase test (3SD = 0.099) in the element-ratio diagram, figure 25. It is possible that a variety of different source magmas or extents of melting of the MMA basalts, indicated by

various incompatible trace element enrichments (Chapter 4.1), may account for the scatter of points in figure 25. To evaluate this possibility, groups of samples that may be comagmatic are identified. General criteria are used to establish the first order magma diversity of these sample groups followed by a series of tests to determine diversity within these groups.

a) First Order Magma Diversity

By examining figure 26, determining the number of distinct magmas sampled in the MMA is possible. The possibility also exists to determine which samples may or may not be related by fractional crystallization. In this diagram, wt% $K_2O$ is plotted as index of fractionation against (Nb/Zr)n as index of source chemistry. A very similar pattern was produced when Mg# was used as the fractionation index.

*$(Nb/Zr)_n$ as an Index of Source Chemistry*

Both Nb and Zr are highly incompatible trace elements with mineral/melt partition coefficients $<0.1$ for plagioclase, clinopyroxene and olivine in basaltic melts (Pearce and Norry, 1979). Thus, samples with significantly different Nb/Zr ratios cannot be related by fractional crystallization. Such variations reflect variations in source chemistry or differences in partial melting.

For extents of source melting greater than 10% (i.e. characteristic of tholeiite production), strongly and moderately incompatible trace elements are not fractionated from each other. Therefore, the Nb/Zr ratio of source and derived magmas are approximately the same. In this case, the variations in Nb/Zr reflect different extents of incompatible-element-enrichment of the source. However, Nb is preferentially partitioned into the melt compared to Zr when there is less than 5% melting of the source region (Erlank and Kable, 1976). Thus a high Nb/Zr ratio could reflect incompatible-element-enrichment in the source and/or small extents of source melting.

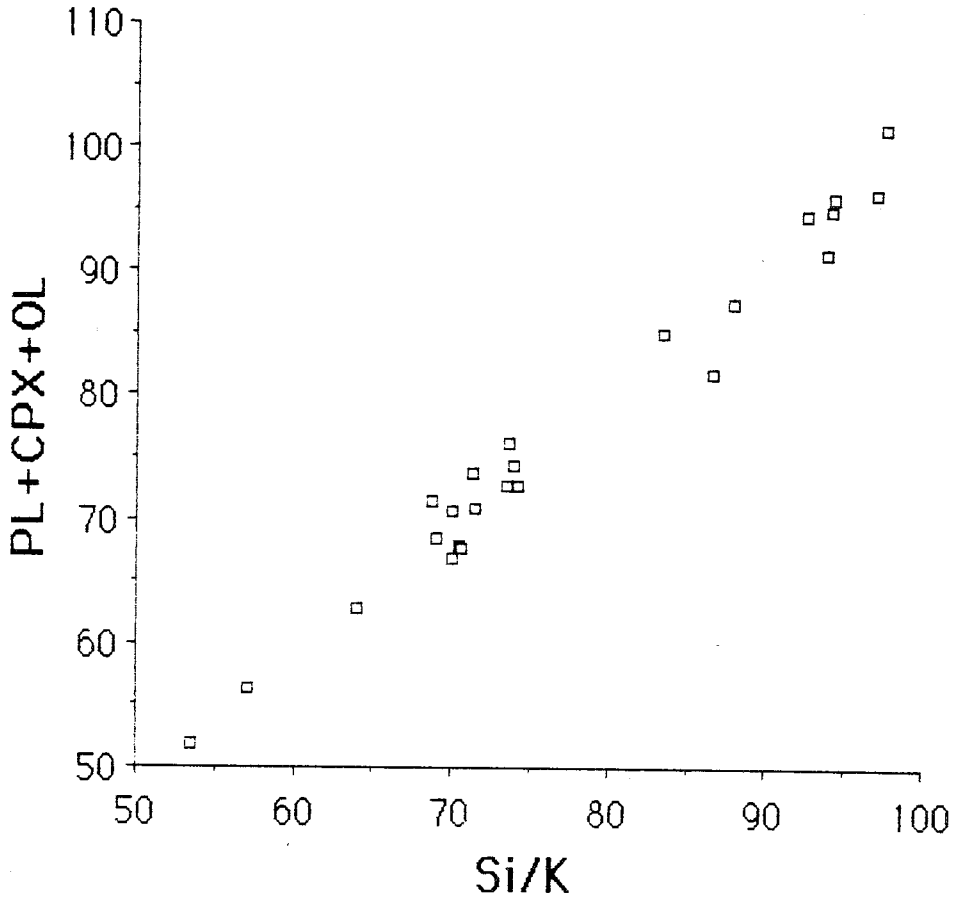


Figure 25: element ratio diagrams: test of three phase fractionation for 25 basalts from the MMA.

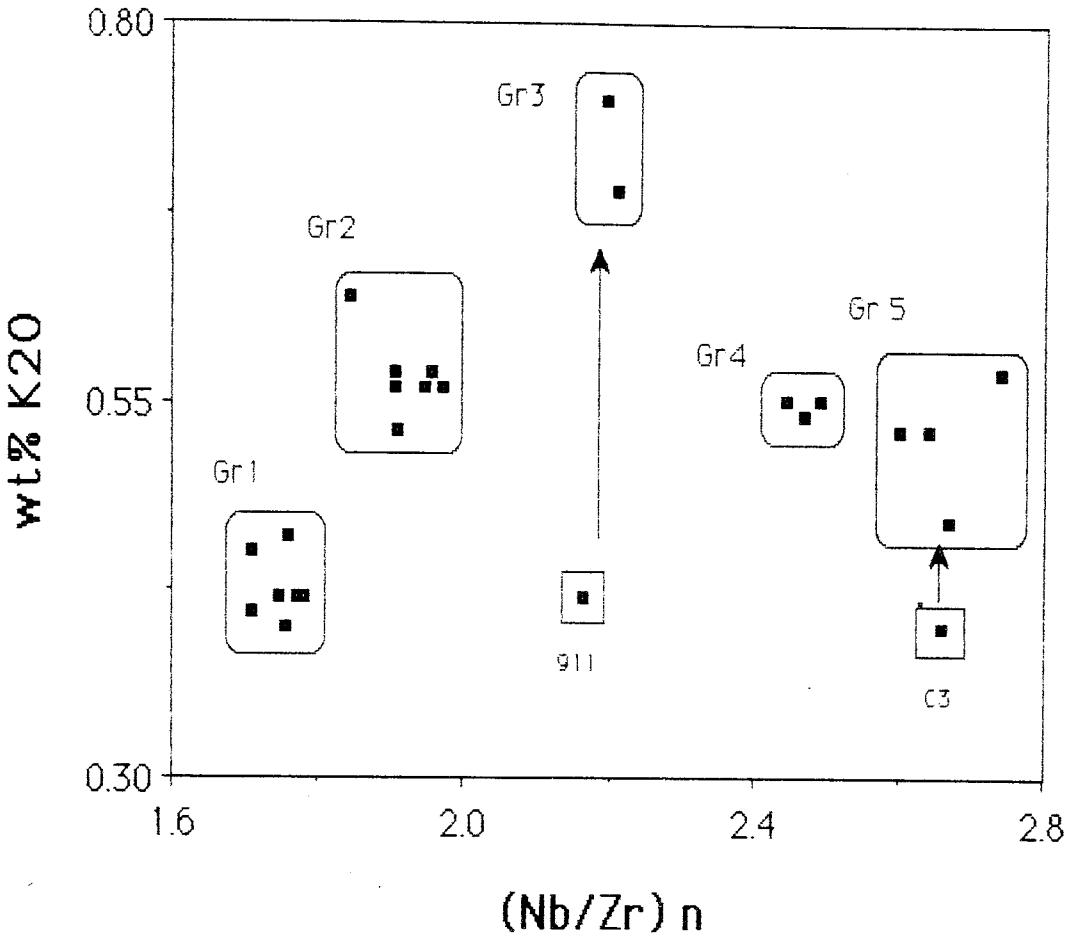


Figure 26: variation of degree of fractionation (wt% $K_2O$) with extent of incompatible element enrichment of source ((Nb/Zr)n) for 25 basalts from the MMA. There are at least 5 distinct magma types (see text).

Samples with ratios which differ by more than 10% are not likely to be comagmatic. Thus, the wide range in enrichment values indicate that the MMA samples are derived from two or more sources. The range in values could result from either production from several discrete sources or products of mixing between two end members.

In figure 26, a comagmatic series of rocks related by fractional crystallization would define a vertical series of points; least fractionated at the bottom to most fractionated at the top of the diagram. Most of the points cluster into five groups, with the least fractionated samples, P1491-1 and CASM-3, as discrete points. Similar patterns were obtained with other fractionation indices such as 1/Mg#, wt% $P_2O_5$ or Ni/Nb plotted against trace element-ratios that vary little through fractionation (eg. Y/Nb or Rb/Nb).

Individual samples have been labelled in figures 27 and 28 to enable their location on the map (figure 4), the petrographic summary (table 4), and in the tables of chemical analyses (tables 4, E1, E2 and E3). The sample numbers have been abbreviated to the last three digits: for example, 041 refers to sample P1504-1 and 941 refers to P1494-1.

The basalts of each group in figure 26 have differences in incompatible element enrichments (Nb/Zr) less than analytical uncertanties. This indicates that the samples within each group may be comagmatic. However, careful observation of element-ratio diagrams reveal a diversity of magmas within each of these groups.

b) Second Order Magma Diversity

Three-phase fractionation tests for samples from each groups 1, 2 and 4 are represented in figure 28. Again, as in figure 26, the points are labelled for ease of

comparison with other data. The points which fall on lines with a slope of one can be related by fractional crystallization. Points that fall significantly away from any fractionation lines can not be so related. In order to determine the variation in the element ratio diagrams attributable to analytical uncertainty, 6 replicate analyses of the basalt standard BHVO (c.f. Appendix C) were plotted in figure 27. The points define a trend with a slope of 0.88 ± 0.10. The standards deviation in the y axis values was 0.17; the standard deviation in the x values was 0.19. This indicates that many apparent chemical differences between samples may in fact be artifacts of analytical uncertainty. Since there is co-variance in the error, the analytical uncertainty is indicated is better represented with an eliptical error envelope than by vertical and horizontal error bars. Consequently, 1 $\sigma$ error envelopes from the 6 replicate analyses are shown in the diagrams in figures 28 and 29. Points with overlapping error envelopes are possibly related by fractional crystallization. The size of the error envelopes observed in figures 27 to 29 may be redused by using a more precisely measured element in the denominator of the ratio such as Zr. Variations in Zr are also less likely to reflect variations in source enrichment than are variations in K.

In the following discussion, results from the element-ratio diagrams are compared with differences in sample petrography and location to determine the minimum number of magma types which make up each sample group.

**Group 1**

Five of the seven group 1 samples, 881-4 and 891, are 'moderately phyric olivine rich' basalts, as described in Chapter 3, with total modal amounts of crystal phases between 1.8 and 4.5 % (c.f. table 2). In figure 28, samples 882 and 883 define a line with a slope of one and can be related by fractional crystallization. Samples 891, 881 and 884 fall within the error envelope of the defined trend and thus may possibly be related by fractional crystallization.

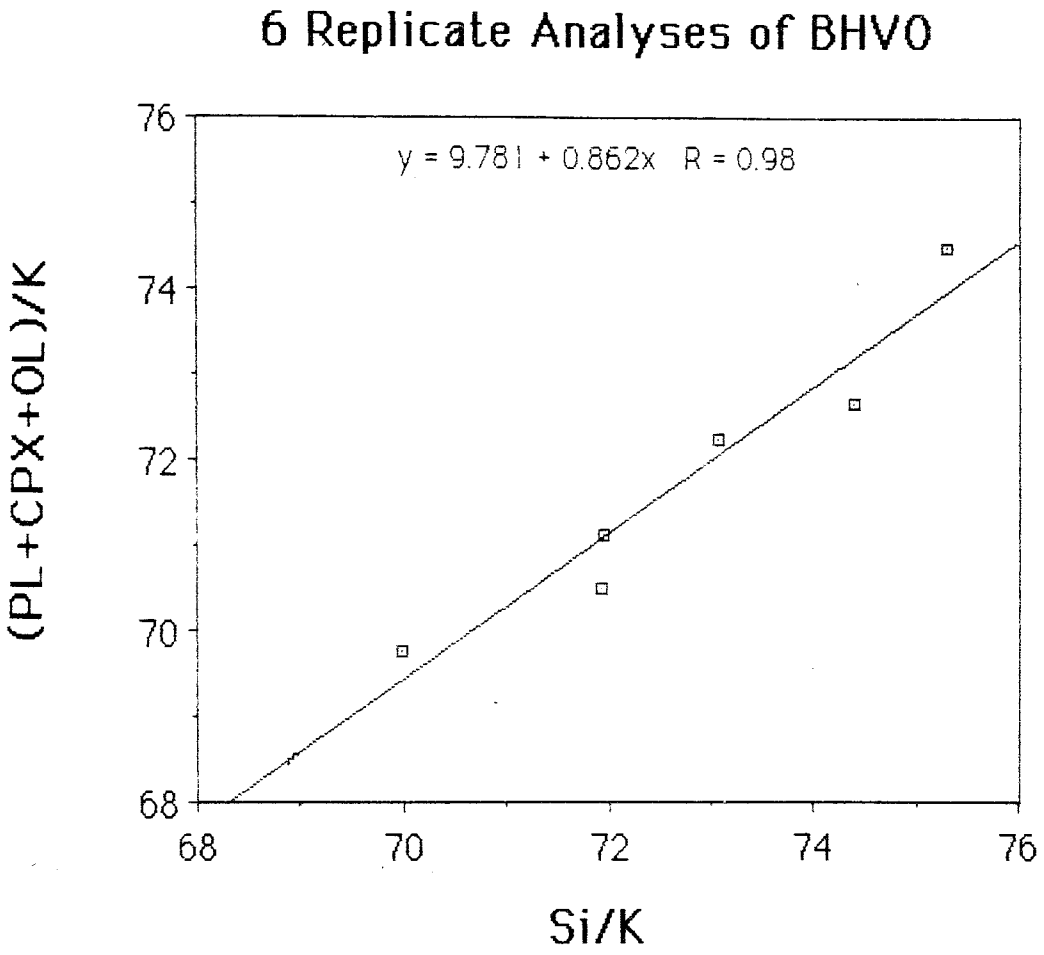


Figure 27: analytical error represented in element-ratio diagrams: test of three-phase fractionation for 7 replicate analyses of basalt standard BHVO.

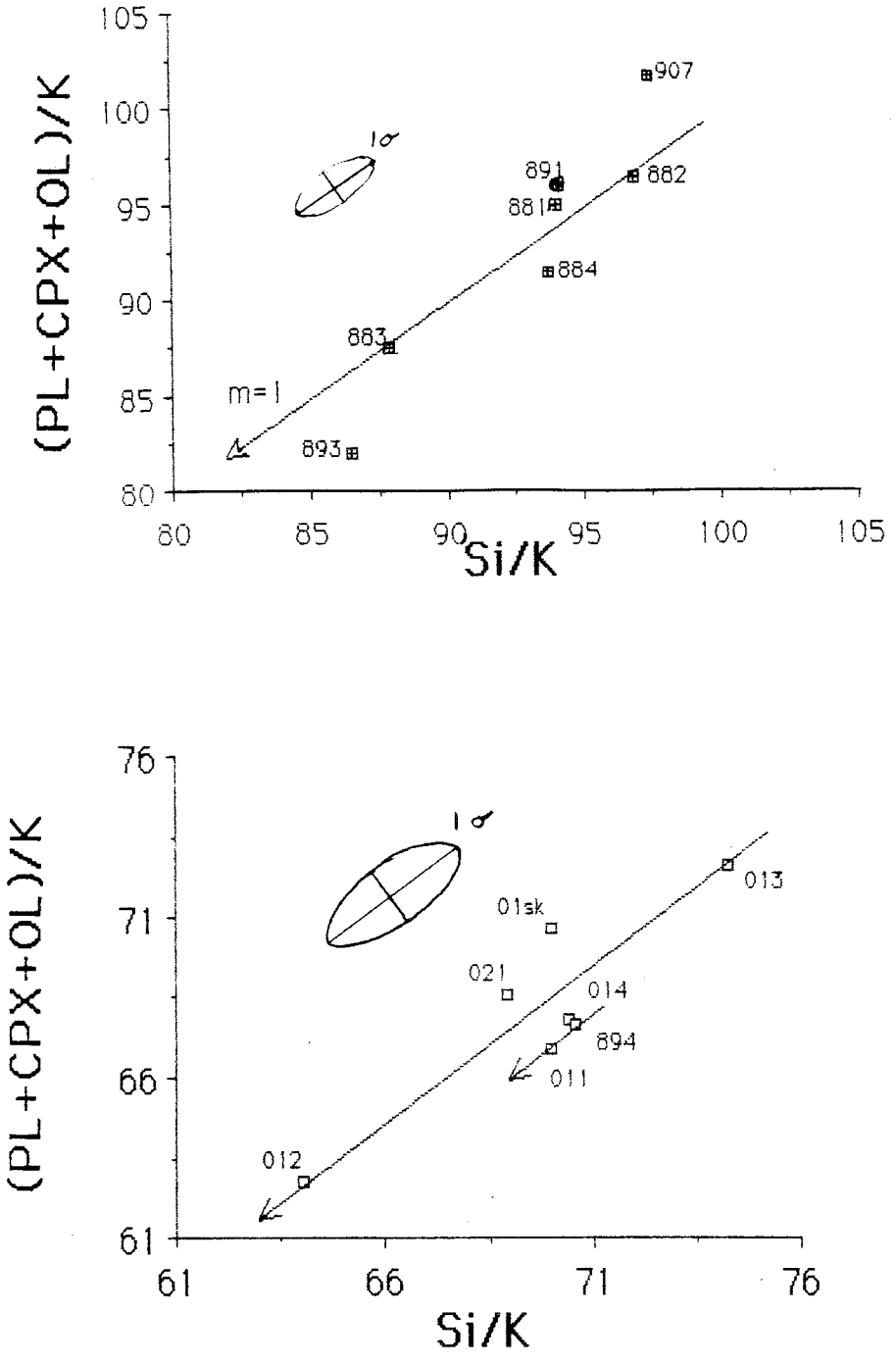


Figure 28: 3 phase fractionation tests for group 1 samples (upper figure) and group 2 samples (lower figure).

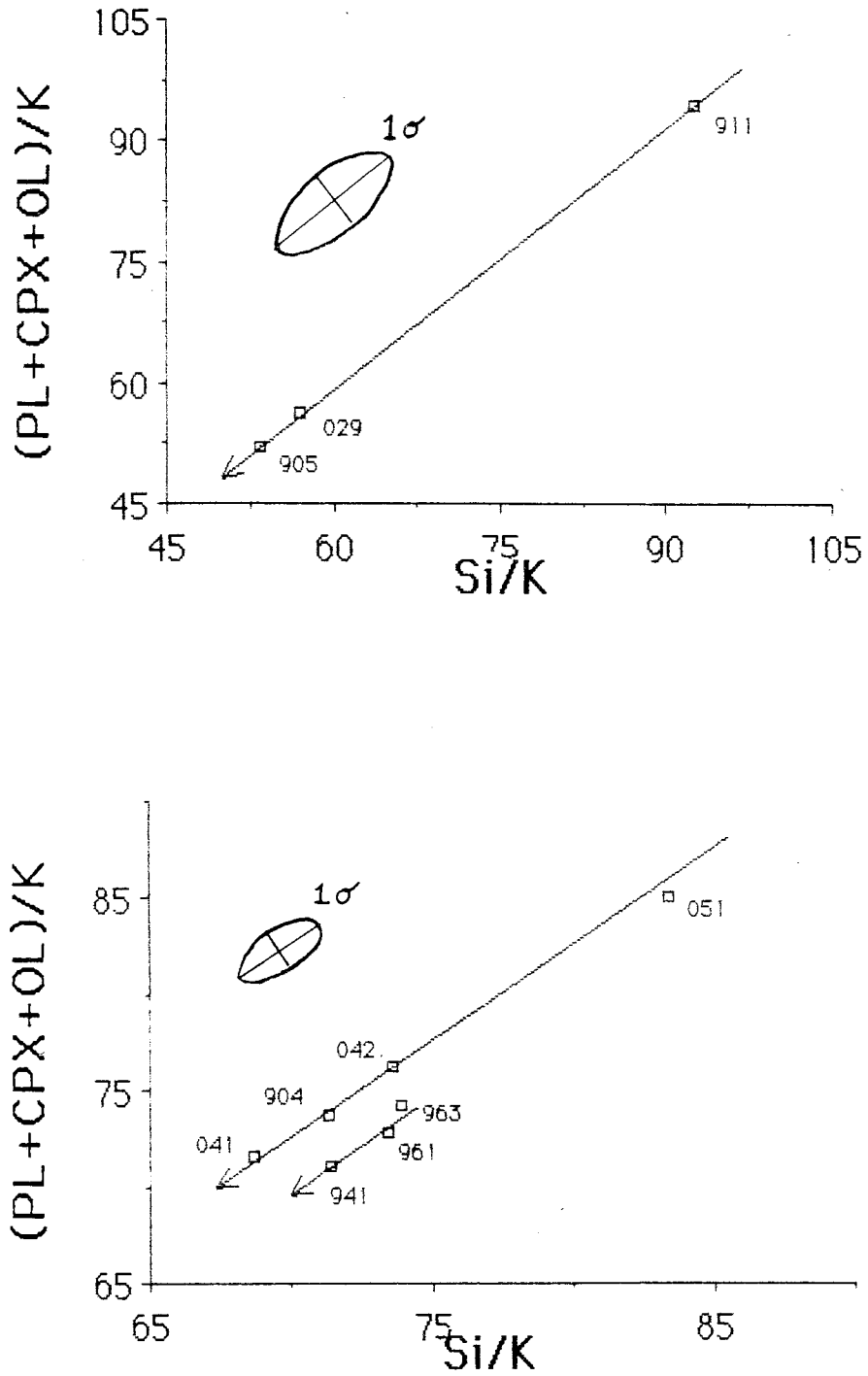


Figure 29: 3 phase fractionation tests for group 3 samples (upper figure) and group 4 and 5 samples (lower figure).

Both samples 893 and 907 define discrete points, indicating that neither sample is comagmatic with any of the 88 series samples. This finding is not unexpected because both of these samples are petrographically distinct from the other five in the group. Sample 893 has only 0.3% modal phenocryst comprised entirely of plagioclase. Sample 907 has more clinopyroxene than olivine, with some clinopyroxene glomerocrysts present. Furthermore, these samples are located over 700 m away from the five other samples and each other. Since lava flows rarely extend beyond 200 m (based on submersible observations), one is unlikely to find samples, located farther than 500 m apart, that are comagmatic.

The analysis of the three-phase fractionation test with sample petrography and location shows that the group 1 samples are derived from at least three distinct magmas.

**Group 2**

There are seven samples in group two. Sample 894, a pillow basalt of the 'moderately phyric pyroxene rich' type, is a skid sample located away from the six other group 2 samples which are fresh glassy lobate flows of the 'aphyric' type. The six samples appear to be quite close in petrography and location. Examination of figure 28 reveals samples 012 and 013 define a line with a slope of one. The other samples fall within the error envelope on either side of this trend. Samples 021 and 01Sk are possibly related to 012 and 013 as are samples 014 and 011. Sample 01sk is not likely related to 011 and 014, however. Furthermore, sample 894 is not related to the other samples due to its distinctive petrography and location. Thus, the group 2 magmas are derived from a minimum of three distinct magmas.

**Group 3**

The group 3 samples (029 and 905) are of the 'moderately phyric pyroxene rich' type with very similar whole rock and mineral chemistry (c.f. Appendix E). They are also very closely located and are thus possibly from the same flow. They can be related by fractional crystallization to sample 911 as a parent.

**Groups 4 and 5**

The seven samples of group 4 and 5 are from the northern half of the study area within the vicinity of Magic Mountain. Two petrographic types are observed in the group 4 samples:

1. Samples 941 and 961 are located within 10 m of each other on the side of Magic Mountain and are very similar petrographically and chemically. They may be from the same flow.
2. Sample 904 is of 'moderately phyric pyroxene rich' type and is located over 2.5 km south of 961. Thus it is not likely comagmatic. Furthermore, it falls significantly off the trend defined by the other Group 4 samples in figure 29.
3. All of the Group 5 samples (041, 042, 051 and 963) are lobate flows of 'aphyric' type. Sample 963 is located over 3 km northeast of sample 041. Although the samples are fairly widely separated, they are chemically and petrographically quite similar and thus may all be of the same type.

**Samples 911 and CASM-3**

Samples 911 and CASM-3 are the least evolved basalts sampled from the MMA. The incompatible element enrichments in these samples indicate that they may be parental to the samples in group 3 and group 5, respectively (figures 26 and 28).

Thus, the 25 samples of the study area are derived from at least 10 distinct magmas, based on sample chemistry, petrography and location.

The element-ratio diagrams were also plotted with phosphorus as the incompatible element in the denominator of the fractionation indices. These diagrams demonstrated the same inter-sample relationships as were observed in diagrams in figures 27 and 28, indicating that the relationships between samples are not a result of analytical errors.

### 5.1.2 MASS-BALANCE TESTS OF FRACTIONATION

Samples believed to be related by fractional crystallization were subjected to mass-balance tests. These tests serve to further evaluate the fractional crystallization hypothesis and to calculate the amount of each phase that is fractionating. A detailed description of the construction and use of the mass-balance test is presented in Appendix.

The results of 23 fractionation tests are summarized in table 6. For each test the following are listed:

1. the proposed parent and daughter samples.
2. the amounts of plagioclase, clinopyroxene and olivine subtracted from (or added to) the parent composition to best approximate the composition of the daughter sample.
3. the results of the three criteria used to evaluate tests (the criteria are described in Appendix F).

*Test Results*

Each group of tests in table 6 is arranged in order of best to poorest fit, as determined by the test criteria. Successful tests (indicated by '+' sign in table 6) met all three criteria. Marginal tests (±) met the criteria for the SRS and either the K or Ti residuals, while failed tests (-) met one or none of the criteria.

**Table 6: Mass-balance Fractionation Test Results**

| Test | Parent | Daughter | Result[1] | Frac. Phases[2] | | | Criteria for Tests[3] | | |
|---|---|---|---|---|---|---|---|---|---|
| | | | | PLAG | CPX | OLIV | Ti res. | K res. | SRS |
| | | | *Tests on Duplicates* | | | | | | |
| 1 | 905 | 905 | + | 1.2 | -0.2 | 0.7 | .041 | .034 | .065 |
| 2 | 883 | 883 | + | 1.3 | 1.5 | 0.1 | .027 | .008 | .048 |
| 3 | 891 | 891 | + | 0.5 | 0.6 | 0.4 | .016 | .015 | .012 |
| | | | *Tests on Samples Within Group 1* | | | | | | |
| 4 | 883 | 882 | + | 0.4 | -0.1 | 0.3 | .015 | .044 | .005 |
| 5 | 883 | 881 | + | 1.1 | -1.8 | 0.6 | .010 | .032 | .028 |
| 6 | 883 | 884 | + | 0.2 | -2.4 | 0.5 | .020 | .020 | .054 |
| 7 | 883 | 891 | + | 0.3 | -1.1 | 0.2 | .005 | .034 | .057 |
| 8 | 883 | 907 | - | 2.3 | 0.9 | 0.6 | .009 | .061 | .379 |
| 9 | 883 | 893 | - | 1.5 | -1.8 | 1.3 | .029 | .010 | .475 |
| | | | *Tests on Samples Within Group 2* | | | | | | |
| 10 | 012 | 021 | + | 1.3 | ---- | 0.9 | .031 | .055 | .044 |
| 11 | 01sk | 021 | + | 0.7 | ---- | 0.7 | .024 | .004 | .076 |
| 12 | 012 | 013 | + | 0.2 | ---- | 0.8 | .051 | .023 | .091 |
| 13 | 011 | 894 | - | -0.6 | ---- | 0.2 | .020 | .008 | .193 |
| | | | *Test on Samples Within Group 3* | | | | | | |
| 14 | 029 | 905 | + | 0.6 | 0.6 | 0.8 | .055 | .036 | .031 |
| | | | *Tests on Samples Within Group 4* | | | | | | |
| 15 | 961 | 941 | + | 0.1 | -0.8 | 0.5 | .015 | .017 | .017 |
| | | | *Tests on Samples Within Group 5* | | | | | | |
| 16 | 042 | 041 | + | 2.5 | 0.6 | 1.5 | .038 | .016 | .034 |
| 17 | 051 | 963 | + | 1.4 | 0.0 | 0.8 | .007 | .053 | .044 |
| 18 | 042 | 051 | - | 2.0 | 0.2 | 0.5 | .065 | .075 | .052 |
| | | | *Tests Between Group 5 Samples and CASM3* | | | | | | |
| 19 | C-3 | 963 | + | 17.3 | 5.7 | 1.8 | .063 | .014 | .110 |
| 20 | C-3 | 051 | ± | 16.2 | 5.6 | 1.1 | .055 | .023 | .145 |
| 21 | C-3 | 042 | - | 14.4 | 5.4 | 0.7 | .001 | .032 | .271 |
| | | | *Tests Between Group 3 Samples and 911* | | | | | | |
| 22 | 911 | 905 | ± | 18.8 | 16.3 | 4.0 | .131 | .046 | .080 |
| 23 | 911 | 029 | ± | 18.6 | 16.0 | 3.5 | .166 | .022 | .054 |

[1] quality of fit; + = good, ± = poor on one criteria, - = poor fit: see text.
[2] grams of mineral phases removed from 100g of parent comp. to best approx. daughter comp.: see Appendix F.
[3] differences between observed and predicted daughter comp. SRS = the sum of the square of all the residuals: see Appendix F.

A good correspondence of results exists between the mass-balance tests and the element-ratio diagrams. For some tests, the amounts of fractionated phases and residuals are equal or less than those of the duplicate tests (1 to 3). The precision of the analyses indicates that some samples are not geochemically distinguishable from each other and may be samples of the same flow. The following sample pairs fall into this catagory:

1. group 1: tests 4 to 7
2. group 2: tests 10 to 12
3. group 3: test 14
4. group 4: test 15
5. group 5: tests 16 and 17

Moderate to good fits were also obtained in the element-ratio diagrams for each of these cases. Conversely, the samples that were significantly off trend with each other in the element-ratio diagrams rendered un-acceptable results in mass-balance tests. This correspondence of failed test results is illustrated with the failed mass-balance tests (8, 9, 13, 18 and 21) listed in table 6.

The conclusions made previously regarding the number of different magma types on the basis of sample location, petrography and element-ratio diagrams are corroborated by mass-balance test results.

Additional conclusions drawn from the analysis of the mass-balance tests are as follows:

1. group 5: Samples 042 and 051 cannot be related by fractional crystallization (test 18). However, 051 can be related to 963 (test 17).
2. CASM3 to group 5: The group 5 samples can be related by fractional crystallization to CASM-3 as a parent (tests 19 and 20), although CASM-3 falls off the trend defined by the group 5 samples in the element-ratio diagram in

figure 25.

3. 911 to group 3: The group 3 samples can be related by fractional crystallization in both tests to P1491-1 as a parent (figure 29).

In the last 5 tests, where CASM3 and 911 are tested as parent samples, there are extents of fractionation that are greater than 5%. In each case, the calculated proportions of fractionating phases are quite close to the petrographically observed phase proportions thereby supporting the hypothesis: MMA basalts undergo three-phase fractionation of plagioclase with lesser amounts of clinopyroxene and olivine.

In the section following, thermodynamic calculations are used to predict the crystallization order of phases and their equilibrium compositions through fractional crystallization.

## 5.2 THERMODYNAMIC MODELLING

The program DUHEM (Russell and Nicholls, 1985) utilizes the work of Ghiorso *et al.* (1983) to model the early crystallization history of mafic and intermediate lavas. From the whole rock composition, which approximates the melt composition in aphyric and sparsely phyric rocks, the program calculates the saturation temperature and compositions of the solid phases as a function of pressure.

The variations in saturation temperature with pressure are represented by the liquidus curves for samples P1502-9 and P1505-1 in figures 30 and 31. The calculated liquidus phase relations are similar in both cases. The order of crystallization through cooling varies with pressure as shown in figures 30 and 31. This calculated crystallization order can be compared with the order inferred from petrographic observations (table 2) to approximate the crystallization pressure.

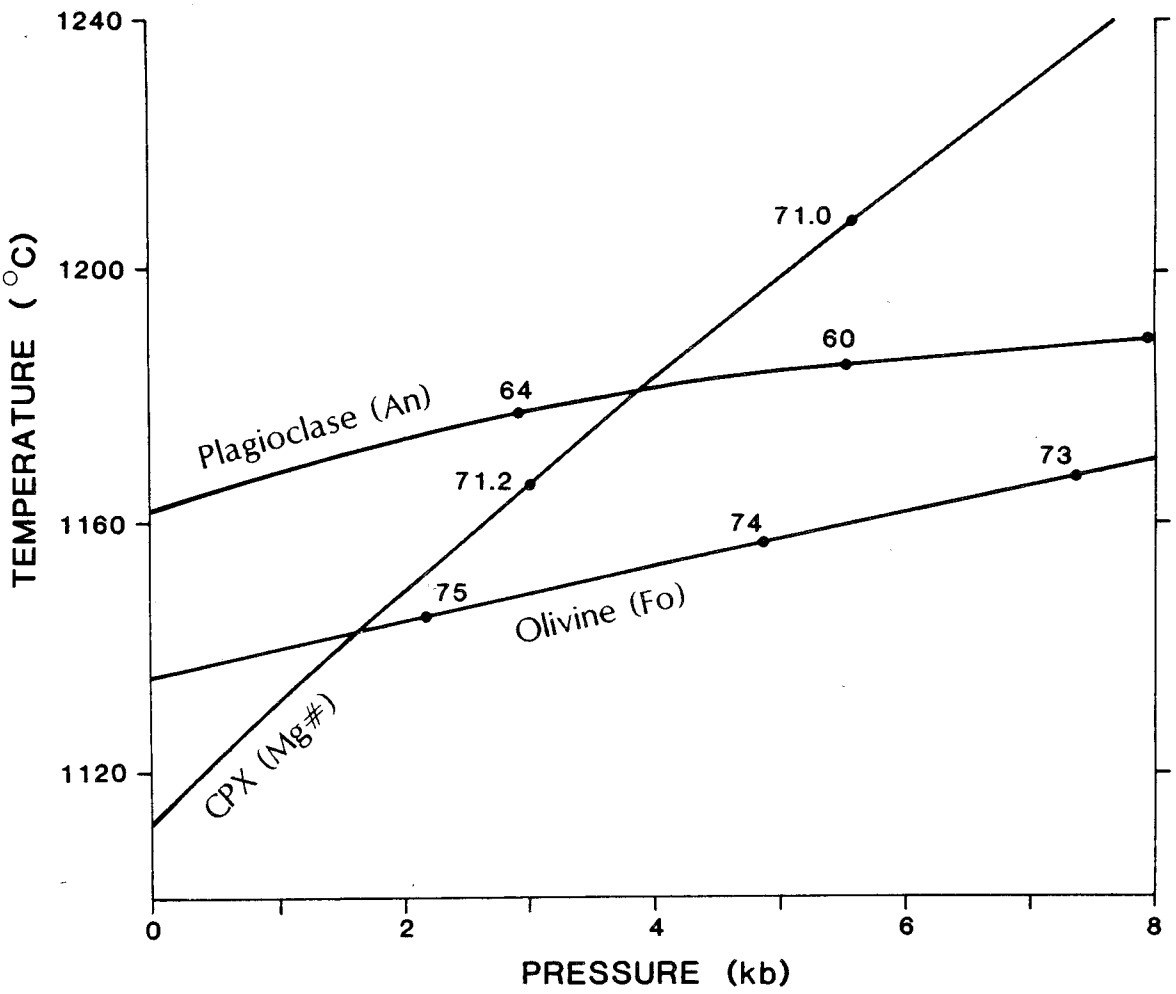


Figure 30: Sample P1502-9 (FeTi basalt): P-T liquidus relations calculated using Duhem's Theorem from whole rock composition. Observed concentration order and phase compositions closest to those predicted at 1.5±0.5 kb The effect of pressure on mineral composition is greatest for plagioclase and least for clinopyroxene (see text).

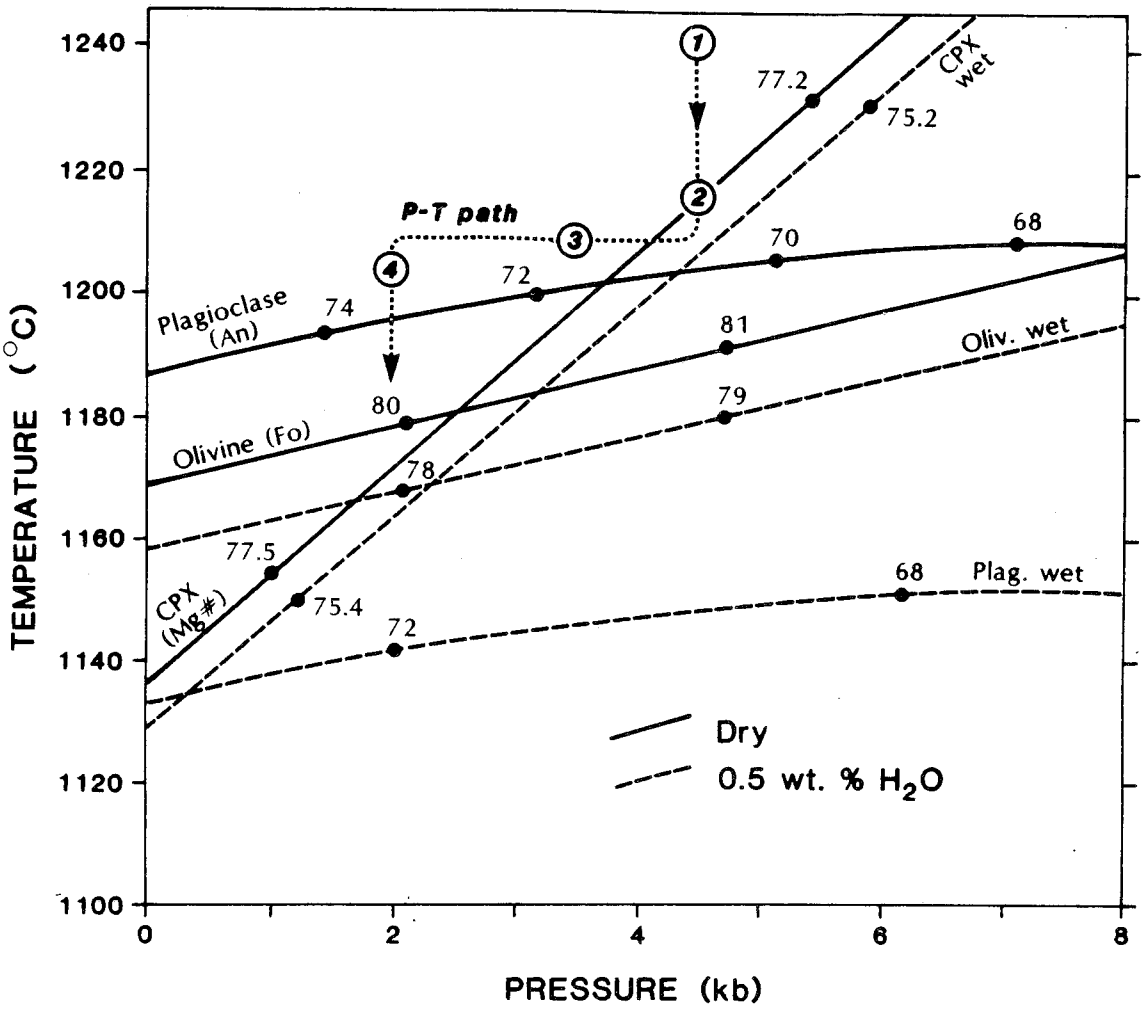


Figure 31: Sample P1505-1: P-T liquidus relations calculated using Duhem's Theorem for both anhydrous whole rock composition (solid lines) and for compositions bearing 0.5 wt% water (long dashes). The short dashed line represents a possible P-T path to explain the formation of early formed clinopyroxene phenocrysts (see chapter 6).

The liquidus temperatures for each sample are listed with the measured and predicted plagioclase and olivine compositions in table 7. The core compositions are also listed for each type or generation of crystal.

The measured clinopyroxene compositions (Table E2) have Mg# values $5.3 \pm 1.1$ higher than predicted values. The model predicts results for end member clinopyroxene compositions but, in fact, the clinopyroxenes in these rocks contain large amounts of $Al_2O_3$ (up to 6.65 wt%) and $TiO_2$ (up to 1.92 wt%). Aluminum and Ti may be incorporated as a result of rapid crystal growth during quenching of the lava upon eruption. This may explain the inaccuracy of predicted clinopyroxene compositions by the computer model. The model is still useful, however, in predicting the occurrence or non-occurrence of clinopyroxene. For these reasons, the predicted liquidus temperatures for clinopyroxene are included in table 7.

Three parameters affecting the predicted liquidus phase compositions and temperatures are: pressure, water content and oxygen fugacity.

***i) Pressure***

As seen in figures 29 and 30, dP/dT of the saturation curves for all three solid phases is positive although the pressure effect on the liquidus temperature is greater for clinopyroxene than it is for plagioclase or olivine. Therefore, the crystallization order varies significantly with pressure. In figure 30, the predicted order of crystallization at 1 kb is plagioclase - olivine - clinopyroxene; at 3 kb is plagioclase - clinopyroxene - olivine, and at 5 kb is clinopyroxene - plagioclase - olivine. The crystallization order inferred from petrography is plagioclase followed by clinopyroxene which is followed closely by olivine. Thus the inferred crystallization pressure for sample P1502-9 is around 1.5 kb. Since liquidus relations and phase compositions vary during the course of fractional crystallization, inferred crystallization

pressures are only accurate to within 1 kb.

The observed crystallization order in sample P1505-1 is plagioclase - olivine followed closely by clinopyroxene. The observed phase composition and crystallization order is best matched by predicted results at a pressure of 2 kb. In fact most of the MMA samples tested had optimal matches between predicted and observed results at pressures between 1.5 and 2 kb. This pressure corresponds to crustal depths between 4 to 6 km. The predicted compositions and orders of crystallization (at 2kb) for each sample are compared with the observed results in table 7.

A large corroded tabular clinopyroxene phenocryst was observed in sample P1505-1. This crystal, which has a primitive composition (Mg# = 84.5), may have formed during an early period of clinopyroxene crystallization at higher pressures (eg. 3 to 4 kb). Such pressures correspond to crustal thickness estimates of 8 to 10 km obtained from seismic data (Malacek and Clowes, 1978). The significance of this result is discussed further in Chapter 6.

The calculated liquidus compositions in figures 29 and 30 are plotted at intervals along the liquidus curves of each phase: mole % An for plagioclase, mole % Fo for olivine and Mg# for clinopyroxene. The pressure effect on mineral composition is greatest for plagioclase and least for clinopyroxene. In sample P1505-1 (figure 31) the change in equilibrium mineral compositions from 2 to 8000 bars is: $\Delta An = -8.2$, $\Delta Fo = +2.4$ and $\Delta Mg\#(cpx) = +0.6$.

***ii) Water Content***

If the dissolved water content of the magma is increased, the liquidus temperature of each phase is lowered. This effect is greatest for plagioclase, as observed in figure 31. The calculated water-free liquidus curves are represented by solid lines and long-dashed lines represent the liquidus curves with the measured $H_2O$ content

**Table 7: Summary of Calculated and Observed Phase Compositions**

| Sample | Liquidus T (°C)[1] | | | Calculated Comp.[2] | | Observed Comp.[3] | |
|---|---|---|---|---|---|---|---|
| | PLAG | OLIV | CPX | An | Fo | An | Fo |
| P1488-3 | 1194 | 1174 | 1169 | 72.2 | 79.4 | x: 88.2<br>p: 78.7 | 80.8 |
| P1490-4 | 1198 | 1174 | 1152 | 72.9 | 79.7 | x: 82.4<br>m: 69.9 | 80.8 |
| P1490-5 | 1174 | 1147 | 1137 | 65.0 | 72.8 | m: 65.4 | 73.1 |
| P1491-1 | 1202 | 1190 | 1181 | 75.8 | 81.9 | x: 49.8<br>p: 83.5<br>m: 68.3 | x:65.6<br>m: 83.2 |
| P1494-1 | 1189 | 1170 | 1162 | 71.1 | 78.2 | p: 81.2<br>m: 71.0 | 80.8 |
| P1496-1 | 1191 | 1165 | 1169 | 71.3 | 77.8 | m: 77.0 | 80.2 |
| P1496-3 | 1194 | 1174 | 1174 | 72.6 | 79.7 | x: 78.3<br>m: 81.9 | |
| P1501-2 | 1178 | 1149 | 1151 | 66.7 | 74.7 | m: 70.5 | 76.6 |
| P1501-4 | 1179 | 1144 | 1154 | 66.9 | 74.3 | m: 70.5 | |
| P1502-1 | 1177 | 1139 | 1153 | 65.9 | 73.7 | m: 68.3 | 76.2 |
| P1504-1 | 1194 | 1168 | 1173 | 72.3 | 79.2 | x: 80.9<br>m: 65.8 | 82.5 |
| P1504-2 | 1197 | 1182 | 1174 | 73.8 | 80.5 | p: 80.9 | 81.7 |
| P1505-1 | 1196 | 1179 | 1173 | 73.3 | 80.1 | m: 80.3 | 82.5 |
| CASM-3 | 1221 | 1178 | 1176 | 78.3 | 82.2 | p: 85.8<br>m: 71.2 | 83.9 |

[1] calculated liquidus temperatures (2kb dry).
[2] calculated liquidus phase compositions (2kb dry).
[3] observed core compositions; x = xenocryst, p = phenocryst, m = microphenocryst.

of 0.5 wt% (Michael and Chase, *in press*). The plagioclase liquidus temperatures are consistently about 55°C lower through the range of pressures for the water bearing solution than the anhydrous solution. However, the liquidus temperature depression for olivine and clinopyroxene are only 10°C and 7°C, respectively.

A significant change in the order of crystallization exists between the dry and hydrous magmas. In sample P1505-1 and the other samples tested, plagioclase is the first forming phase from the dry magma at crustal pressures (0 to 3.5 kB). In contrast, the tests including 0.5 wt% water as a component revealed plagioclase to be the second to last or the last forming phase. However, plagioclase is the first formed phase in the MMA basalts and is often the only phenocryst phase observed (table 2).

These observations indicate that the thermodynamic model does not predict phase relations in hydrous melts accurately. This may be due to lack of sufficient experimental data in hydrous conditions available to Ghiorso *et al.* (1983) (J.K. Russell, *pers. comm.*) For this reason, the calculations summarized in table 7 were made on a water free basis.

As observed in the compositions on the liquidus curves, increased water content results in lower An, Fo and Mg#(cpx) values.

***iii) Oxygen Fugacity***

Changes in the oxygen fugacity have a minor effect on liquidus temperatures and equilibrium phase compositions. For example, in sample P1505-1, raising the oxygen fugacity slightly (log $fO_2$ = -8.79 from -9.57) lowers the liquidus temperature of each phase between 0.5 and 1°C.

This has very little effect on the order of crystallization. The compositional effects of this slight increase in oxygen fugacity were: $\Delta An = +0.2$, $\Delta Fo = +0.35$ and $\Delta Mg\#(cpx) = +0.35$. Calculations were done using the FeO and $Fe_2O_3$ values determined by the equation of Michael (*pers. comm.*) as described in Chapter 4.

***Results of DUHEM Calculations***

As shown by the liquidus temperatures in table 7, the model predicts:

1. Plagioclase is the first forming phase.
2. Olivine and clinopyroxene usually appear close together in the cooling history, after a substantial interval of plagioclase formation (10 to 30 C°). The predicted order of crystallization at pressures between 1.5 and 2.0 kb is similar to the order obtained from petrographic observations.

### 5.2.1 CHANGE IN MELT PROPERTIES DURING FRACTIONATION

By applying Duhem's Theorem, determining the liquid line of descent with increasing extents of fractional crystallization is possible. In so doing, it is also possible to calculate changes in physical properties of the melt during fractionation, such as density ($\rho$) and dynamic (or kinematic) viscosity ($\nu$).

These calculations were done on a series of compositions, derived by fractional crystallization, from sample P1505-1 (P=1kb). The variation of mineral-melt density contrast with dynamic viscosity (log $\nu$) of the melt as fractional crystallization proceeds is indicated in figure 32. The curves are generated by plotting the density contrast values ($\Delta\rho = \rho_{min} - \rho_{melt}$) against the log of the dynamic viscosity values for residual melts after each increment of fractional crystallization. The final values (to the right in each curve) correspond to a derivative liquid with a composition very similar to the most fractionated FeTi basalts of the MMA (samples P1490-5 and P1502-9). The physical properties were calculated using the program

ROCK by Dr. J. Nicholls of the University of Calgary. From this diagram two important observations are made:

1. Plagioclase is initially only slightly less dense than the host liquid. The density contrast increases during the course of crystallization. Thus, some of the plagioclase glomerocrysts observed could be floatation cumulates.
2. The density of the mafic phases olivine and clinopyroxene are significantly greater than the density of the host liquids. The density contrast for the mafic phases, olivine in particular, increases substantially over the course of fractionation. If the increase in density contrast is not offset by the concurrent increase in dynamic viscosity of the melt, the efficiency of gravitative separation is enhanced. This may explain the scarcity of olivine microphenocrysts in the more fractionated samples of the MMA and the accumulation of plagioclase in other samples (such as CASM-3).

***Discussion***

Elthon (1984) has observed that oceanic basalts often contain greater than cotectic proportions of plagioclase. This was also observed to be the case for some of the MMA samples (eg. CASM3, 904). Elthon proposed that plagioclase in axial magma chambers separates much more slowly from the host liquid than do the co-crystallizing olivine and clinopyroxene, because the plagioclase is much closer in density to the co-existing liquid than are the mafic phases. The results of the modelling depicted in figure 32 confirm the findings of Elthon.

Staudigel and Bryan (1981) have demonstrated that significant variations in mineral distributions occur on the scale of 2 to 5 cm in individual cooling units of ocean basalt lavas. These variations were attributed to gravitative differentiation (i.e. accumulation of plagioclase and settling of clinopyroxene and olivine) and dynamic flow sorting during which the concentration of crystals in the centre of a flow unit

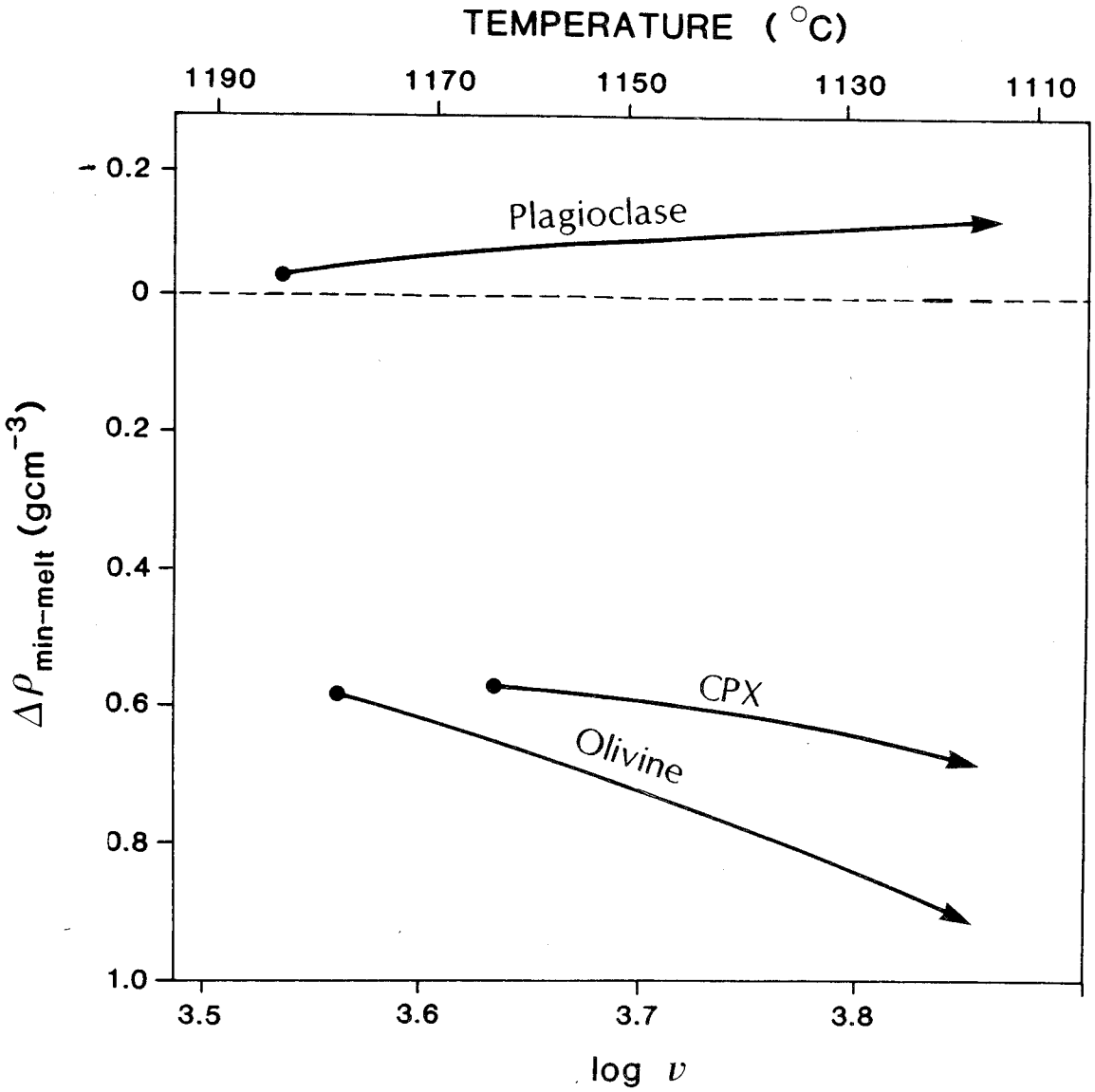


Figure 32: Sample P1505-1: Calculated mineral-melt density contrasts ($\Delta\rho$) between plagioclase, clinopyroxene and olivine and the residual liquid during low pressure fractional crystallization. The density contrasts are plotted against the temperature and dynamic viscosity ($\nu$) of the magma (see text).

is increased. This selective sorting must occur within hours of extrusion, depending on the thickness of the flow unit.

The size of the compositional variations within the cooling units observed by Staudigel and Bryan (1981) were large enough to "warrant caution in attaching special petrogenetic significance to magma batches or chemical types based on whole rock data alone". Thus, many of the compositional differences between comagmatic samples in the MMA (Chapter 5.1) may be attributed to flow differentiation rather than fractional crystallization in a magma reservior. Recent work by Sparks and Huppert (1984) suggests that the density of basaltic melts varies during the course of fractional crystallization depending on the order and amounts of phases forming. Such variations govern the stratification and mixing of different magmas more than do thermal effects. Further investigation along this line may prove worthwhile in order to better understand magma mixing.

***Summary***

The major results of the thermodynamic calculations are as follows:

1. Most crystallization occured between 4 and 6 km beneath the ridge axis.
2. Including water contents in the calculations has the effect of depressing the liquidus temperatures of all crystallizing phases, especially plagioclase. The extent of this effect is not, at present, well known.
3. Changes in oxygen fugacity have only minor effects on calculated equilibrium phase compositions.
4. When the calculations are made on a water free basis, the model accurately predicts the order and proportion of mineral phases formed during crystillization.
5. Calculated changes in mineral-melt density contrasts during fractional crystallization may, in part, explain the accumulation of plagioclase glomerocrysts and the scarcity of olivine microphenocrysts.
6. Late stage flow differentiation may account for some of the compositional variations observed between comagmatic samples.

## 5.3 MAGMA MIXING

Some of the magma diversity observed in the MMA may have resulted from mixing of magmas of different compositions mixing between magma reservoirs or by the addition of primitive magmas into a resevoir of relatively fractionated material.

Disequilibrium mineral textures and compositions found in a number of the MMA samples are indicative of magma mixing. Equilibrium phase compositions were calculated for each sample by using Duhem's theorem (Table 7).

The differences between calculated and observed plagioclase compositions are represented graphically in figure 33. The microphenocrysts, which are petrograhically

interpreted to form during low pressure cotectic crystallization, have core compositions that tend to be the nearest to the predicted values.

The calcic tabular glomerocrysts identified in samples 904, 893 and CASM-3, which appear to be xenocrystic due to disequilibrium textures such as resorption and mantling (figures 14, 18 and 19), have An contents 8 to 15 units greater than the predicted values.

Additional evidence for magma mixing is seen in sample P1491-1. The equilibrium plagioclase composition for this rock is calculated to be An 78. Reverse zoning is observed in an elongate microphenocryst with a core composition of An 50 surrounded by a thick An 70 mantle. Large irregular glass inclusions are present along the core-mantle boundary, as seen in the reflected light microphotograph in figure 35. The An content of the core increases gradually outward to An 54 at the core-mantle boundary where there is a sudden increase in An content to An 70. Microphenocrysts with high calcium contents (An 82) were also observed in this sample. The wide range in disequilibrium textures and compositions observed in this sample, as well as samples 883, 904 and CASM3 are most readily attributed to mixing between more and less evolved magmas. (Figure 35 is a reflected light microphotograph that was used for location with the electron microprobe.)

While variations in olivine compositions are generally smaller within any one sample (figure 34), samples 904 and 911 have large variations which are also suggestive of mixing with more evolved magmas. For example, an olivine microphenocryst was observed in sample 911 which had an Fo 82 core surrounded by a thick mantle of Fo 76 material. The equilibrium composition was calculated to be Fo 84 (figure 34).

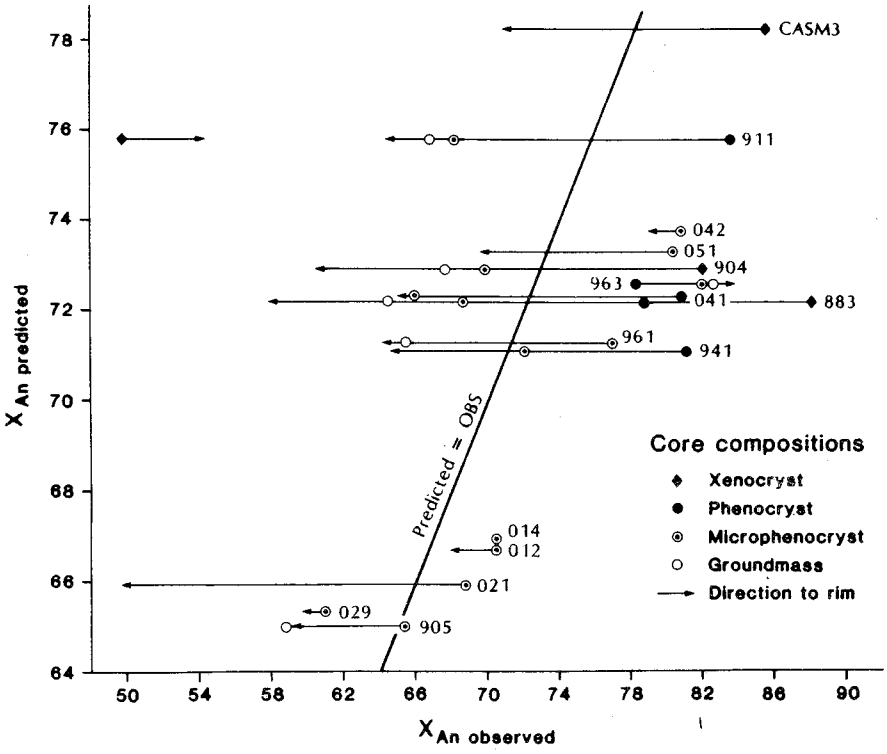


Figure 33: Observed versus calculated plagioclase compositions.

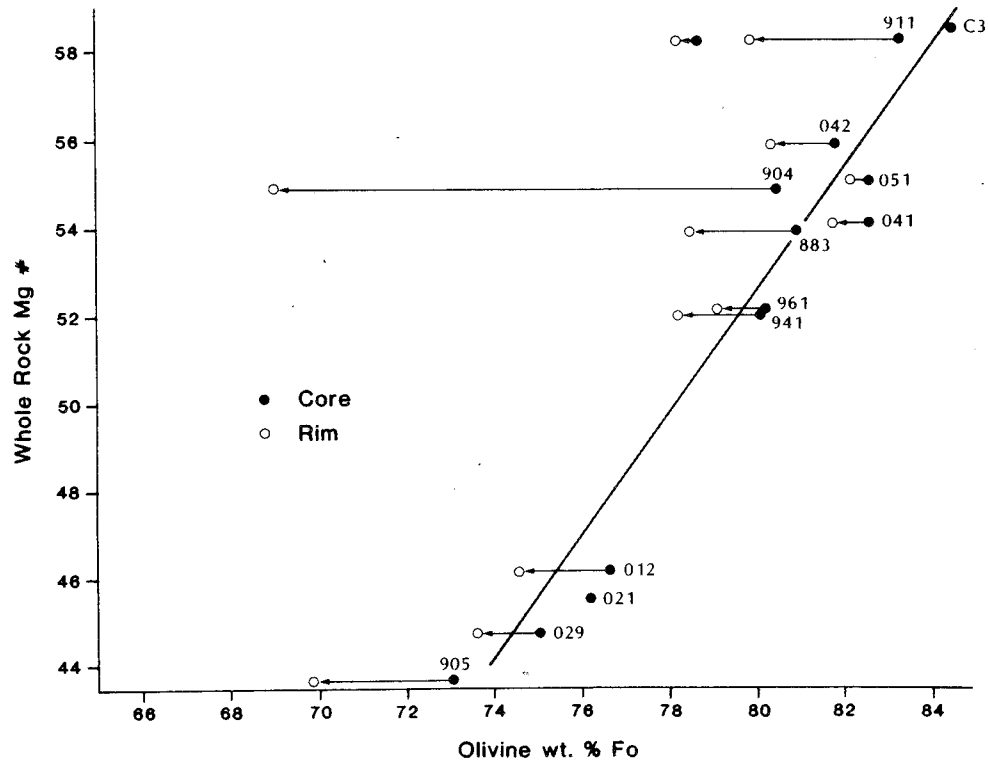


Figure 34: Observed versus predicted olivine compostitions.

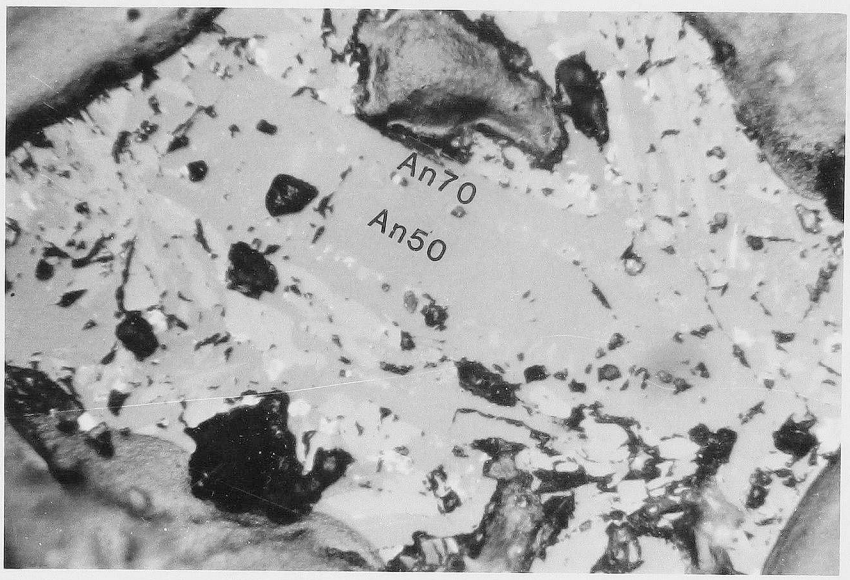


Figure 35: Sample P1491-1: plagioclase microphenocryst with An50 core and An70 mantle separated by zone of glass inclusions; evidence of magma mixing (see text).(reflected light, fov=0.5mm)

As well a in sample 911, Reverse zoning in plagioclase is also observed in only sample 963; a phenocryst with an An 78.3 core and an An 81.9 rim (figure 33). A 3.6% increase in An content could be explained by:

1. Isothermal crystallization through a pressure decrease of approximately 3 kb (Chapter 5.2).
2. The addition of a more primitive lava (with a higher equilibrium An composition) into the magma chamber.

While individual samples provide petrographical and chemical evidence of magma mixing, the samples could not be related to other samples in the suite as end member or mixed lavas. Thus, the nature and extent of mixing in the MMA could not be determined.

# 6. DISCUSSION

## 6.1 CHEMICAL EVIDENCE OF TECTONIC PROCESSES

As discussed in Chapter 2, the MMA has a complex tectonic setting. It appears from geophysical and bathymetric data (Chapter 2) to be located just 20 km to the south of a northward propagating ridge tip, and nearby over a ridge-centred hot spot. The results of the present study provide chemical evidence of both ridge propagation (FeTi basalts) and the presence of a hot spot (incompatible-element-enriched basalts) under the ridge (Chapter 4).

The coincidence of FeTi basalts with incompatible-element-enriched basalts has also been observed at the Galapagos Spreading Centre (Schilling *et al.*, 1982) and the Juan de Fuca Ridge (Delaney *et al.*, 1986). In both these cases there is also the association (on a larger scale) of a mantle plume or hot spot with active ridge propagation.

Christie and Sinton (1981) proposed that the extent of fractionation in a magma reservoir is controlled by a balance between the cooling rate and the rate at which new magma is supplied to the magma reservoir. Sinton *et al.* (1983) proposed that, as a ridge propagates into older cooler lithosphere, the magmas rising beneath the newly forming ridge axis initially undergo closed-system fractionation in small disconnected magma chambers. Larger longer lived reservoirs are not thermally stable in such a tectonic setting. The large variety of lavas sampled in the MMA more likely indicate formation in a series of discrete magma reservoirs than formation in a single well mixed magma reservoir.

Variations in ridge morphology, flow type and composition of lavas of the MMA (Chapter 4) have been sited as evidence for the presence of a hot spot just to the north of the MMA. In Francheteau and Ballard's (1983) model of axial

processes, topographic highs are proposed to be thermal expressions of principal magma chambers feeding lavas to the axis. The volume of lava erupted, proportion of sheet and lobate to pillow flows and the extent of hydrothermal activity all increase systematically approaching the topographic high.

Thompson *et al.* (1985) investigated the axial processes of a segment of the East Pacific Rise at 11°N. Their findings supported the Francheteau-Ballard model. They described five magma types sampled from the ridge on the basis of degree of fractionation and of incompatible-element-enrichment. Similar processes may be occuring on a smaller scale in the vicinity of the high-standing point on the SER, which results in a gradation in ridge morpholgy and basalt chemistry from south to north:

***northern samples:*** the less fractionated compositions, incompatible-element-enrichment and petrographical mineralogical evidence of magma mixing in some of the northern samples may reflect a locally increased degree of magma chamber size and interaction associated with the presence of a hot spot.

***southern samples:*** The highly fractionated FeTi basalts located in the south of the study area are more likely products of smaller discrete magma reservoirs that have little to no interaction. Such reservoirs are more typical of propagating ridges.

Schilling *et al.* (1982) proposed that the excess magma output rates and locally thickened crust at 91°W on the GSC could be in part attributed to higher $H_2O$ contents in the source region, which tend to slightly lower mantle viscosities and melting temperatures. This would both facilitate mantle upwelling and increase the depth range of partial melting. Michael and Chase (*in review*) have observed a strong correlation of water content and incompatible-element-enrichment in the

basalts of the MMA and the SER. Thus, water enrichment in the source region of the MMA could be facilitating the formation of a mantle plume (Morgan, 1971).

***Evidence for a Thick Crust: High Pressure Pyroxene***

One of the consequenses of increased magmatism associated with hot spot activity is an increase in crustal thickness. The crustal thickness of the SER 30 km south of the MMA is estimated from seismic profiling to be 8 to 10 km (Malecek and Clowes, 1978). It would seem reasonable that the crust at the MMA is at least this thick and probably thicker, considering isostatic compensation for the greater elevation of the ridge at this point (+300 m). Such crustal thickening probably results from increased constructive volcanism and eruption rates associated with hot spot influence.

The thermodynamic modelling of the MMA basalts determined the crystallization order of plagioclase followed by olivine and clinopyroxene to occur at pressures corresponding to depths of 4 to 6 km. Clinopyroxene is calculated to be the first formed (liquidus) phase at pressures corresponding to 8 to 10 km depth (i.e. the estimated thickness of the crust). Thus, if there is a magma reservoir at the base of an 8 to 10 km thick crust, extensive clinopyroxene fractionation could theoretically have occured in the lavas prior to shallow level fractionation and eruption at the surface.

However, clinopyroxene comprises less than 0.2% of the mode in the northern samples and in some cases is absent entirely (Chapter 3). The problem of observing chemical evidence for clinopyroxene fractionation without significant amounts of clinopyroxene present in the mode of MORBs has been referred to as the 'ghost pyroxene problem' (Rhodes and Dungan, 1979). The absence of early formed clinopyroxene phenocrysts in MORBs is usually attributed to resorption due

to isothermal depressurization during magma ascent.

A 'ghost' pyroxene may well have been preserved in sample P1505-1, however. This crystal is large (>0.5mm), sector zoned and partially resorbed with a primitive core composition (Mg# = 84.5, c.f. Table E2). All of these features distinguish it from the commonly observed later-forming anhedral skeletal crystals. This crystal is proposed to be an earlier formed high pressure xenocryst; a 'ghost pyroxene' that was not totally resorbed upon depressurization during magma ascent.

If this proposition is valid, a fractionation path for this sample, which is most consistent with the petrographical observations (i.e. corroded clinopyroxene as the only observed phenocryst phase) is indicated in figure 31.

1. Magma forms and collects at the base of a thick crust (10 to 12 km) at 4.5 kB pressure.
2. Cooling magma becomes saturated with clinopyroxene (i.e. encounters the clinopyroxene liquidus (1218°C); well formed clinopyroxene phenocrysts begin to form and settle from the melt.
3. Magma ascends. With isothermal depressurization, the path of the magma leaves the field of clinopyroxene stability and clinopyroxene crystals begin to be resorbed.
4. magma collects in a shallow high level (approximately 2kB) reservoir; plagioclase forms with cooling, eventually joined by olivine &/or clinopyroxene during subsequent cotectic crystallization.

This sequence of events would both account for the petrographic and chemical observations of the northern enriched samples in the MMA.

## 6.2 VOLCANO-TECTONIC SETTING AND HYDROTHERMAL ACTIVITY

A dynamic model was proposed by Schilling *et al.* (1982) to explain the interaction of axial hot spots and ridge propagation. In this model, the mantle-plume binary mixing model of Schilling (1973) is combined with the idea of recurring rift propagation as described by Hey (1977), whereby 'a pulsating mantle-plume flux, perhaps in the form of a chain of blobs, may initiate the development of new rifts and their propagation.' New rifts are initiated as the surplus magma reaches the surface. Propagation of the new rift occurs as this excess magma flows away from the locus of the plume through older cooler crust. The extent and rate of propagation reflect the size and frequency of the plume flux.

This model can be used to explain the volcano-tectonic evolution of the MMA. In Chapter 2, it was proposed that the Seminole Seamount and Scott Seamounts were formed on the ridge axis at or near the MMA as the products of a hot spot. The variation in the extent of volcanic construction of these features along their length, particularly in the Seminole Seamount, may be due to regular variations in the amount of magma supplied to the axis from a mantle plume. Less enriched samples dredged from directly west of the MMA (Cousens, 1982) may thus have been formed during a period when there was a smaller proportion of hot spot-enriched magma supplied to the ridge axis.

Spatial and temporal variations in mantle upwelling (Crane, 1985) and magma supply would produce variations in the crustal heat flux, which in turn would in part determine the location and duration of hydrothermal activity on the ridge axis through time (Crane, 1984 and Crane *et al.*, 1980).

It is assumed that an increased volume and frequency of magma pulses would result in an increase in the size and duration of magma reservoirs. If this is so, there would be an increased probability of interaction (mixing) of new pulses of

primary material in magma reservoirs as well as mixing of materials between reservoirs. However, variations in incompatible-element-enrichment of the lavas in the area indicate that homogeneous magma reservoirs are unlikely to be more than 1 km wide. Another possibility is that a larger reservoir is present that is chemically zoned because of a lack of convection in the chamber. It is impossible, however, to distinguish geochemically such reservoirs from smaller homogeneous reservoirs.

## 6.3 CONCLUSIONS

The major conclusions of the present study are here summarized:

1. The lavas of the Magic Mountain area are Recent, aphyric to moderately phyric (0 to 6 % crystals) pillow, lobate and sheet flows.
2. The petrographically inferred crystallization order for these basalts is plagioclase followed by olivine and clinopyroxene. Pressures of 1.5 to 2 kb (obtained from thermodynamic calculations) predict this crystallization order as well as the observed modal phase proportions. Thus the magma reservoirs in which the crystals formed was probably at 4 to 6 km depth (1 to 2 kb).
3. A magnesium rich clinopyroxene xenocryst occuring in one of the northern samples was probably formed at pressures corresponding to 8 to 10 km depth (assuming that it was not formed in the mantle). This finding serves to corroborate the geophysical evidence of a thick crust beneath the MMA.
4. From element-ratio diagrams and mass-balance calculations it was demonstrated that the 25 samples are from at least 10 distinct magmas. This diversity precludes the possibility that the MMA samples are derived from a common magma reservoir or a single magma source.
5. Plagioclase glomerocrysts and chemically zoned plagioclase and olivine microphenocrysts occuring in some of the northern samples reflect the presence of magma reservoirs between which some degree of mixing may

have occured.

6. The sample suite also includes the most iron-titanium (FeTi) enriched basalts sampled to date in the Explorer Region. These enrichments provide chemical evidence supporting the geophysical evidence that the SER is an actively propagating ridge segment.

7. The fact that all the FeTi basalts were sampled in the southern half of the study area is consistant with other lines of evidence that magma reservoirs are small and isololated in the south and larger and more interconnected in the north.

8. Changes in ridge thickness and height, abundance of sheet flows and degree of hydrothermal activity indicates an increased magma supply from south to north in the MMA.

9. The most incompatible-element-enriched samples collected to date from the Explorer Region are from the MMA. Furthermore, the increase in incompatible element enrichment from south to north in the MMA suggests that the increased magma supply is due to the presence of an axial hot spot 5 km to the north.

10. The Seminole and Scott Island seamounts are proposed to have been formed at the site of the hot spot north of the MMA. Variations in the size of the seamounts, the extent and rate of rift propagation and hydrothermal activity could result from cycles in the mantle plume flux.

## 6.4 SUGGESTIONS FOR FURTHER STUDY

The relationship between hot spot activity and increased magmatism with the location and duration of axial hydrothermal activity has not been actively investigated to date. However, correlations of enrichment in incompatible elements, magmatism and hydrothermal activity with ridge elevation have been observed at many spreading centres (Ballard and Francheteau, 1983, Bougault *et al., in press,* Schilling *et al.,* 1982). Thus, there are two suggestions for further study:

1. Obtain and analyse more samples from the flanks of the SER and from the nearby volcanic features to increase our understanding of the interplay of ridge jumps and propagation with hot spot activity occuring over the last few million years in the Explorer Region.
2. In so doing, seek to better define the relationship of ridge propagation with the spatial and temporal variations in extensive axial hydrothermal activity and associated massive sulphide deposition.
3. Obtain more well located samples, either with PISCES 4 or a remotely operated vehicle (ROV) in and near the study area to better delineate
   a. the size, location and duration of magma reservoirs.
   b. the variation in these parameters at and away from the axial high.
   c. location and extent of plume type magmas.
   d. location and extent of interaction (mixing) of more and less enriched magmas and more and less fractionated magmas.

## APPENDIX A: MODAL ESTIMATES

*i) Point Counting Method*

Polished rectangular (25mm by 40mm) thin sections were prepared for each of the 25 samples. The points were counted at a 0.5mm spacing. The mode was calculated after the first 1000 points were counted. After each additional 100, the mode was recalculated until the relative variation between subsequent modal estimates was less than 5% for each phase. The number of points counted on a given slide varied from 1100 to 3000 points in order to obtain a 5% precision.

Plagioclase which appeared to be xenocrysts were counted separately. These tended to be large grains (>0.5mm) with large, often rounded cores. The rims often showed reaction relation and resorption and had cores rich in glass inclusions.

*ii) Accuracy*

The accuracy of determining the mode of the sample is subject to the following factors:

1. An increase in the degree of crystallization of the groundmass from rim to interior of the sample leads to a greater likelihood of an overestimation of the microphenocryst mode in the holocrystalline interiors where a size continuum is often observed between microlites and microphenocrysts (see text Ch. 3). The size and shape criteria for identifying microphenocrysts, phenocrysts and microlites are presented in table A1.

2. Preferred orientations of non-symmetrical mineral grains would result in different modal estimates of the same rock by counting sections made through different planes. Although the cpx and plag crystals are elongated, they appear to be randomly orientated in all of the samples and thus the assumption that the volume % of a phase is equal to the area % in the slide is probably still valid.

3. Phase misidentification occurs, usually between small olivine and cpx microphenocrysts. This may affect the modes of the highly crystalized samples but is generally not very significant.

**Table A1: Criteria for Establishing Crystal Type**

| Phase | Crystal Shape | Crystal Size (mm) | Crystal Type |
|---|---|---|---|
| plagioclase | skeletal | <0.1mm | microlite |
| | tabular | <0.08 | microlite |
| | skeletal | 0.1 to 0.5 | microphenocryst |
| | tabular | 0.08 to 0.25 | microphenocryst |
| | skeletal | >0.5 | phenocryst |
| | tabular | >0.25 | phenocryst |
| | tabular | >2.0 | megacryst |
| clinopyroxene | anhedral | <0.1 | microlite |
| | euhedral | <0.05 | microlite |
| | euhedral | 0.05 to 0.5 | microphenocryst |
| | anhedral | 0.1 to 0.5 | microphenocryst |
| olivine | skeletal | <0.1 | microlite |
| | euhedral | <0.05 | microlite |

## APPENDIX B: SAMPLE PREPARATION

### i) Preparation of Sample Powders

Approximately 10g of fresh rock powder for each of the 25 samples was prepared. These powders were used to make fused disks and pressed powder pellets for major and trace element XRF analysis, respectively. Sources of contamination were of primary concern in developing a careful method of preparation which is outlined below:

1. Fresh portions of each sample are selected and broken down to 1 cm pieces with a hydraulic wedge vice in order to thoroughly check for and eliminate hydrothermal precipitates and alteration materials on surfaces and in fractures and vessicles in the interiors.

2. The fresh pieces are then reduced to small pea size fragments by hammering them in a plastic bag and then removing any small bits of plastic adhering to the fragments. The plastic is composed mostly of C, H and O, elements which do not interfere in XRF analyses. On the other hand, the jaw crushers and ring wheels normally used to do this job contain significant contents of interfering trace elements.

3. The grains are then placed in a ring crusher which is run until the material is reduced to 200 mesh. This usually takes 50 to 60 seconds for basalts. (Running the machine for much longer risks the oxidation of the iron in the powder.) The tungsten-carbide mill was used rather than the Cr-steel mill in order to avoid contamination by Cr and Ni (Hickson and Juras, 1986).

   Nb contamination due to grinding with the W-C mill was demonstrated by P. J. Michael (Pers. Comm.). Eight basalt samples were prepared using both the W-C mill and an agate mortar and pestle. The Nb concentrations in the samples ground in the W-C mill were 0.50 ± 0.64 ppm higher than those prepared with the agate mortar and pestle. This difference is comparable to the analytical uncertainty for Nb. Thus the difference is significant and the Nb values were lowered by 0.5 ppm.

4. Each powder was poured into a clean plastic sample bottle. After each run, the ring crusher was thoroughly washed and dried out with kim-wipes and the area thoroughly cleaned in order to avoid cross contamination between samples.

### ii) Preparation of Fused Glass Disks

1. The sample powders, flux and platinum crucibles were dried at 100°C for 3 hours to drive off any water adsorbed from the atmosphere.

2. After cooling to ambient temperature, 400.00±0.2mg of sample powder + 3600.00±0.2mg of Spectroflux®105 were measured into a clean dry platinum crucible. The composition of this flux material is: 47.0% dilithium tetraborate, 36.7% lithium carbonate and 16.3% lanthanum oxide. The heavy lanthanum oxide absorbs emmisions of scattered X-rays. The amounts of the powders must be carefully measured because the major element reduction programs are based on a 1:9 ratio of sample to flux. The weighing precision was ±0.2mg.

3. The crucibles were heated in a furnace at 1100°C for 30 minutes, and then cooled in a descicator for 20 minutes.

4. The crucibles were re-weighed. The weight loss is attributed to loss of volatiles during fusion of the powder in the oven. The difference is made up by the addition of Spectroflux®100, composed of pure lithium tetraborate, which does not absorb secondary electrons and thus will not affect the 1:9 sample to flux ratio.

5. The crucibles were heated over a burner until the glass was completely remelted. At this point, the liquid was poured quickly into an aluminum disk mold and cooled slowly on a 300°C hot plate.

6. After cooling for about 20 minutes, the disks are labelled (on the side not exposed to x-rays during the analysis) and placed into separate labelled bags.

It is of paramount importance to keep the samples well separated and identified at every step of sample preparation and analysis.

iii) Preparation of Pressed Powder Pellets

Approximately 4 grams of powder are mixed with 2 to 3 drops of a 2% water solution of poly-vinyl alcohol (pva) which acts as a binder. The pellet and its boric acid backing are compressed at a pressure of 20 tonnes per square inch for about one minute. The resulting pellet is labelled on the back and placed into a separate plastic sample bag. The pellet-making apparatus is thoroughly cleaned between the preparations of each sample.

## APPENDIX C: WHOLE-ROCK MAJOR-ELEMENT ANALYSIS

*i) Analytical Procedure*

The oxide concentrations of ten major elements were determined: silicon ($SiO_2$), titanium ($TiO_2$), aluminum ($Al_2O_3$), iron ($Fe_2O_3$), manganese (MnO), magnesium (MgO), calcium (CaO), sodium ($Na_2O$), potassium ($K_2O$) and phosphorous ($P_2O_5$).

Initially, the P1400 samples and P1500 samples were analysed on separate runs. Four P1500 samples were included in both runs for an estimate of inter-run precision. The analyses of Ti, Mn and P were quite consistent between runs for these samples. However, for the elements Si, Al, Fe, Mg, Ca, Na and K, variations of analyses betweeen runs were large and unsystematic, possibly caused by instrumental drift between runs and/or poor sample preparation. Consequently, all 25 samples were prepared for a single re-calibrated and drift-monitored run analysing the seven elements that exhibited significant inter-run variations. Poorly formed disks were recast and those yielding analyses with total oxide contents greater than 101.5% or less than 98% were made again from the original rock powders.

*ii) Calibration and Data Reduction*

Calibrations for each element were made with the twelve well-defined igneous rock standards listed in table C1 using the recommended concentration values of Abbey (1983). The calibrations were regressed and unknown concentrations calculated using the on-line program supplied by Phillips for the PW1400 XRF machine. Total volatile contents of the standards ranged from 0.24 to 3.31 wt.%. The program converts recommended standard values into the volatile free amounts, which are be the effective concentrations after fusion.

The counting times were doubled from those of the previous runs to minimize the counting statistical errors. The standard BHVO and the sample P1490-5 were analysed repeatedly through the run in order to estimate the precision of the data. Details on calibrations, as well as data precision are provided in Appendix D.

**Table C1: Standards for Major Element Analysis**

| Standard | Rock Type | Source |
|---|---|---|
| AGV-1 | Andesite | USGS |
| BHVO-1 | Basalt | USGS |
| BR | Basalt | USGS |
| DR-N | Basalt | ANRT, France |
| G2 | Granite | USGS |
| GA | Granite | CRPG, France |
| GSP-1 | Granodiorite | USGS |
| MRG-1 | Gabbro | CCRMP, Canada |
| NIM-G | Granite | NIM, S.Africa |
| NIM-S | Syenite | NIM, S.Africa |
| SY-2 | Syenite | CCRMP, Canada |

*iii) Instrument Precision*

The major element instrument precision was estimated by calculating the 1 $\sigma$ deviation of six replicate analyses of the basaltic standard BHVO. The values for each element are listed in table C2 as the instrument precision error '$e_i$'. The $e_i$ value is a relative error, expressed as a percentage of the analysis value. The detection limits were calculated using the formulae derived by C. J. Hickson (PhD thesis, 1986). The values for $e_i$ are listed along with the detection limits in table C2. The detection limits are those calculated from standard BHVO.

**Table C2: Major Element Analysis Statistics**

| Element | Range in Comp.(wt%) | Det.Lim.(wt%) | $e_i$ [2] (%) |
|---|---|---|---|
| $SiO_2$ | 49.52 to 50.88 | 0.73 | 0.45 |
| $TiO_2$ | 1.30 to 2.35 | 0.01 | 0.49 |
| $Al_2O_3$ | 13.87 to 16.14 | 0.24 | 0.88 |
| FeO* | 8.72 to 12.38 | 0.13 | 0.15 |
| MnO | 0.15 to 0.23 | 0.01 | 4.40 |
| MgO | 5.44 to 7.66 | 0.12 | 2.40 |
| CaO | 9.92 to 12.22 | 0.13 | 0.40 |
| $Na_2O$ | 2.32 to 3.29 | 0.24 | 1.48 |
| $K_2O$ | 0.40 to 0.75 | 0.04 | 1.77 |
| $P_2O_5$ | 0.18 to 0.35 | 0.02 | 2.80 |

[1] detection limit on sample BHVO-1.

[2] instrumental precision error, calculated as $1\sigma$ of 6 duplicate analyses of standard BHVO-1 (see text).

## APPENDIX D: WHOLE-ROCK TRACE ELEMENT ANALYSIS

*i) Analytical Procedure*

The concentrations of 10 trace elements were determined: barium (Ba), chromium (Cr), copper (Cu), niobium (Nb), nickel (Ni), rubidium (Rb), strontium (Sr), vanadium (V), yttrium (Y) and zirconium (Zr). Measurements were made on pressed powder pellets using the Department of Oceanography's Phillips PW1400 x-ray flourescence unit with a rhodium x-ray tube.

The samples were analysed during two separately calibrated runs. The P1400 series (SCHISM) samples were included at the end of a large group of 79 samples analysed during one long run from July 25 to July 30, 1985 (80 minutes/sample). The P1500 series (CASM4) samples were interspersed in a later drift monitored run of 37 samples analysed from Oct. 17 to Oct. 20, 1985. Determinations of precision between runs were made from four P1500 series samples analysed on both runs. The CASM3 sample was analysed separately.

*ii) Calibrations and Data Reduction*

Calibrations were made at the beginning of both runs for each of the ten elements analysed. Twelve well-defined igneous rock standards were used, representing most of the compositional spectrum from ultra-mafic peridotites to granites. Standard working curves and unknown concentrations were calculated using the regression program of Dr. R. L. Armstrong modified by C. J. Hickson, both of the Department of Geological Sciences at the University of British Columbia. The modified program also calculates and lists the counting statistical errors and detection limits of each standard in the 10 calibrations.

The purpose of this appendix is to specify the standards used in calibrating the XRF unit, their recommended values and the inter-element interference factors

employed in obtaining the best fit for the final regression curves in the range of the unknown concentrations. The precision of the data will also be discussed. These details are specified for those interested in using this data for any careful work in which precision and accuracy need be known with a high degree of confidence.

The 12 standards, along with the recommended value sets used for each are listed in table D1. All of this information was obtained from the summary by Govindaraju (1984).

**Table D1: Standards for Trace Element Calibrations**

| Standard | Rock Type | Source | Analysis Used |
|---|---|---|---|
| AGV-1 | Andesite | USGS | Gladney '83 |
| BCR-1 | Basalt | USGS | Gladney '83 |
| BE-N | Basalt | ANRT, France | Govindaraju '80 |
| BHVO-1 | Basalt | USGS | Abbey '83 |
| G2 | Granite | USGS | Gladney '83 |
| GA | Granite | CRPG, France | Govindaraju '77 |
| GSP-1 | Granodiorite | USGS | Gladney '83 |
| JB-1 | Basalt | GSJ, Japan | Andrews '84 |
| MRG-1 | Gabbro | CCRMP, Canada | Abbey '83 |
| NIM-N | Norite | NIM, S.Africa | Malakoff '77 |
| PCC-1 | Peridotite | USGS | Gladney '83 |
| W-1 | Diabase | USGS | Gladney '83 |

The following priority of considerations was made in obtaining the best fits:

1. Optimizing fit for standard values in range of unknown concentrations (i.e. basalt standards).

2. Obtaining a high degree of correlation ($R>0.995$) between counts measured and standard concentration values and minimizing the standard deviation.

3. Passing the Y intercept as close as possible through zero for elements with unknown concentrations less than 50 ppm.

The first way of obtaining these ends is in 'rejecting' standards from the regression.

All standards yielding negative net counts were automatically excluded by the trace element reduction program. Standards were often excluded that had concentrations several times greater than those of the unknowns; for example Ba in the granite standards, and Cr and Ni in the peridotite standard. Occasionally non-basaltic standards were excluded from the regression to improve the fit of the curve in the concentration range of the unknown samples and in order to improve the accuracy of the results.

*iii) Inter-element Interferences*

The second way of refining the regressions was by correcting for inter-element interferences. The interferences from Ti $K_\alpha$ on Ba $L_\alpha$, and Ti $K_\beta$ on the V $K_\alpha$ and Cr $K_\alpha$ peaks were calibrated by preparing five pellets from a single sample powder of a low Ti basalt. Different increments of reagent-grade $TiO_2$ were added to each pellet such that the resulting suite of pellets spanned the range of $TiO_2$ concentrations observed in the unknowns. The interferences calibrated are:

1. Ti $K_\beta$ (2.514 Å) on V $K_\alpha$ (2.505 Å), Ti MAC = 270
2. Ti $K_\alpha$ (2.750 Å on Ba $L_\alpha$ (2.776 Å), Ti MAC = 115
3. Ti $K_\beta$ (2.514 Å) on Cr $K_\alpha$ (2.229 Å), Ti MAC = 570

where MAC is the mass absorption coefficient (wavelength and MAC data from Jenkins and De Vries, 1967). The effects of increasing Ti concentration on the Ba, V and Cr peaks are listed in table D2.

Each interference correction factor was obtained by dividing the change in the net counts of the element interfered with (e.g., Ba), by the change in the net counts of Ti between the original and $TiO_2$ supplemented sample. The results of the calibration are presented in table D2.

**Table D2: Calibration of Ti Interference**

| mg $TiO_2$[1] | wt% $TiO_2$ | $I_N$ Ti[2] | $I_N$ V $K_\alpha$ | cf: Ti-V[3] | $I_N$ Ba $L_\alpha$ | cf: Ti-Ba | $I_N$ Cr $K_\alpha$ |
|---|---|---|---|---|---|---|---|
| 0.00 | 1.03% | 6315 | 1375 | | 10 | | 1723 |
| 20.17 | 1.53% | 10930 | 1827 | 9.83% | 15 | 0.109% | 1723 |
| 40.48 | 2.02% | 15258 | 2230 | 9.66% | 21 | 0.124% | 1738 |
| 80.94 | 3.00% | 23890 | 3021 | 9.56% | 31 | 0.122% | 1717 |
| 121.54 | 4.07% | 32867 | 3848 | 9.59% | 45 | 0.135% | 1679 |

[1]mass of $TiO_2$ added to 4,000 mg of basalt, each measurement ± 0.04 mg
[2]net counts Ti; at λ=2.514 Å for V and λ=2.750 Å for Ba, see text.
[3]correction factor: % of Ti net counts to be subtracted from analyte net counts. This factor has also been adjusted for the effective dilution of original sample by addition of Ti powder.

Although the correction factor for Ti $K_a$ on Ba $L_a$ is small, the effective correction is large, because the number of counts from Ti is large and from Ba is small. For instance, in one sample, 0.12% of 15258 Ti counts is 18 counts of interference on the Ba peak, whereas only 21 Ba counts were measured in total. Thus, only 3 counts, or 14% of the measured counts at the Ba $L_a$ wavelength in that sample would be from Ba $L_a$ emissions. Similarly, the Ti interference on V $K_a$ represents 1465/2230 or 66% of the measured total net counts. The effective Ti interference on Cr $K_a$ was found to be less than 1% and was deemed to be insignificant.

The Ti correction factors are fairly constant across the measured range of Ti concentrations. The interpolated correction factors for 1.8 wt% $TiO_2$, an average concentration for the standards and unknowns, were used in the trace element reduction program.

There is an apparent 'negative' interference of Ti on Cr. Net counts from Cr decrease by 2.6% with an increase of 3 wt% $TiO_2$. This may be attributed to the large amount of mass absorption by Ti of electrons at the Cr $K_a$ wavelength, where the Ti MAC is 565. With an increase of $TiO_2$ wt% from 0.8 to 3.8%, the bulk MAC. for Cr $K_a$ increases from 15.95 to 16.35. This increase of 2.5% accounts for most of the observed 2.6% decrease in Cr counts.

The calibrated Ti interference factors were applied to both runs. The smaller yet still significant interferences of Rb $K_a$ on Y $K_a$ and Ni $K_a$, and of V $K_a$ on Cr $K_a$ were not calibrated for either run. They were determined indirectly by an iterative process, whereby the calibration for a given element is regressed repeatedly, each time with a different interference factor. The factor chosen is the one that minimizes the differences between published and calculated values for the standards both relatively enriched and depleted in the interfering element. The values thus

obtained are close to values measured for this instrument previously. The interference factors used for each are presented in table D3, along with the typical amount of the interference which is being corrected for. The correction factor for the interference of Sr $K_a$ on Zr $K_a$ was 13.9%. This factor was obtained previously.

**Table D3: Trace Element Interference Factors**

| Interference | Factor Run 1 | Int. Amount[1] | Factor Run 2 | Int. Amount |
|---|---|---|---|---|
| Ti $K_\beta$ → Ba $L_a$ | 0.065% | 29% | 0.125% | 31% |
| Ti $K_a$ → V $K_a$ | 7.24% | 34% | 10.0% | 36% |
| V $K_a$ → Cr $K_a$ | 16% | 53% | 16% | 51% |
| Rb $K_a$ → Ni $K_a$ | 2.9% | 0.5% | 2.9% | 0.5% |
| Rb $K_a$ → Y $K_a$ | 26.9% | 3.2% | 24.8% | 2.7% |
| Sr $K_a$ → Zr $K_a$ | 13.9% | 13.9% | 13.9% | 13.9% |

[1] Proportion of net counts contributed by interfering element

These correction factors are applied as a proportion of the 'raw' net counts (i.e. counts before the mass-absorption correction) of the interfering element to be subtracted from the raw net counts of the element interfered with. For example, 16% of the raw net counts of V, as the interfering element, are subtracted from the raw net of counts of Cr. The Ti interference factors for the second run obtained by this indirect method are close to those directly measured and listed in

table D2. The size of the corrections for each element are similar on each run as well. Both of these facts indicate that the iterative method of obtaining correction factors is valid. The calibrations and interference corrections for sample CASM3 are not available to the author.

*iv) Precision Within a Run*

During the second run, the instumental precision was estimated. This was done by analysing the standard BHVO, which has a composition similar to the unknown samples, every fifth sample throughout the run, six times in all. The instrumental precision error for an element ($e_i$) is the one standard deviation value of the 6 measurements made of that element expressed as a percentage. These measurements are presented in table D4. The one standard deviation variation of standards in the calibration regression $e_c$ is reported along with the correlation coefficients of the regressions. The detection limits were calculated using equations derived by C. J. Hickson (PhD thesis, 1986). These values are also included in table D4. The values listed in the table are those calculated for sample P1490-7. The detection limit for an element varied little between the samples.

*v) Differences Between Runs*

The four samples P1502-1, P1504-1, P1502-9 and P1496-1 were included in both runs to estimate differences between runs. These observations are presented in table D4. A difference was determined to be significant when the average difference of the analyses of the four samples between runs ($=X_\Delta$) was greater than the uncertainty of the calibration ($e_c$). (The $X_\Delta$ values are included in table D4). Thus significant differences between runs were observed for Cr, Ni, Nb, Rb and Zr.

**Table D4: Trace Element Analysis Statistics**

| Element | Range in Comp.(ppm) | Det.Lim.[1] | $e_i$[2] | $e_c$[3] | R[4] | $X_\Delta$[5] |
|---|---|---|---|---|---|---|
| Ba | 72 to 158 | 2.5 | 3.3 | 14.3 | 0.99981 | -5.0 ±11.9 |
| Cr | 38 to 272 | 2.0 | 1.3 | 15.5 | 0.99688 | -32.0 ±12.6 |
| Cu | 42 to 81 | 2.7 | 8.3 | 8.2 | 0.98909 | -5.1 ±10.8 |
| Nb | 13.7 to 24.5 | 0.5 | 0.13 | 1.3 | 0.99760 | 1.5 ±0.4 |
| Ni | 36 to 90 | 2.3 | 5.2 | 5.1 | 0.99741 | -3.4 ±3.0 |
| Rb | 6.0 to 11.2 | 2.1 | 0.36 | 0.72 | 0.99997 | 1.5 ±0.5 |
| Sr | 164 to 202 | 2.4 | 5.2 | 6.6 | 0.99914 | 4.9 ±4.9 |
| V | 305 to 443 | 1.1 | 8.1 | 26.1 | 0.98314 | 14.5 ±6.8 |
| Y | 25 to 43 | 2.3 | 1.0 | 1.4 | 0.98905 | 0.2 ±1.2 |
| Zr | 98 to 188 | 3.0 | 2.1 | 7.0 | 0.99893 | 8.0 ±1.0 |

[1] detection limit on sample P1490-7, calculated using equations in text.
[2] instrument precision error, calculated as $1\sigma$ of 6 duplicate analyses of standard BHVO (see text).
[3] one $\sigma$ uncertainty on the calibration regression.
[4] correlation co-efficient of the calibration regression.
[5] average difference observed between runs on four duplicates (see text).

The Rb values in the second run are higher on average by 13.6% (approx. 1.5 ppm) than those in the first run. However, samples from both runs were analysed by isotope dilution (P. J. Michael, *in prep.*). It was determined that the samples in the first run were consistently 4% higher and those in the second were 14% higher than the isotope dilution (ID) values. This 10% difference is close to the 13.6% observed directly between runs. To increase the accuracy of the results, the values of the first run were decreased by 4% and those of the second by 14%. The vanadium values were compared in a similar manner to instrumental neutron activation (INAA) measurements. Values from the first run were decreased by 3.4% (approx. 12 ppm) and values from the second run were increased by 2.5%. There were no measurements of Nb, Cr or Zr made by other methods. For these elements, the analyses from each run were corrected 'toward' each other by half of the $X_{\Delta}$ value. For instance $X_{\Delta}$ is 8 ppm for Zr, thus the first run values were raised by 4 ppm and the second run values were lowered by 4 ppm.

## APPENDIX E: ELECTRON MICROPROBE ANALYSIS AND RESULTS

The mineral phases of eleven of the 25 samples were analysed by electron microprobe. The P1400 series samples were analysed at UBC with the automated three channel ARL-SEMQ microprobe. Seven P1500 series samples and the CASM-3 sample were analysed at the Smithsonian Institute (SI) in Washington, D.C. by Dr. P. J. Michael using an automated 9-channel ARL-SEMQ microprobe. The acceleration voltage was set at 15 kV for both instruments. The beam current was 30 nA (SI) and 40 nA (UBC). The beam diameter used in analysis was approximately 1 $\mu$m.

Calibrations were made using both natural and synthetic mineral standards and the raw data was reduced using the method of Bence and Albee (1968). Plagioclase and clinopyroxene ternary diagrams for individual samples are presented in figures E1 and E2, respectively.

The mineral analyses are listed in table E1 (plagioclase), E2 (clinopyroxene) and E3 (olivine). The analyses in these tables are labelled in such a way as to convey both the number of the sample and the type (size) of crystal analysed. The following is an example:

883-MC2

1. The first three numbers in the label are the last three digits of the sample number.
2. The first letter after the hyphon denotes size of the grain analysed: P = phenocryst, M = microphenocryst, G = groundmass microlite.
3. The second letter after the hyphon denotes the location of the analysis within the grain: C = core, M = mantle, R = rim.
4. The final number (if needed) distinguishes between anlyses of the same sample that are on the same grain size and location.

Thus, the example sample label refers to the analysis of a second microphenocryst core from sample P1488-3.

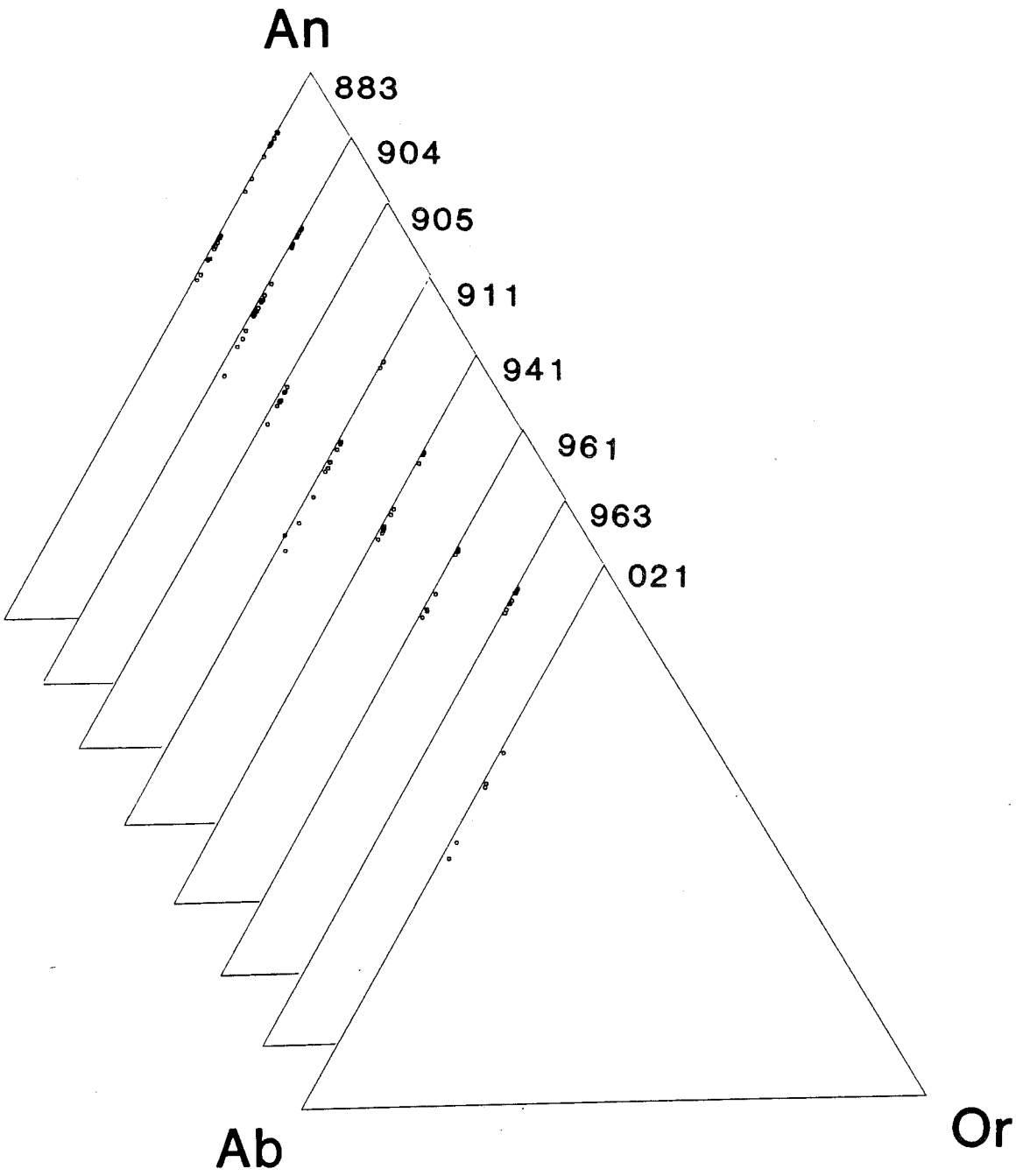


Figure E1: Plagioclase ternary diagrams for individual samples.

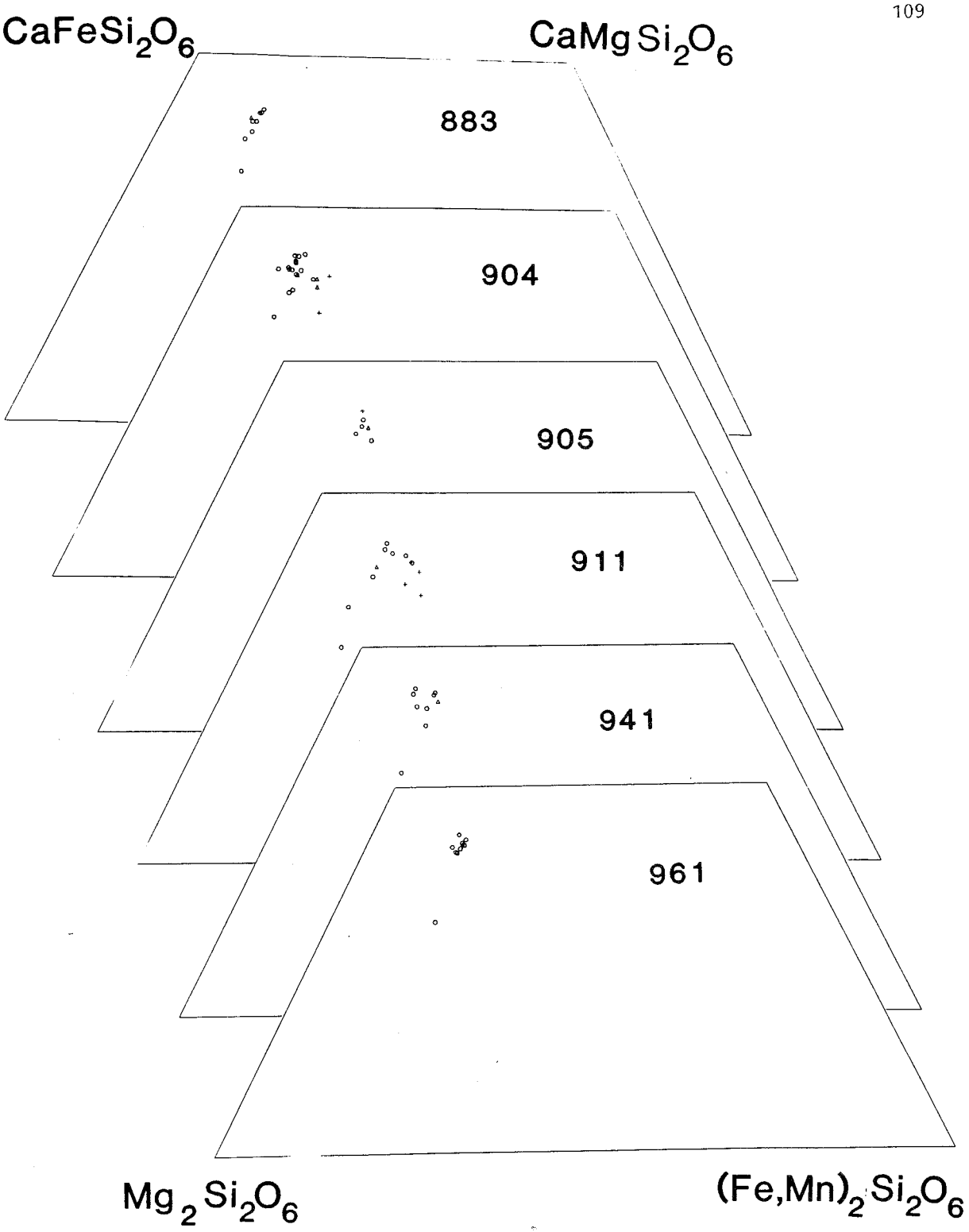


Figure E2: Clinopyroxene ternary diagrams for individual samples.

**Table D2: Calibration of Ti Interference**

| mg $TiO_2$ [1] | wt% $TiO_2$ | $I_N$ Ti [2] | $I_N$ V $K_\alpha$ | cf: Ti-V [3] | $I_N$ Ba $L_\alpha$ | cf: Ti-Ba | $I_N$ Cr $K_\alpha$ |
|---|---|---|---|---|---|---|---|
| 0.00 | 1.03% | 6315 | 1375 | | 10 | | 1723 |
| 20.17 | 1.53% | 10930 | 1827 | 9.83% | 15 | 0.109% | 1723 |
| 40.48 | 2.02% | 15258 | 2230 | 9.66% | 21 | 0.124% | 1738 |
| 80.94 | 3.00% | 23890 | 3021 | 9.56% | 31 | 0.122% | 1717 |
| | | 32867 | 3848 | 9.59% | 45 | 0.135% | 1679 |

[1] mass of
[2] net counts
[3] correction fac...
adjusted for the e...

...t, each measurement ± 0.04 mg
...750 Å for Ba, see text.
...tracted from analyte net counts. This factor has also been
...le by addition of Ti powder.

Table E1: Plagioclase Electron-Microprobe Analyses from MMA Basalts

| Sample: | 883-PC | 883-PM | 883-G | 883-MC | 883-MR | 883-MM | 904-PC | 904-PM | 904-PR | 904-MC |
|---|---|---|---|---|---|---|---|---|---|---|
| Anal.#: | 1 | 2 | 3 | 4 | 5 | 6 | 7 | 8 | 9 | 10 |
| | wt.% | wt.% | wt.% | wt.% | wt.% | wt.% | wt.% | wt.% | wt.% | wt.% |
| SiO2 | 45.66 | 46.07 | 50.62 | 50.97 | 52.58 | 51.61 | 47.86 | 50.26 | 52.45 | 50.76 |
| Al203 | 35.15 | 33.43 | 29.20 | 30.76 | 27.10 | 29.73 | 33.21 | 30.96 | 29.10 | 30.29 |
| FeO* | 0.45 | 0.45 | 0.66 | 0.64 | 0.97 | 0.74 | 0.63 | 0.66 | 1.03 | 0.73 |
| MgO | 0.14 | 0.12 | 0.21 | 0.22 | 0.60 | 0.24 | 0.17 | 0.24 | 0.24 | 0.22 |
| CaO | 18.26 | 17.66 | 13.56 | 14.45 | 12.93 | 14.05 | 17.16 | 14.99 | 13.23 | 14.40 |
| Na20 | 1.25 | 1.53 | 3.90 | 3.44 | 4.14 | 3.59 | 1.90 | 3.00 | 3.94 | 3.38 |
| K20 | 0.04 | 0.03 | 0.09 | 0.08 | 0.12 | 0.09 | 0.05 | 0.09 | 0.12 | 0.10 |
| TOTAL | 100.95 | 99.29 | 98.24 | 100.56 | 98.44 | 100.05 | 100.98 | 100.20 | 100.11 | 99.88 |
| | IRON CALCULATED AS Fe203 (TOTAL) | | | | | | | | | |
| Si | 2.0869 | 2.1377 | 2.3494 | 2.3126 | 2.4297 | 2.3505 | 2.1787 | 2.2915 | 2.3832 | 2.3194 |
| Al | 1.8934 | 1.8282 | 1.5972 | 1.6449 | 1.4759 | 1.5958 | 1.7818 | 1.6636 | 1.5584 | 1.6312 |
| Fe+3 | 0.0172 | 0.0175 | 0.0256 | 0.0243 | 0.0375 | 0.0282 | 0.0240 | 0.0252 | 0.0391 | 0.0279 |
| Mg | 0.0095 | 0.0083 | 0.0145 | 0.0149 | 0.0413 | 0.0163 | 0.0115 | 0.0163 | 0.0163 | 0.0150 |
| Ca | 0.8942 | 0.8780 | 0.6743 | 0.7025 | 0.6402 | 0.6856 | 0.8370 | 0.7323 | 0.6441 | 0.7050 |
| Na | 0.1108 | 0.1377 | 0.3509 | 0.3026 | 0.3709 | 0.3170 | 0.1677 | 0.2652 | 0.3471 | 0.2994 |
| K | 0.0023 | 0.0018 | 0.0053 | 0.0046 | 0.0071 | 0.0052 | 0.0029 | 0.0052 | 0.0070 | 0.0058 |
| SUM | 5.0143 | 5.0091 | 5.0173 | 5.0064 | 5.0026 | 4.9986 | 5.0037 | 4.9993 | 4.9951 | 5.0037 |
| TETRA | 3.9975 | 3.9834 | 3.9722 | 3.9818 | 3.9431 | 3.9745 | 3.9845 | 3.9803 | 3.9807 | 3.9785 |
| X-CAT | 1.0168 | 1.0257 | 1.0451 | 1.0246 | 1.0595 | 1.0241 | 1.0191 | 1 0190 | 1.0144 | 1.0252 |
| | COMPOSITION (MOLE %) | | | | | | | | | |
| AN | 87.94 | 85.60 | 64.52 | 68.56 | 60.42 | 66.94 | 82.13 | 71.86 | 63.49 | 68.76 |
| AB | 10.89 | 13.42 | 33.58 | 29.54 | 35.01 | 30.95 | 16.46 | 26.03 | 34.22 | 29.21 |
| OR | 0.23 | 0.17 | 0.51 | 0.45 | 0.67 | 0.51 | 0.28 | 0.51 | 0.69 | 0.57 |

Table E1: Plagioclase Electron-Microprobe Analyses from MMA Basalts

| Sample: | 904-MR | 904-G | 911-MC1 | 911-MR1 | 911-MC2 | 911-MM2 | 911-MR2 | 911-MC3 | 911-G | 941-PC |
|---|---|---|---|---|---|---|---|---|---|---|
| Anal.#: | 11 | 12 | 13 | 14 | 15 | 16 | 17 | 18 | 19 | 20 |
| | wt.% | wt.% | wt.% | wt.% | wt.% | wt.% | wt.% | wt.% | wt.% | wt.% |
| SiO2 | 52.13 | 50.51 | 46.78 | 50.65 | 55.79 | 50.57 | 51.14 | 50.18 | 50.83 | 47.25 |
| Al2O3 | 28.99 | 29.89 | 33.14 | 28.88 | 26.46 | 29.37 | 28.19 | 28.57 | 29.02 | 32.06 |
| FeO* | 1.06 | 0.65 | 0.51 | 1.09 | 0.88 | 0.90 | 1.45 | 0.91 | 1.10 | 0.63 |
| MgO | 0.23 | 0.23 | 0.19 | 0.31 | 0.07 | 0.35 | 0.68 | 0.37 | 0.38 | 0.16 |
| CaO | 13.03 | 14.19 | 17.56 | 13.70 | 10.41 | 14.65 | 13.09 | 14.43 | 14.14 | 16.71 |
| Na2O | 4.11 | 3.51 | 1.75 | 3.96 | 5.60 | 3.47 | 3.91 | 3.36 | 3.51 | 1.98 |
| K2O | 0.16 | 0.11 | 0.03 | 0.14 | 0.23 | 0.10 | 0.12 | 0.10 | 0.10 | 0.05 |
| TOTAL | 99.71 | 99.09 | 99.96 | 98.73 | 99.44 | 99.41 | 98.58 | 97.92 | 99.08 | 98.84 |
| | IRON CALCULATED AS Fe2O3 (TOTAL) | | | | | | | | | |
| Si | 2.3800 | 2.3264 | 2.1558 | 2.3450 | 2.5317 | 2.3272 | 2.3670 | 2.3429 | 2.3434 | 2.1969 |
| Al | 1.5599 | 1.6225 | 1.7999 | 1.5759 | 1.4151 | 1.5930 | 1.5378 | 1.5722 | 1.5768 | 1.7568 |
| Fe+3 | 0.0405 | 0.0250 | 0.0197 | 0.0422 | 0.0334 | 0.0346 | 0.0561 | 0.0355 | 0.0424 | 0.0245 |
| Mg | 0.0157 | 0.0158 | 0.0131 | 0.0214 | 0.0047 | 0.0240 | 0.0469 | 0.0257 | 0.0261 | 0.0111 |
| Ca | 0.6374 | 0.7002 | 0.8670 | 0.6796 | 0.5061 | 0.7223 | 0.6491 | 0.7219 | 0.6984 | 0.8324 |
| Na | 0.3638 | 0.3134 | 0.1564 | 0.3555 | 0.4927 | 0.3096 | 0.3509 | 0.3042 | 0.3137 | 0.1785 |
| K | 0.0093 | 0.0065 | 0.0018 | 0.0083 | 0.0133 | 0.0059 | 0.0071 | 0.0060 | 0.0059 | 0.0030 |
| SUM | 5.0064 | 5.0098 | 5.0135 | 5.0278 | 4.9971 | 5.0167 | 5.0150 | 5.0083 | 5.0068 | 5.0032 |
| TETRA | 3.9803 | 3.9739 | 3.9753 | 3.9631 | 3.9802 | 3.9549 | 3.9610 | 3.9506 | 3.9626 | 3.9782 |
| X-CAT | 1.0261 | 1.0359 | 1.0382 | 1.0647 | 1.0169 | 1.0618 | 1.0540 | 1.0577 | 1.0442 | 1.0250 |
| | COMPOSITION (MOLE %) | | | | | | | | | |
| AN | 62.11 | 67.59 | 83.51 | 63.83 | 49.77 | 68.03 | 61.59 | 68.25 | 66.89 | 81.21 |
| AB | 35.45 | 30.26 | 15.06 | 33.39 | 48.45 | 29.16 | 33.29 | 28.76 | 30.05 | 17.41 |
| OR | 0.91 | 0.62 | 0.17 | 0.78 | 1.31 | 0.55 | 0.67 | 0.56 | 0.56 | 0.29 |

Table E1: Plagioclase Electron-Microprobe Analyses from MMA Basalts

| Sample: | 941-PR 21 | 941-MC 22 | 905-PC 23 | 905-PM 24 | 905-MC 25 | 905-G 26 | 963-PC 27 | 963-PM 28 | 963-PR 29 | 963-MC1 30 |
|---|---|---|---|---|---|---|---|---|---|---|
| | wt.% | wt.% | wt.% | wt.% | wt.% | wt.% | wt.% | wt.% | wt.% | wt.% |
| SiO2 | 51.11 | 49.71 | 52.03 | 51.82 | 52.19 | 53.79 | 49.52 | 48.40 | 48.04 | 48.57 |
| Al2O3 | 28.71 | 30.33 | 29.52 | 28.78 | 29.04 | 27.90 | 31.87 | 32.29 | 32.36 | 32.19 |
| FeO* | 1.03 | 0.71 | 0.68 | 0.75 | 0.72 | 0.74 | 0.52 | 0.52 | 0.65 | 0.53 |
| MgO | 0.34 | 0.18 | 0.15 | 0.18 | 0.16 | 0.15 | 0.19 | 0.19 | 0.21 | 0.17 |
| CaO | 13.44 | 14.72 | 13.40 | 13.00 | 13.02 | 11.95 | 16.35 | 16.72 | 16.97 | 16.56 |
| Na2O | 3.71 | 3.14 | 3.84 | 3.99 | 4.05 | 4.42 | 2.31 | 2.04 | 1.88 | 2.09 |
| K2O | 0.12 | 0.08 | 0.14 | 0.16 | 0.14 | 0.15 | 0.07 | 0.06 | 0.06 | 0.06 |
| TOTAL | 98.46 | 98.87 | 99.76 | 98.68 | 99.32 | 99.10 | 100.83 | 100.22 | 100.17 | 100.17 |
| | IRON CALCULATED AS Fe2O3 (TOTAL) | | | | | | | | | |
| Si | 2.3656 | 2.2979 | 2.3718 | 2.3876 | 2.3882 | 2.4556 | 2.2494 | 2.2157 | 2.2029 | 2.2232 |
| Al | 1.5661 | 1.6524 | 1.5860 | 1.5629 | 1.5662 | 1.5011 | 1.7062 | 1.7422 | 1.7489 | 1.7366 |
| Fe+3 | 0.0399 | 0.0274 | 0.0259 | 0.0289 | 0.0276 | 0.0283 | 0.0198 | 0.0199 | 0.0249 | 0.0203 |
| Mg | 0.0235 | 0.0124 | 0.0102 | 0.0124 | 0.0109 | 0.0102 | 0.0129 | 0.0130 | 0.0144 | 0.0116 |
| Ca | 0.6665 | 0.7290 | 0.6545 | 0.6418 | 0.6383 | 0.5845 | 0.7957 | 0.8201 | 0.8338 | 0.8122 |
| Na | 0.3329 | 0.2814 | 0.3394 | 0.3564 | 0.3593 | 0.3912 | 0.2034 | 0.1811 | 0.1671 | 0.1855 |
| K | 0.0071 | 0.0047 | 0.0081 | 0.0094 | 0.0082 | 0.0087 | 0.0041 | 0.0035 | 0.0035 | 0.0035 |
| SUM | 5.0015 | 5.0053 | 4.9960 | 4.9994 | 4.9987 | 4.9797 | 4.9914 | 4.9955 | 4.9955 | 4.9928 |
| TETRA | 3.9715 | 3.9777 | 3.9838 | 3.9794 | 3.9819 | 3.9850 | 3.9753 | 3.9778 | 3.9767 | 3.9801 |
| X-CAT | 1.0299 | 1.0276 | 1.0122 | 1.0200 | 1.0168 | 0.9947 | 1.0161 | 1.0176 | 1.0188 | 1.0127 |
| | COMPOSITION (MOLE %) | | | | | | | | | |
| AN | 64.71 | 70.95 | 64.66 | 62.92 | 62.78 | 58.76 | 78.31 | 80.59 | 81.84 | 80.19 |
| AB | 32.32 | 27.39 | 33.53 | 34.95 | 35.34 | 39.33 | 20.02 | 17.79 | 16.41 | 18.32 |
| OR | 0.69 | 0.46 | 0.80 | 0.92 | 0.80 | 0.88 | 0.40 | 0.34 | 0.34 | 0.35 |

Table E1: Plagioclase Electron-Microprobe Analyses from MMA Basalts

| Sample: | 963-MC2 31 | 963-MR2 32 | 963-G 33 | 961-MC1 34 | 961-MM1 35 | 961-MC2 36 | 961-MC3 37 | | | |
|---|---|---|---|---|---|---|---|---|---|---|
| | wt.% | wt.% | wt.% | wt.% | wt.% | wt.% | wt.% | wt.% | wt.% | wt.% |
| SiO2 | 49.01 | 47.97 | 48.32 | 48.53 | 49.64 | 51.35 | 47.89 | | | |
| Al2O3 | 32.55 | 32.44 | 32.10 | 31.62 | 32.02 | 29.37 | 31.57 | | | |
| FeO* | 0.55 | 0.63 | 0.65 | 0.61 | 0.58 | 0.68 | 0.65 | | | |
| MgO | 0.20 | 0.16 | 0.19 | 0.19 | 0.18 | 0.22 | 0.18 | | | |
| CaO | 16.97 | 17.16 | 17.04 | 16.19 | 16.04 | 13.75 | 15.91 | | | |
| Na2O | 1.89 | 1.80 | 1.85 | 2.50 | 2.61 | 3.68 | 2.49 | | | |
| K2O | 0.04 | 0.05 | 0.04 | 0.05 | 0.07 | 0.12 | 0.08 | | | |
| TOTAL | 101.21 | 100.21 | 100.19 | 99.69 | 101.14 | 99.17 | 98.77 | | | |
| | IRON CALCULATED AS Fe2O3 (TOTAL) | | | | | | | | | |
| Si | 2.2203 | 2.1994 | 2.2144 | 2.2337 | 2.2481 | 2.3585 | 2.2250 | | | |
| Al | 1.7379 | 1.7530 | 1.7338 | 1.7153 | 1.7091 | 1.5899 | 1.7287 | | | |
| Fe+3 | 0.0208 | 0.0242 | 0.0249 | 0.0235 | 0.0220 | 0.0261 | 0.0253 | | | |
| Mg | 0.0135 | 0.0109 | 0.0130 | 0.0130 | 0.0122 | 0.0151 | 0.0125 | | | |
| Ca | 0.8237 | 0.8430 | 0.8367 | 0.7984 | 0.7783 | 0.6766 | 0.7920 | | | |
| Na | 0.1660 | 0.1600 | 0.1644 | 0.2231 | 0.2292 | 0.3277 | 0.2243 | | | |
| K | 0.0023 | 0.0029 | 0.0023 | 0.0029 | 0.0040 | 0.0070 | 0.0047 | | | |
| SUM | 4.9845 | 4.9935 | 4.9896 | 5.0099 | 5.0029 | 5.0009 | 5.0125 | | | |
| TETRA | 3.9790 | 3.9766 | 3.9732 | 3.9725 | 3.9792 | 3.9745 | 3.9790 | | | |
| X-CAT | 1.0055 | 1.0169 | 1.0164 | 1.0375 | 1.0237 | 1.0264 | 1.0335 | | | |
| | COMPOSITION (MOLE %) | | | | | | | | | |
| AN | 81.92 | 82.90 | 82.32 | 76.96 | 76.03 | 65.92 | 76.63 | | | |
| AB | 16.51 | 15.74 | 16.17 | 21.50 | 22.39 | 31.93 | 21.70 | | | |
| OR | 0.23 | 0.29 | 0.23 | 0.28 | 0.40 | 0.68 | 0.46 | | | |

Table E1: Plagioclase Electron-Microprobe Analyses from MMA Basalts

| Sample: | 012-MC | 014-MC | 021-MC | 021-MR | 021-G | 029-MC | 041-PC | 041-PR | 041-MC | 042-MC |
|---|---|---|---|---|---|---|---|---|---|---|
| Anal.#: | 38 | 39 | 40 | 41 | 42 | 43 | 44 | 45 | 46 | 47 |
| | wt.% | wt.% | wt.% | wt.% | wt.% | wt.% | wt.% | wt.% | wt.% | wt.% |
| SiO2 | 50.40 | 51.03 | 51.12 | 52.05 | 55.57 | 53.17 | 47.52 | 49.63 | 51.88 | 47.56 |
| Al2O3 | 31.29 | 31.64 | 30.88 | 28.64 | 27.29 | 29.01 | 33.27 | 31.21 | 29.57 | 34.28 |
| FeO | 0.80 | 0.71 | 0.65 | 1.05 | 1.35 | 0.94 | 0.52 | 0.74 | 0.98 | 0.51 |
| MgO | 0.22 | 0.21 | 0.22 | 0.32 | 0.29 | 0.22 | 0.19 | 0.27 | 0.43 | 0.24 |
| CaO | 14.52 | 14.44 | 13.91 | 12.60 | 10.74 | 12.56 | 16.88 | 14.75 | 13.73 | 16.81 |
| Na2O | 3.73 | 3.77 | 3.98 | 4.62 | 6.04 | 4.91 | 2.38 | 3.54 | 4.09 | 2.25 |
| K2O | 0.05 | 0.10 | 0.11 | 0.10 | 0.20 | 0.14 | 0.05 | 0.09 | 0.14 | 0.07 |
| TOTAL | 101.01 | 101.90 | 100.87 | 99.38 | 101.48 | 100.95 | 100.81 | 100.23 | 100.82 | 101.72 |
| | IRON CALCULATED AS Fe2O3 (TOTAL) | | | | | | | | | |
| Si | 2.2824 | 2.2885 | 2.3130 | 2.3853 | 2.4836 | 2.3972 | 2.1696 | 2.2680 | 2.3492 | 2.1501 |
| Al | 1.6701 | 1.6723 | 1.6467 | 1.5469 | 1.4375 | 1.5415 | 1.7903 | 1.6810 | 1.5781 | 1.8265 |
| Fe+3 | 0.0303 | 0.0266 | 0.0246 | 0.0402 | 0.0505 | 0.0354 | 0.0199 | 0.0283 | 0.0371 | 0.0193 |
| Mg | 0.0149 | 0.0140 | 0.0148 | 0.0219 | 0.0193 | 0.0148 | 0.0129 | 0.0184 | 0.0290 | 0.0162 |
| Ca | 0.7045 | 0.6938 | 0.6743 | 0.6187 | 0.5143 | 0.6067 | 0.8257 | 0.7222 | 0.6661 | 0.8142 |
| Na | 0.3275 | 0.3278 | 0.3492 | 0.4105 | 0.5234 | 0.4292 | 0.2107 | 0.3137 | 0.3591 | 0.1972 |
| K | 0.0029 | 0.0057 | 0.0063 | 0.0058 | 0.0114 | 0.0081 | 0.0029 | 0.0052 | 0.0081 | 0.0040 |
| SUM | 5.0326 | 5.0288 | 5.0291 | 5.0293 | 5.0399 | 5.0329 | 5.0321 | 5.0368 | 5.0268 | 5.0276 |
| TETRA | 3.9828 | 3.9874 | 3.9844 | 3.9724 | 3.9715 | 3.9742 | 3.9798 | 3.9773 | 3.9644 | 3.9959 |
| X-CAT | 1.0498 | 1.0414 | 1.0447 | 1.0569 | 1.0684 | 1.0588 | 1.0523 | 1.0595 | 1.0623 | 1.0317 |
| | COMPOSITION (MOLE %) | | | | | | | | | |
| AN | 67.11 | 66.63 | 64.55 | 58.54 | 48.14 | 57.30 | 78.47 | 68.16 | 62.70 | 78.92 |
| AB | 31.20 | 31.48 | 33.42 | 38.84 | 48.99 | 40.54 | 20.02 | 29.60 | 33.80 | 19.12 |
| OR | 0.28 | 0.55 | 0.61 | 0.55 | 1.07 | 0.76 | 0.28 | 0.50 | 0.76 | 0.39 |

Table E1: Plagioclase Electron-Microprobe Analyses from MMA Basalts

| Sample: | O51-MC1 | O51-MR1 | O51-MC2 | C3-MC | C3-MR | C3-PC | C3-PM |
|---|---|---|---|---|---|---|---|
| Anal.#: | 48 | 49 | 50 | 51 | 52 | 53 | 54 |
| | wt.% | wt.% | wt.% | wt.% | wt.% | wt.% | wt.% |
| SiO2 | 47.63 | 49.47 | 49.93 | 47.35 | 50.36 | 46.35 | 47.22 |
| Al2O3 | 33.17 | 30.46 | 33.21 | 33.23 | 30.97 | 34.01 | 33.58 |
| FeO | 0.53 | 0.88 | 0.46 | 0.47 | 0.72 | 0.47 | 0.49 |
| MgO | 0.22 | 0.51 | 0.25 | 0.23 | 0.31 | 0.16 | 0.24 |
| CaO | 16.35 | 14.65 | 16.36 | 17.15 | 14.93 | 17.57 | 17.03 |
| Na2O | 2.48 | 3.46 | 2.28 | 0.05 | 0.13 | 0.05 | 0.05 |
| K2O | 0.08 | 0.12 | 0.07 | 2.03 | 3.42 | 1.64 | 2.05 |
| TOTAL | 100.46 | 99.55 | 102.56 | 100.51 | 100.84 | 100.25 | 100.66 |
| | IRON CALCULATED AS Fe2O3 (TOTAL) | | | | | | |
| Si | 2.1790 | 2.2773 | 2.2277 | 2.1758 | 2.3003 | 2.1363 | 2.1663 |
| Al | 1.7885 | 1.6528 | 1.7463 | 1.7997 | 1.6673 | 1.8475 | 1.8157 |
| Fe+3 | 0.0203 | 0.0339 | 0.0172 | 0.0181 | 0.0275 | 0.0181 | 0.0188 |
| Mg | 0.0150 | 0.0350 | 0.0166 | 0.0158 | 0.0211 | 0.0110 | 0.0164 |
| Ca | 0.8014 | 0.7226 | 0.7821 | 0.8444 | 0.7307 | 0.8676 | 0.8371 |
| Na | 0.2200 | 0.3088 | 0.1972 | 0.0045 | 0.0115 | 0.0045 | 0.0044 |
| K | 0.0047 | 0.0070 | 0.0040 | 0.1190 | 0.1993 | 0.0964 | 0.1200 |
| SUM | 5.0289 | 5.0373 | 4.9911 | 4.9771 | 4.9577 | 4.9814 | 4.9787 |
| TETRA | 3.9878 | 3.9639 | 3.9912 | 3.9935 | 3.9951 | 4.0019 | 4.0008 |
| X-CAT | 1.0411 | 1.0734 | 0.9999 | 0.9836 | 0.9626 | 0.9795 | 0.9779 |
| | COMPOSITION (MOLE %) | | | | | | |
| AN | 76.98 | 67.31 | 78.21 | 85.85 | 75.91 | 88.58 | 85.60 |
| AB | 21.13 | 28.77 | 19.73 | 0.45 | 1.20 | 0.46 | 0.45 |
| OR | 0.45 | 0.66 | 0.40 | 12.10 | 20.70 | 9.84 | 12.27 |

Table E2: Pyroxene Electron Microprobe Analyses of MMA Basalts

| Sample: | 883-MC | 883-MM | 883-MC | 911-G | 905-MC | 905-PC | 911-MC | 911-MM | 911-G |
|---|---|---|---|---|---|---|---|---|---|
| | wt.% | wt.% | wt.% | wt.% | wt.% | wt.% | wt.% | wt.% | wt.% |
| SiO2 | 50.38 | 51.58 | 51.86 | 50.29 | 49.71 | 52.04 | 48.56 | 49.42 | 49.24 |
| TiO2 | 1.40 | 0.91 | 0.55 | 1.18 | 0.93 | 1.10 | 1.49 | 1.13 | 1.85 |
| Al2O3 | 4.56 | 3.78 | 1.98 | 3.43 | 2.73 | 2.69 | 6.65 | 4.13 | 4.77 |
| Cr2O3 | 0.20 | 0.32 | 0.27 | 0.11 | 0.10 | 0.05 | 0.28 | 0.11 | 0.19 |
| FeO | 7.38 | 7.53 | 8.56 | 8.80 | 8.57 | 10.20 | 7.04 | 9.97 | 9.74 |
| MnO | 0.18 | 0.23 | 0.25 | 0.23 | 0.22 | 0.27 | 0.17 | 0.23 | 0.26 |
| MgO | 15.70 | 16.56 | 18.34 | 14.98 | 14.51 | 14.99 | 14.95 | 14.52 | 14.52 |
| CaO | 20.13 | 19.00 | 16.77 | 19.46 | 20.84 | 18.74 | 19.37 | 19.16 | 19.11 |
| Na2O | 0.28 | 0.29 | 0.19 | 0.23 | 0.30 | 0.30 | 0.25 | 0.25 | 0.25 |
| TOTAL | 100.21 | 100.20 | 98.77 | 98.71 | 97.91 | 100.38 | 98.76 | 98.92 | 99.93 |
| | CATIONS BASED ON 6 OXYGENS | | | | | | | | |
| Si | 1.8576 | 1.8940 | 1.9300 | 1.8917 | 1.8954 | 1.9272 | 1.8124 | 1.8659 | 1.8391 |
| Ti | 0.0388 | 0.0251 | 0.0154 | 0.0334 | 0.0267 | 0.0306 | 0.0418 | 0.0321 | 0.0520 |
| Al | 0.1982 | 0.1636 | 0.0868 | 0.1521 | 0.1227 | 0.1174 | 0.2925 | 0.1838 | 0.2100 |
| Cr | 0.0058 | 0.0093 | 0.0079 | 0.0033 | 0.0030 | 0.0015 | 0.0083 | 0.0033 | 0.0056 |
| Fe | 0.2276 | 0.2312 | 0.2664 | 0.2768 | 0.2733 | 0.3159 | 0.2197 | 0.3148 | 0.3042 |
| Mn | 0.0056 | 0.0072 | 0.0079 | 0.0073 | 0.0071 | 0.0085 | 0.0054 | 0.0074 | 0.0082 |
| Mg | 0.8628 | 0.9063 | 1.0173 | 0.8399 | 0.8246 | 0.8274 | 0.8317 | 0.8171 | 0.8083 |
| Ca | 0.7952 | 0.7475 | 0.6687 | 0.7843 | 0.8513 | 0.7436 | 0.7746 | 0.7751 | 0.7647 |
| Na | 0.0200 | 0.0206 | 0.0137 | 0.0168 | 0.0222 | 0.0215 | 0.0181 | 0.0183 | 0.0181 |
| TOTAL | 4.0116 | 4.0048 | 4.0141 | 4.0056 | 4.0262 | 3.9935 | 4.0044 | 4.0177 | 4.0102 |
| Mg/(Mg+Fe) | 0.7913 | 0.7967 | 0.7925 | 0.7521 | 0.7511 | 0.7237 | 0.7910 | 0.7219 | 0.7265 |

Table E2: Pyroxene Electron Microprobe Analyses of MMA Basalts

| Sample: | 911-PC | 911-PR | 961-G | 041-MC | 961-MC | 041-MM | 041-MC | 041-MC | 041-MC |
|---|---|---|---|---|---|---|---|---|---|
| | wt.% | wt.% | wt.% | wt.% | wt.% | wt.% | wt.% | wt.% | wt.% |
| SiO2 | 52.70 | 49.09 | 54.04 | 50.83 | 51.60 | 50.34 | 52.40 | 50.92 | 50.04 |
| TiO2 | 0.54 | 1.07 | 0.53 | 1.07 | 1.09 | 1.39 | 0.65 | 0.77 | 1.44 |
| Al2O3 | 2.23 | 4.75 | 1.40 | 3.71 | 3.25 | 4.74 | 2.14 | 2.74 | 5.07 |
| Cr2O3 | 0.25 | 0.30 | 0.08 | 0.09 | 0.16 | 0.14 | 0.16 | 0.18 | 0.02 |
| FeO | 8.06 | 7.23 | 8.82 | 7.58 | 6.72 | 7.68 | 6.31 | 6.13 | 8.29 |
| MnO | 0.21 | 0.22 | 0.28 | 0.17 | 0.14 | 0.14 | 0.13 | 0.13 | 0.22 |
| MgO | 20.67 | 16.16 | 19.18 | 15.21 | 15.45 | 15.48 | 16.24 | 15.95 | 16.03 |
| CaO | 14.47 | 18.84 | 15.58 | 19.92 | 21.11 | 19.67 | 21.47 | 21.50 | 18.71 |
| Na2O | 0.13 | 0.23 | 0.11 | 0.28 | 0.23 | 0.26 | 0.24 | 0.19 | 0.24 |
| TOTAL | 99.26 | 97.89 | 100.02 | 98.86 | 99.75 | 99.84 | 99.74 | 98.51 | 100.06 |
| | CATIONS BASED ON 6 OXYGENS | | | | | | | | |
| Si | 1.9303 | 1.8493 | 1.9717 | 1.8978 | 1.9066 | 1.8615 | 1.9338 | 1.9061 | 1.8474 |
| Ti | 0.0149 | 0.0303 | 0.0145 | 0.0300 | 0.0303 | 0.0387 | 0.0180 | 0.0217 | 0.0400 |
| Al | 0.0963 | 0.2109 | 0.0602 | 0.1633 | 0.1415 | 0.2066 | 0.0931 | 0.1209 | 0.2206 |
| Cr | 0.0072 | 0.0089 | 0.0023 | 0.0027 | 0.0047 | 0.0041 | 0.0047 | 0.0053 | 0.0006 |
| Fe | 0.2469 | 0.2278 | 0.2691 | 0.2367 | 0.2077 | 0.2375 | 0.1947 | 0.1919 | 0.2559 |
| Mn | 0.0065 | 0.0070 | 0.0087 | 0.0054 | 0.0044 | 0.0044 | 0.0041 | 0.0041 | 0.0069 |
| Mg | 1.1285 | 0.9074 | 1.0431 | 0.8464 | 0.8509 | 0.8532 | 0.8933 | 0.8899 | 0.8821 |
| Ca | 0.5679 | 0.7604 | 0.6090 | 0.7969 | 0.8357 | 0.7793 | 0.8489 | 0.8623 | 0.7401 |
| Na | 0.0092 | 0.0168 | 0.0078 | 0.0203 | 0.0165 | 0.0186 | 0.0172 | 0.0138 | 0.0172 |
| TOTAL | 4.0077 | 4.0189 | 3.9864 | 3.9994 | 3.9982 | 4.0038 | 4.0079 | 4.0160 | 4.0107 |
| Mg/(Mg+Fe) | 0.8205 | 0.7993 | 0.7949 | 0.7815 | 0.8038 | 0.7822 | 0.8210 | 0.8226 | 0.7751 |

Table E2: Pyroxene Electron Microprobe Analyses of MMA Basalts

| Sample: | 904-PC | 904-PR | 904-G7 | C3-MC | 904-MR | 051-PC | C3-MC |
|---|---|---|---|---|---|---|---|
| | wt.% | wt.% | wt.% | wt.% | wt.% | wt.% | wt.% |
| SiO2 | 53.88 | 49.46 | 50.70 | 50.82 | 50.03 | 51.55 | 51.20 |
| TiO2 | 0.40 | 1.49 | 0.91 | 1.09 | 0.93 | 0.58 | 0.70 |
| Al2O3 | 1.50 | 4.47 | 3.53 | 4.24 | 3.79 | 2.63 | 3.81 |
| Cr2O3 | 0.11 | 0.03 | 0.19 | 0.15 | 0.04 | 0.17 | 0.10 |
| FeO | 7.37 | 8.75 | 6.68 | 7.40 | 9.34 | 5.64 | 5.62 |
| MnO | 0.22 | 0.24 | 0.16 | 0.23 | 0.15 | 0.15 | 0.26 |
| MgO | 18.90 | 14.98 | 15.78 | 16.61 | 15.39 | 16.99 | 17.31 |
| CaO | 17.43 | 18.80 | 20.82 | 18.41 | 18.55 | 20.26 | 20.25 |
| Na2O | 0.12 | 0.29 | 0.21 | 0.23 | 0.22 | 0.18 | 0.16 |
| TOTAL | 99.93 | 98.51 | 98.98 | 99.18 | 98.44 | 98.15 | 99.41 |
| | CATIONS BASED ON 6 OXYGENS | | | | | | |
| Si | 1.9658 | 1.8621 | 1.8896 | 1.8817 | 1.8859 | 1.9226 | 1.8861 |
| Ti | 0.0110 | 0.0422 | 0.0255 | 0.0304 | 0.0264 | 0.0163 | 0.0194 |
| Al | 0.0645 | 0.1983 | 0.1551 | 0.1850 | 0.1684 | 0.1156 | 0.1654 |
| Cr | 0.0032 | 0.0009 | 0.0056 | 0.0044 | 0.0012 | 0.0050 | 0.0029 |
| Fe | 0.2249 | 0.2755 | 0.2082 | 0.2291 | 0.2944 | 0.1759 | 0.1731 |
| Mn | 0.0068 | 0.0077 | 0.0051 | 0.0072 | 0.0048 | 0.0047 | 0.0081 |
| | 0.0 | 0.0 | | | | | |
| Mg | 1.0278 | 0.8406 | 0.8766 | 0.9167 | 0.8647 | 0.9445 | 0.9504 |
| Ca | 0.6813 | 0.7583 | 0.8314 | 0.7304 | 0.7492 | 0.8096 | 0.7992 |
| Na | 0.0085 | 0.0212 | 0.0152 | 0.0165 | 0.0161 | 0.0130 | 0.0114 |
| TOTAL | 3.9937 | 4.0067 | 4.0122 | 4.0015 | 4.0110 | 4.0073 | 4.0161 |
| Mg/(Mg+Fe) | 0.8205 | 0.7532 | 0.8081 | 0.8000 | 0.7460 | 0.8430 | 0.8459 |

Pyroxene Electron Microprobe Analyses of MMA Basalts

| Sample: | 029-MC1 | 029-MC2 | 041-MC1 | 051-MC2 | 041-MC3 | 041-MC4 | 042-MC | 051-MC1 | 051-MC2 |
|---|---|---|---|---|---|---|---|---|---|
| | wt.% | wt.% | wt.% | wt.% | wt.% | wt.% | wt.% | wt.% | wt.% |
| SiO2 | 50.16 | 50.35 | 52.52 | 50.78 | 52.91 | 50.51 | 52.26 | 51.95 | 52.10 |
| TiO2 | 1.27 | 1.26 | 0.46 | 0.64 | 0.44 | 0.93 | 0.46 | 0.56 | 0.54 |
| Al2O3 | 3.66 | 3.40 | 1.89 | 2.96 | 1.86 | 5.75 | 2.05 | 2.39 | 2.50 |
| Cr2O3 | 0.29 | 0.28 | 0.39 | 0.33 | 0.39 | 0.22 | 0.46 | 0.48 | 0.62 |
| FeO | 10.22 | 9.72 | 5.40 | 7.36 | 5.83 | 6.75 | 5.56 | 5.47 | 5.40 |
| MnO | 0.0 | 0.0 | 0.0 | 0.0 | 0.0 | 0.0 | 0.0 | 0.0 | 0.0 |
| MgO | 16.14 | 15.99 | 17.69 | 18.39 | 18.20 | 16.07 | 17.90 | 17.81 | 17.81 |
| CaO | 17.91 | 18.34 | 21.48 | 18.02 | 20.60 | 18.99 | 20.66 | 21.06 | 21.13 |
| Na2O | 0.32 | 0.36 | 0.21 | 0.20 | 0.24 | 0.64 | 0.24 | 0.23 | 0.23 |
| TOTAL | 99.97 | 99.70 | 100.04 | 98.68 | 100.47 | 99.86 | 99.59 | 99.95 | 100.33 |
| | CATIONS BASED ON 6 OXYGENS | | | | | | | | |
| Si | 1.8676 | 1.8776 | 1.9257 | 1.8899 | 1.9294 | 1.8546 | 1.9227 | 1.9071 | 1.9050 |
| Ti | 0.0356 | 0.0353 | 0.0127 | 0.0179 | 0.0121 | 0.0257 | 0.0127 | 0.0155 | 0.0148 |
| Al | 0.1606 | 0.1494 | 0.0817 | 0.1298 | 0.0799 | 0.2488 | 0.0889 | 0.1034 | 0.1077 |
| Cr | 0.0085 | 0.0083 | 0.0113 | 0.0097 | 0.0112 | 0.0064 | 0.0134 | 0.0139 | 0.0179 |
| Fe | 0.3182 | 0.3031 | 0.1656 | 0.2291 | 0.1778 | 0.2073 | 0.1711 | 0.1679 | 0.1651 |
| Mn | 0.0 | 0.0 | 0.0 | 0.0 | 0.0 | 0.0 | 0.0 | 0.0 | 0.0 |
| Mg | 0.8957 | 0.8868 | 0.9668 | 1.0202 | 0.9892 | 0.8795 | 0.9816 | 0.9745 | 0.9707 |
| Ca | 0.7145 | 0.7328 | 0.8439 | 0.7186 | 0.8048 | 0.7471 | 0.8144 | 0.8283 | 0.8278 |
| Na | 0.0231 | 0.0260 | 0.0149 | 0.0144 | 0.0170 | 0.0456 | 0.0171 | 0.0164 | 0.0163 |
| TOTAL | 4.0238 | 4.0213 | 4.0226 | 4.0296 | 4.0214 | 4.0149 | 4.0220 | 4.0270 | 4.0254 |
| Mg/(Mg+Fe) | 0.7379 | 0.7457 | 0.8538 | 0.8166 | 0.8477 | 0.8093 | 0.8516 | 0.8530 | 0.8546 |

Table E3: Olivine Electron Microprobe Analyses from MMA Basalts

| Sample: | 883-PC | 883-PR | 883-MC | 883-MR | 883-G | 904-PC | 904-PR | 904-MC | 904-MR | 904-GC |
|---|---|---|---|---|---|---|---|---|---|---|
| | wt.% | wt.% | wt.% | wt.% | wt.% | wt.% | wt.% | wt.% | wt.% | wt.% |
| SiO2 | 39.31 | 39.09 | 39.52 | 38.70 | 38.88 | 39.00 | 38.82 | 38.38 | 37.89 | 39.48 |
| FeO | 17.67 | 18.23 | 17.39 | 19.05 | 17.46 | 18.08 | 18.24 | 17.70 | 17.34 | 17.66 |
| MnO | 0.25 | 0.33 | 0.27 | 0.30 | 0.27 | 0.32 | 0.31 | 0.26 | 0.28 | 0.30 |
| MgO | 42.24 | 41.73 | 41.81 | 40.47 | 42.10 | 41.71 | 41.79 | 42.25 | 42.38 | 42.48 |
| CaO | 0.35 | 0.35 | 0.32 | 0.37 | 0.31 | 0.30 | 0.38 | 0.32 | 0.29 | 0.37 |
| TOTAL | 99.82 | 99.73 | 99.31 | 98.89 | 99.02 | 99.41 | 99.54 | 98.91 | 98.18 | 100.29 |
| | CATIONS BASED ON 4 OXYGENS | | | | | | | | | |
| Si | 1.0019 | 1.0005 | 1.0103 | 1.0032 | 0.9990 | 1.0008 | 0.9963 | 0.9898 | 0.9842 | 1.0014 |
| Fe+2 | 0.3766 | 0.3902 | 0.3718 | 0.4130 | 0.3752 | 0.3880 | 0.3915 | 0.3818 | 0.3767 | 0.3746 |
| Mn | 0.0054 | 0.0072 | 0.0058 | 0.0066 | 0.0059 | 0.0070 | 0.0067 | 0.0057 | 0.0062 | 0.0064 |
| Mg | 1.6046 | 1.5920 | 1.5931 | 1.5637 | 1.6124 | 1.5953 | 1.5987 | 1.6241 | 1.6408 | 1.6060 |
| Ca | 0.0096 | 0.0096 | 0.0088 | 0.0103 | 0.0085 | 0.0082 | 0.0104 | 0.0088 | 0.0081 | 0.0101 |
| SUM | 2.9981 | 2.9995 | 2.9897 | 2.9968 | 3.0010 | 2.9992 | 3.0037 | 3.0102 | 3.0158 | 2.9986 |
| X-CAT | 1.9962 | 1.9990 | 1.9795 | 1.9936 | 2.0020 | 1.9985 | 2.0073 | 2.0204 | 2.0317 | 1.9972 |
| | COMPOSITION (MOLE %) | | | | | | | | | |
| FOR | 80.38 | 79.64 | 80.48 | 78.44 | 80.54 | 79.83 | 79.64 | 80.39 | 80.76 | 80.42 |
| FAY | 18.87 | 19.52 | 18.78 | 20.72 | 18.74 | 19.41 | 19.50 | 18.90 | 18.54 | 18.76 |
| CA | 0.48 | 0.48 | 0.44 | 0.52 | 0.43 | 0.41 | 0.52 | 0.44 | 0.40 | 0.50 |
| MN | 0.27 | 0.36 | 0.30 | 0.33 | 0.29 | 0.35 | 0.34 | 0.28 | 0.30 | 0.32 |
| TOTAL | 100.00 | 100.00 | 100.00 | 100.00 | 100.00 | 100.00 | 100.00 | 100.00 | 100.00 | 100.00 |

Table E3: Olivine Electron Microprobe Analyses from MMA Basalts

| Sample: | 904-GM | 904-GR | 905-PC | 905-PR | 905-MC | 905-G | 911-MC1 | 911-MR1 | 911-MC2 | 911-MM2 |
|---|---|---|---|---|---|---|---|---|---|---|
| | wt.% | wt.% | wt.% | wt.% | wt.% | wt.% | wt.% | wt.% | wt.% | wt.% |
| SiO2 | 38.23 | 36.92 | 37.57 | 37.99 | 37.67 | 37.95 | 39.40 | 38.77 | 39.50 | 39.15 |
| FeO | 20.00 | 26.57 | 23.89 | 26.37 | 23.89 | 23.85 | 15.24 | 18.07 | 15.33 | 15.91 |
| MnO | 0.30 | 0.36 | 0.37 | 0.41 | 0.38 | 0.44 | 0.24 | 0.32 | 0.22 | 0.21 |
| MgO | 40.08 | 33.90 | 37.68 | 35.33 | 36.95 | 36.71 | 44.15 | 41.73 | 44.37 | 43.81 |
| CaO | 0.33 | 0.31 | 0.31 | 0.32 | 0.29 | 0.29 | 0.34 | 0.35 | 0.33 | 0.35 |
| TOTAL | 98.94 | 98.06 | 99.82 | 100.42 | 99.18 | 99.24 | 99.37 | 99.24 | 99.75 | 99.43 |
| | CATIONS BASED ON 4 OXYGENS | | | | | | | | | |
| Si | 0.9960 | 1.0031 | 0.9892 | 1.0038 | 0.9977 | 1.0037 | 0.9980 | 0.9973 | 0.9969 | 0.9946 |
| Fe+2 | 0.4358 | 0.6037 | 0.5260 | 0.5827 | 0.5292 | 0.5275 | 0.3228 | 0.3887 | 0.3236 | 0.3380 |
| Mn | 0.0066 | 0.0083 | 0.0083 | 0.0092 | 0.0085 | 0.0099 | 0.0051 | 0.0070 | 0.0047 | 0.0045 |
| Mg | 1.5564 | 1.3728 | 1.4787 | 1.3914 | 1.4587 | 1.4471 | 1.6668 | 1.6000 | 1.6691 | 1.6588 |
| O.O | 0.0 | 0.0 | 0.0 | 0.0 | | | | | | |
| Ca | 0.0092 | 0.0090 | 0.0087 | 0.0091 | 0.0082 | 0.0082 | 0.0092 | 0.0096 | 0.0089 | 0.0095 |
| SUM | 3.0040 | 2.9969 | 3.0108 | 2.9962 | 3.0023 | 2.9963 | 3.0020 | 3.0027 | 3.0031 | 3.0054 |
| X-CAT | 2.0080 | 1.9938 | 2.0217 | 1.9924 | 2.0046 | 1.9927 | 2.0040 | 2.0054 | 2.0062 | 2.0109 |
| | COMPOSITION (MOLE %) | | | | | | | | | |
| FOR | 77.51 | 68.85 | 73.14 | 69.84 | 72.77 | 72.62 | 83.17 | 79.79 | 83.19 | 82.49 |
| FAY | 21.70 | 30.28 | 26.02 | 29.25 | 26.40 | 26.47 | 16.11 | 19.38 | 16.13 | 16.81 |
| CA | 0.46 | 0.45 | 0.43 | 0.45 | 0.41 | 0.41 | 0.46 | 0.48 | 0.44 | 0.47 |
| MN | 0.33 | 0.42 | 0.41 | 0.46 | 0.43 | 0.49 | 0.26 | 0.35 | 0.23 | 0.22 |
| TOTAL | 100.00 | 100.00 | 100.00 | 100.00 | 100.00 | 100.00 | 100.00 | 100.00 | 100.00 | 100.00 |

Table E3: Olivine Electron Microprobe Analyses from MMA Basalts

| Sample: | 911-MR2 | 911-MC3 | 911-MM3 | 941-MC1 | 941-MC2 | 941-MR2 | 961-G | 961-MC | 961-MR |
|---|---|---|---|---|---|---|---|---|---|
| | wt.% | wt.% | wt.% | wt.% | wt.% | wt.% | wt.% | wt.% | wt.% |
| SiO2 | 39.28 | 38.93 | 37.12 | 39.88 | 39.00 | 39.09 | 39.26 | 39.25 | 38.86 |
| FeO | 17.09 | 19.37 | 28.76 | 18.11 | 18.65 | 19.59 | 18.46 | 18.18 | 18.33 |
| MnO | 0.25 | 0.29 | 0.41 | 0.28 | 0.29 | 0.29 | 0.30 | 0.28 | 0.31 |
| MgO | 43.74 | 41.39 | 31.98 | 42.32 | 42.00 | 40.92 | 40.90 | 42.66 | 41.23 |
| CaO | 0.33 | 0.34 | 0.55 | 0.36 | 0.34 | 0.37 | 0.34 | 0.32 | 0.39 |
| TOTAL | 100.69 | 100.32 | 98.82 | 100.95 | 100.28 | 100.26 | 99.26 | 100.69 | 99.12 |
| | CATIONS BASED ON 4 OXYGENS | | | | | | | | |
| Si | 0.9906 | 0.9959 | 1.0108 | 1.0058 | 0.9948 | 1.0010 | 1.0097 | 0.9945 | 1.0017 |
| Fe+2 | 0.3604 | 0.4144 | 0.6549 | 0.3820 | 0.3979 | 0.4195 | 0.3970 | 0.3852 | 0.3951 |
| Mn | 0.0053 | 0.0063 | 0.0095 | 0.0060 | 0.0063 | 0.0063 | 0.0065 | 0.0060 | 0.0068 |
| Mg | 1.6441 | 1.5782 | 1.2980 | 1.5908 | 1.5969 | 1.5619 | 1.5678 | 1.6111 | 1.5840 |
| Ca | 0.0089 | 0.0093 | 0.0160 | 0.0097 | 0.0093 | 0.0102 | 0.0094 | 0.0087 | 0.0108 |
| SUM | 3.0094 | 3.0041 | 2.9892 | 2.9942 | 3.0052 | 2.9990 | 2.9903 | 3.0055 | 2.9983 |
| X-CAT | 2.0188 | 2.0082 | 1.9784 | 1.9885 | 2.0103 | 1.9979 | 1.9807 | 2.0110 | 1.9967 |
| | COMPOSITION (MOLE %) | | | | | | | | |
| FOR | 81.44 | 78.59 | 65.61 | 80.00 | 79.44 | 78.18 | 79.15 | 80.11 | 79.33 |
| FAY | 17.85 | 20.64 | 33.10 | 19.21 | 19.79 | 21.00 | 20.04 | 19.16 | 19.79 |
| CA | 0.44 | 0.46 | 0.81 | 0.49 | 0.46 | 0.51 | 0.47 | 0.43 | 0.54 |
| MN | 0.26 | 0.31 | 0.48 | 0.30 | 0.31 | 0.31 | 0.33 | 0.30 | 0.34 |
| TOTAL | 100.00 | 100.00 | 100.00 | 100.00 | 100.00 | 100.00 | 100.00 | 100.00 | 100.00 |

Table E3: Olivine Electron Microprobe Analyses from MMA Basalts

| Sample: | 021-MC1 | 021-MC2 | 012-MC1 | 012-MC2 | 029-MC1 | 029-MC2 | 029-MC3 | 041-MC1 | 041-MC2 | 042-MC1 |
|---|---|---|---|---|---|---|---|---|---|---|
| | wt.% | wt.% | wt.% | wt.% | wt.% | wt.% | wt.% | wt.% | wt.% | wt.% |
| SiO2 | 37.95 | 37.79 | 37.64 | 38.33 | 38.10 | 38.16 | 37.79 | 39.14 | 38.44 | 38.85 |
| Al2O3 | 0.0 | 0.0 | 0.32 | 0.06 | 0.0 | 0.0 | 0.01 | 0.02 | 0.0 | 0.0 |
| Cr2O3 | 0.03 | 0.03 | 0.02 | 0.03 | 0.03 | 0.01 | 0.02 | 0.01 | 0.02 | 0.02 |
| FeO | 20.91 | 20.85 | 20.67 | 22.35 | 22.96 | 22.23 | 23.50 | 15.83 | 16.54 | 16.19 |
| MnO | 0.42 | 0.37 | 0.39 | 0.42 | 0.43 | 0.47 | 0.45 | 0.33 | 0.34 | 0.31 |
| MgO | 38.72 | 38.28 | 39.56 | 38.23 | 37.99 | 38.30 | 37.38 | 43.58 | 42.91 | 42.04 |
| NiO | 0.12 | 0.14 | 0.0 | 0.14 | 0.12 | 0.12 | 0.09 | 0.10 | 0.11 | 0.12 |
| CaO | 0.34 | 0.35 | 0.36 | 0.46 | 0.31 | 0.34 | 0.30 | 0.42 | 0.38 | 0.40 |
| TOTAL | 98.49 | 97.81 | 98.96 | 100.02 | 99.94 | 99.63 | 99.54 | 99.43 | 98.74 | 97.93 |
| | CATIONS BASED ON 4 OXYGENS | | | | | | | | | |
| Si | 0.9990 | 1.0017 | 0.9851 | 0.9992 | 0.9970 | 0.9985 | 0.9960 | 0.9951 | 0.9890 | 1.0044 |
| Al | 0.0 | 0.0 | 0.0099 | 0.0018 | 0.0 | 0.0 | 0.0003 | 0.0006 | 0.0 | 0.0 |
| Cr | 0.0006 | 0.0006 | 0.0004 | 0.0006 | 0.0006 | 0.0002 | 0.0004 | 0.0002 | 0.0004 | 0.0004 |
| Fe+2 | 0.4603 | 0.4622 | 0.4524 | 0.4873 | 0.5025 | 0.4865 | 0.5180 | 0.3366 | 0.3559 | 0.3501 |
| Mn | 0.0094 | 0.0083 | 0.0086 | 0.0093 | 0.0095 | 0.0104 | 0.0100 | 0.0071 | 0.0074 | 0.0068 |
| Mg | 1.5192 | 1.5123 | 1.5432 | 1.4855 | 1.4818 | 1.4938 | 1.4685 | 1.6515 | 1.6455 | 1.6201 |
| Ni | 0.0025 | 0.0030 | 0.0 | 0.0029 | 0.0025 | 0.0025 | 0.0019 | 0.0020 | 0.0023 | 0.0025 |
| Ca | 0.0096 | 0.0099 | 0.0101 | 0.0128 | 0.0087 | 0.0095 | 0.0085 | 0.0114 | 0.0105 | 0.0111 |
| SUM | 3.0007 | 2.9980 | 3.0098 | 2.9995 | 3.0027 | 3.0014 | 3.0036 | 3.0045 | 3.0108 | 2.9953 |
| X-CAT | 2.0017 | 1.9964 | 2.0246 | 2.0003 | 2.0056 | 2.0029 | 2.0076 | 2.0094 | 2.0219 | 1.9909 |
| | COMPOSITION (MOLE %) | | | | | | | | | |
| FOR | 75.90 | 75.75 | 76.22 | 74.26 | 73.88 | 74.58 | 73.15 | 82.19 | 81.38 | 81.37 |
| FAY | 23.00 | 23.15 | 22.35 | 24.36 | 25.05 | 24.29 | 25.80 | 16.75 | 17.60 | 17.58 |
| CA | 0.48 | 0.50 | 0.50 | 0.64 | 0.43 | 0.48 | 0.42 | 0.57 | 0.52 | 0.56 |
| MN | 0.47 | 0.42 | 0.43 | 0.46 | 0.48 | 0.52 | 0.50 | 0.35 | 0.37 | 0.34 |
| TOTAL | 99.84 | 99.82 | 99.49 | 99.73 | 99.84 | 99.86 | 99.87 | 99.86 | 99.87 | 99.85 |

Table E3: Olivine Electron Microprobe Analyses from MMA Basalts

| Sample: | 042-MC2 | 051-PC | C3-MC1 | C3-MC2 |
|---|---|---|---|---|
| | wt.% | wt.% | wt.% | wt.% |
| SiO2 | 39.45 | 38.72 | 39.58 | 39.10 |
| Cr2O3 | 0.02 | 0.03 | 0.02 | 0.01 |
| FeO | 17.34 | 15.88 | 15.26 | 15.32 |
| MnO | 0.35 | 0.31 | 0.06 | 0.07 |
| MgO | 41.31 | 42.59 | 46.11 | 45.25 |
| NiO | 0.12 | 0.16 | 0.05 | 0.05 |
| CaO | 0.44 | 0.42 | 0.34 | 0.32 |
| TOTAL | 99.03 | 98.11 | 101.42 | 100.12 |
| | CATIONS BASED ON 4 OXYGENS | | | |
| Si | 1.0124 | 0.9987 | 0.9826 | 0.9842 |
| Cr | 0.0004 | 0.0006 | 0.0004 | 0.0002 |
| Fe+2 | 0.3722 | 0.3425 | 0.3168 | 0.3225 |
| Mn | 0.0076 | 0.0068 | 0.0013 | 0.0015 |
| Mg | 1.5802 | 1.6374 | 1.7062 | 1.6977 |
| Ni | 0.0025 | 0.0033 | 0.0010 | 0.0010 |
| Ca | 0.0121 | 0.0116 | 0.0090 | 0.0086 |
| SUM | 2.9874 | 3.0010 | 3.0172 | 3.0157 |
| X-CAT | 1.9749 | 2.0023 | 2.0347 | 2.0315 |
| | COMPOSITION (MOLE %) | | | |
| FOR | 80.01 | 81.78 | 83.85 | 83.57 |
| FAY | 18.84 | 17.11 | 15.57 | 15.87 |
| CA | 0.61 | 0.58 | 0.44 | 0.42 |
| MN | 0.39 | 0.34 | 0.06 | 0.07 |
| TOTAL | 99.85 | 99.80 | 99.93 | 99.94 |

## APPENDIX F : DESCRIPTION OF FRACTIONATION TESTS

***Element Ratio Diagrams***

It is possible to evaluate igneous differentiation processes such as fractional crystallization with element-ratio diagrams (Pearce, 1968) The weight percent oxide variation diagrams (Harker type) often employed to evaluate these processes have two major disadvantages that the element ratio diagrams do not have. The first is that wt% oxide data can not be easily related to mineral formulae. Secondly, the oxides plotted in a Harker diagram can show apparent variations even when they are not involved in the igneous process being tested. For example, large amounts of plagioclase fractionation from a basaltic melt would produce a variation in FeO vs. MgO space even though neither element is involved in the process. In an element-ratio diagram, the atomic abundances of element(s) are plotted, with both variables divided by a common denominator element which is not involved in the process being evaluated. This renders the variations in the plotted elements independant of variations in other elements. A recent demonstration of the theory and application of element-ratio diagrams to igneous petrology is provided by Nicholls *et al.* (1986), Russell and Nicholls (1987).

For the early crystallization history of basalts, potassium (K) behaves as a process-independent denominator element because it is not partitioned in trace amounts only into any of the early crystallizing phases. Selecting the appropriate combination of elements for the indices on each axis of the diagram can result in a series of rocks related by the fractionation of one or more phases to plot as a series of points defining a straight line with a slope of one.

For example, the removal of one molecule of olivine results in the loss of one atom of Si as well as one atom of either Fe or Mg from the magma. These removals produce horizontal and vertical shifts in the diagram, respectively. Furthermore, each shift is of equal magnitude, resulting in a slope of one. The

same shifts occur with the removal of any composition of plagioclas clinopyroxene.

Some minerals contain small amounts of elements substituting in the various mineral sites which are not involved in the index (eg. $TiO_2$ and $Al_2O_3$ in clinopyroxene). These minor substitutions do not produce significant deviations from the desired slope of one in the diagram, however.

Thus, a series of comagmatic lavas related by the removal of any combination of the three-phases of any composition would produce a series of points defining a line with a slope of one. If the samples have less than 2 or 3 % crystals, then they probably represent liquid compositions and the lines in the diagrams represent liquid lines of descent.

***The Mass-balance Fractionation Test***

The mass-balance calculations were made using the program XFRAC (Stout and Nicholls, 1977). The program determines the mass of the fractionating mineral phases that must be added to or subtracted from the composition of the proposed parent sample to best approximate the composition of the proposed daughter sample.

A total of 27 fractionation tests were made. A sample print-out of a mass-balance test is presented in figure F1 (test 27). The input data includes the composition of the proposed parent (P1491-1) and daughter (P1502-9) samples, as well as the compositions of the fractionating phases. Fractionating phases are inferred to be those present as equilibrium microphenocrysts and phenocrysts in the parent or the daughter sample. Phases present only as microlites are not entered and xenocryst compositions are not entered. Thus, only plagioclase and olivine are entered as fractionating phases in the tests between group two samples. In all the other tests, there are three fractionating phases; plagiocalse and clinopyroxene and

```
P1491-1(X) TO 1502-9(X)NO. OF SOLID PHASES  3

          PARENT    DERIVED      OLIV        PLAG        CPX
SIO2       49.52     50.16      38.55       48.70       51.38
TIO2        1.46      2.34        0.0         0.0        1.10
AL203      14.91     13.94        0.0       31.10        3.40
FE203        0.0       0.0        0.0         0.0         0.0
FEO         9.78     12.38      19.87        0.78        7.40
MNO         0.17      0.17       0.32         0.0        0.22
MGO         7.66      5.62      40.87        0.25       17.10
CAO        11.96      9.83       0.30       15.60       18.10
NA20        2.64      3.29        0.0        2.85        0.21
K20         0.42      0.69        0.0        0.08         0.0
P205        0.20      0.32        0.0         0.0         0.0
H20          0.0       0.0        0.0         0.0         0.0
TOTAL      98.72     98.74      99.91       99.36       98.91

                  ****************************************
                     SOLUTION TO MASS-BALANCE CALCULATION
                  ****************************************

                          100 GRAMS OF PARENT LIQUID + :
                                       -3.52  GRAMS OLIV
                                      -18.57  GRAMS PLAG
                                      -16.03  GRAMS CPX


                             EQUALS   61.87    GRAMS DERIVED
                  ----------------------------------------


          PARENT    DERIVED   OBS DIF   CALC DIF  RESIDUAL
SIO2    50.1621   50.8001    0.6380     0.5787   -0.0593
TIO2     1.4789    2.3699    0.8909     0.7253   -0.1656
AL203   15.1033   14.1179   -0.9854    -0.9821    0.0033
FE203     0.0       0.0       0.0        0.0        0.0
FEO      9.9068   12.5380    2.6312     2.7343    0.1031
MNO      0.1722    0.1722   -0.0000     0.0187    0.0187
MGO      7.7593    5.6917   -2.0676    -2.0895   -0.0219
CAO     12.1151    9.9554   -2.1596    -2.0640    0.0956
NA20     2.6742    3.3320    0.6578     0.7036    0.0458
K20      0.4254    0.6988    0.2734     0.2515   -0.0219
P205     0.2026    0.3241    0.1215     0.1236    0.0021
H20       0.0       0.0       0.0        0.0        0.0

                                       SUM RES:   0.5374
                                       SUM SQR:   0.0542

  THERE ARE     7 DEGREES OF FREEDOM
       SIGNIFICANCE LEVEL IS =    1.00000
PROBABILITY OF SSQ BY CHANCE =    0.00000

          ************************************************
```

Figure F1: Sample printout of program XFRAC (see text for description).

olivine.

The phase compositions entered are averages between the compositions observed in the parent and daughter samples (c.f. Appendix E). These are intended to represent the average composition crystallizing during fractionation. In tests where no mineral analyses for one sample were obtained, the analyses of another sample from the same chemical group were used.

The program calculates the combination of fractionating phases that produces the smallest sum of squares of residual differences (SRS) between oxide amounts of the calculated derived composition and the entered daughter composition. These differences are listed (in grams) below the input data (figure F1). This information, along with the SRS value, is listed in a table beneath the amounts of fractionating phases (figure F1). The final item on the output is a test of the significance of the result. It employs a 'chi squared' test to determine the statistical probability that the SRS was calculated by chance. In every successful test this probability was less than 1 in 100,000.

*Criteria for a Successful Test*

Three conditions had to be satisfied in order for a solution to be accepted and the hypothesis of fractional crystallization relating the samples maintained:

1. ***SRS < 0.10***

   The first three tests were run on duplicate analyses in order to determine what SRS value can be attributed to the analytical uncertainty in the major element analyses. The average SRS value observed in these three tests is about 0.05. Twice this amount (i.e. 0.10) was chosen as the maximum acceptable SRS value.

2. ***K and Ti Residuals < 0.05g out of 100g Parent Melt***

   In order to ascertain which of the remaining tests are valid, the residuals for the incompatible elements K and Ti were examined. These are both

incompatible elements (i.e. elements that are not incorporated in significant amounts in any of the observed fractionating phases). The enrichment in these elements reflects only the total amount of fractionation. Thus they are reliable indicators of what samples may or may not be related by fractional crystallization.

There are two other factors that contribute to the effectiveness of these elements as discriminants:

1. The range of observed concentrations is large; 0.40g to 0.75g for $K_2O$ and 1.30g to 2.35g for $TiO_2$
2. The $2\sigma$ analytical uncertainty for each element is low; 4.0% for $K_2O$ and 1.0% for $TiO_2$.

These analytical uncertainties account for residual differences less than 0.05g for each element.

The incompatible element phosphorus is not as effective a discriminant element as K or Ti because it has a smaller observed range of compositions and a large analytical uncertainty (6.5%). In some clinopyroxene microphenocrysts, Ti contents range from 0.50 wt% to 1.70 wt%. Thus, for solutions involving large (i.e. > 10g) of clinopyroxene formation (such as those relating 911 to the group 3 samples), larger residuals for Ti were accepted. Larger residuals were also accepted when the observed difference between parent and derived compositions was more than five times larger than the residual difference.

## APPENDIX F : DESCRIPTION OF FRACTIONATION TESTS

***Element Ratio Diagrams***

It is possible to evaluate igneous differentiation processes such as fractional crystallization with element-ratio diagrams (Pearce, 1968) The weight percent oxide variation diagrams (Harker type) often employed to evaluate these processes have two major disadvantages that the element ratio diagrams do not have. The first is that wt% oxide data can not be easily related to mineral formulae. Secondly, the oxides plotted in a Harker diagram can show apparent variations even when they are not involved in the igneous process being tested. For example, large amounts of plagioclase fractionation from a basaltic melt would produce a variation in FeO vs. MgO space even though neither element is involved in the process. In an element-ratio diagram, the atomic abundances of element(s) are plotted, with both variables divided by a common denominator element which is not involved in the process being evaluated. This renders the variations in the plotted elements independant of variations in other elements. A recent demonstration of the theory and application of element-ratio diagrams to igneous petrology is provided by Nicholls *et al.* (1986), Russell and Nicholls (1987).

For the early crystallization history of basalts, potassium (K) behaves as a process-independent denominator element because it is not partitioned in trace amounts only into any of the early crystallizing phases. Selecting the appropriate combination of elements for the indices on each axis of the diagram can result in a series of rocks related by the fractionation of one or more phases to plot as a series of points defining a straight line with a slope of one.

For example, the removal of one molecule of olivine results in the loss of one atom of Si as well as one atom of either Fe or Mg from the magma. These removals produce horizontal and vertical shifts in the diagram, respectively. Furthermore, each shift is of equal magnitude, resulting in a slope of one. The

same shifts occur with the removal of any composition of plagioclas clinopyroxene.

Some minerals contain small amounts of elements substituting in the various mineral sites which are not involved in the index (eg. $TiO_2$ and $Al_2O_3$ in clinopyroxene). These minor substitutions do not produce significant deviations from the desired slope of one in the diagram, however.

Thus, a series of comagmatic lavas related by the removal of any combination of the three-phases of any composition would produce a series of points defining a line with a slope of one. If the samples have less than 2 or 3 % crystals, then they probably represent liquid compositions and the lines in the diagrams represent liquid lines of descent.

***The Mass-balance Fractionation Test***

The mass-balance calculations were made using the program XFRAC (Stout and Nicholls, 1977). The program determines the mass of the fractionating mineral phases that must be added to or subtracted from the composition of the proposed parent sample to best approximate the composition of the proposed daughter sample.

A total of 27 fractionation tests were made. A sample print-out of a mass-balance test is presented in figure F1 (test 27). The input data includes the composition of the proposed parent (P1491-1) and daughter (P1502-9) samples, as well as the compositions of the fractionating phases. Fractionating phases are inferred to be those present as equilibrium microphenocrysts and phenocrysts in the parent or the daughter sample. Phases present only as microlites are not entered and xenocryst compositions are not entered. Thus, only plagioclase and olivine are entered as fractionating phases in the tests between group two samples. In all the other tests, there are three fractionating phases; plagiocalse and clinopyroxene and

```
P1491-1(X) TO 1502-9(X)NO. OF SOLID PHASES  3

          PARENT    DERIVED      OLIV        PLAG        CPX
SIO2      49.52     50.16        38.55       48.70       51.38
TIO2       1.46      2.34         0.0         0.0         1.10
AL2O3     14.91     13.94         0.0        31.10        3.40
FE2O3      0.0       0.0          0.0         0.0         0.0
FEO        9.78     12.38        19.87        0.78        7.40
MNO        0.17      0.17         0.32        0.0         0.22
MGO        7.66      5.62        40.87        0.25       17.10
CAO       11.96      9.83         0.30       15.60       18.10
NA2O       2.64      3.29         0.0         2.85        0.21
K2O        0.42      0.69         0.0         0.08        0.0
P2O5       0.20      0.32         0.0         0.0         0.0
H2O        0.0       0.0          0.0         0.0         0.0
TOTAL     98.72     98.74        99.91       99.36       98.91

                    ****************************************
                        SOLUTION TO MASS-BALANCE CALCULATION
                    ****************************************

                              100 GRAMS OF PARENT LIQUID + :
                                                  -3.52  GRAMS OLIV
                                                 -18.57  GRAMS PLAG
                                                 -16.03  GRAMS CPX


                                 EQUALS   61.87    GRAMS DERIVED
                                ----------------------------------------


            PARENT    DERIVED    OBS DIF   CALC DIF   RESIDUAL
SIO2      50.1621   50.8001     0.6380     0.5787    -0.0593
TIO2       1.4789    2.3699     0.8909     0.7253    -0.1656
AL2O3     15.1033   14.1179    -0.9854    -0.9821     0.0033
FE2O3      0.0       0.0        0.0        0.0        0.0
FEO        9.9068   12.5380     2.6312     2.7343     0.1031
MNO        0.1722    0.1722    -0.0000     0.0187     0.0187
MGO        7.7593    5.6917    -2.0676    -2.0895    -0.0219
CAO       12.1151    9.9554    -2.1596    -2.0640     0.0956
NA2O       2.6742    3.3320     0.6578     0.7036     0.0458
K2O        0.4254    0.6988     0.2734     0.2515    -0.0219
P2O5       0.2026    0.3241     0.1215     0.1236     0.0021
H2O        0.0       0.0        0.0        0.0        0.0

                                           SUM RES:   0.5374
                                           SUM SQR:   0.0542

  THERE ARE     7 DEGREES OF FREEDOM
       SIGNIFICANCE LEVEL IS =    1.00000
PROBABILITY OF SSQ BY CHANCE =    0.00000

          ************************************************
```

Figure F1: Sample printout of program XFRAC (see text for description).

olivine.

The phase compositions entered are averages between the compositions observed in the parent and daughter samples (c.f. Appendix E). These are intended to represent the average composition crystallizing during fractionation. In tests where no mineral analyses for one sample were obtained, the analyses of another sample from the same chemical group were used.

The program calculates the combination of fractionating phases that produces the smallest sum of squares of residual differences (SRS) between oxide amounts of the calculated derived composition and the entered daughter composition. These differences are listed (in grams) below the input data (figure F1). This information, along with the SRS value, is listed in a table beneath the amounts of fractionating phases (figure F1). The final item on the output is a test of the significance of the result. It employs a 'chi squared' test to determine the statistical probability that the SRS was calculated by chance. In every successful test this probability was less than 1 in 100,000.

*Criteria for a Successful Test*

Three conditions had to be satisfied in order for a solution to be accepted and the hypothesis of fractional crystallization relating the samples maintained:

1. ***SRS < 0.10***

   The first three tests were run on duplicate analyses in order to determine what SRS value can be attributed to the analytical uncertainty in the major element analyses. The average SRS value observed in these three tests is about 0.05. Twice this amount (i.e. 0.10) was chosen as the maximum acceptable SRS value.

2. ***K and Ti Residuals < 0.05g out of 100g Parent Melt***

   In order to ascertain which of the remaining tests are valid, the residuals for the incompatible elements K and Ti were examined. These are both

incompatible elements (i.e. elements that are not incorporated in significant amounts in any of the observed fractionating phases). The enrichment in these elements reflects only the total amount of fractionation. Thus they are reliable indicators of what samples may or may not be related by fractional crystallization.

There are two other factors that contribute to the effectiveness of these elements as discriminants:

1. The range of observed concentrations is large; 0.40g to 0.75g for $K_2O$ and 1.30g to 2.35g for $TiO_2$
2. The $2\sigma$ analytical uncertainty for each element is low; 4.0% for $K_2O$ and 1.0% for $TiO_2$.

These analytical uncertainties account for residual differences less than 0.05g for each element.

The incompatible element phosphorus is not as effective a discriminant element as K or Ti because it has a smaller observed range of compositions and a large analytical uncertainty (6.5%). In some clinopyroxene microphenocrysts, Ti contents range from 0.50 wt% to 1.70 wt%. Thus, for solutions involving large (i.e. > 10g) of clinopyroxene formation (such as those relating 911 to the group 3 samples), larger residuals for Ti were accepted. Larger residuals were also accepted when the observed difference between parent and derived compositions was more than five times larger than the residual difference.

## BIBLIOGRAPHY


ABBEY S. (1983) Studies in 'standard samples' of silicate rocks and minerals 1969-1982, Geological Survey of Canada, Paper 85-15,

BALLARD R. D., FRANCHETEAU J., JUTEAU T., RANGIN C., and NORMARK W. (1981) East Pacific Rise at 21°N: The volcanic, tectonic and hydrothermal processes of the central axis, *Earth Planet. Sci. Lett.*, 55, 1-10.

BENCE A. E., and ALBEE A. L. (1968) Emperical correction factors for the electron microanalysis of silicates and oxides, *J. Geol.*, 76, 382-403.

BOTROS M., and JOHNSON H. P. (*in review*) A model for the tectonic evolution of the Explorer-Northern Juan de Fuca Region.

BOUGAULT H., DMITRIEV L., SOBOLEV A., and NEEDHAM H. D. (*in review*) R. V. Akademik Boris Petrov: The 14°N zero age anomaly in the Atlantic from on board Nb/Zr determinations.

BYERLY G. R. (1980) The nature of differentiation trends in some volcanic rocks from the Galapagos Spreading Centre, *J. Geophys. Res.*, 85, 3797-3810.

CHASE R. L., SCOTT S. D., BARRETT T. J., HANNINGTON M. D., FOUQUET Y., and JUNIPER S. K. (1984) Tectonic framework and sulfide deposits of Southern Explorer Ridge, Northeastern Pacific Ocean, (abstr.) *EOS*, 65, 1111.

CHASE R. L., TIFFIN D. L., and MURRAY J. W. (1975) The Western Canadian continental margin. In *Canada's Continental Margins and Offshore Petroleum Exploration* (eds. C. J. Yorath, E. R. Parker and D. J. Glass), Caanadian Society of Petroleum Geologists, Memoir 4, Calgary, 701-721.

CHAYES F. (1956) The Holmes effect and the lower limit of modal analysis, *Miner. Mag.*, 31, 276-281.

CHRISTIE D. M., and SINTON J. M. (1981) Evolution of abyssal lavas along propagating segments of the Galapagos Spreading Centre, *Earth Planet. Sci. Lett.*, 56, 321-329.

COUSENS B. L. (1982) Major and trace element geochemistry of basalts from the Explorer area, Northeast Pacific Ocean, unpublished MSc thesis, University of British Columbia, 100p.

COUSENS B. L., CHASE R. L., and SCHILLING J. G. (1984) Basalt geochemistry of the Explorer Ridge area, Northeast Pacific Ocean, *Can. J. Earth Sci.*, 21, 157-170.

CRANE K. (1985) The spacing of rift axis highs: dependence upon diapiric processes in the underlying asthenosphere?, *Earth Planet. Sci. Lett.*, 72, 405-414.

CRANE K., AIKMAN F., EMBLEY R., HAMMOND S., MALAHOFF A., and LUPTON J. (1984) The distribution of geothermal fields on the Juan de Fuca Ridge, *J. Geophys. Res.*, 90, 727-744.

DAVIS E., CURRIE R., SAWYER R., and RIDDIHOUGH R. (1985) Juan de Fuca Ridge atlas: Illuminated-contour SEABEAM bathymetry (Explorer Ridge), Earth Physics Branch, Energy Mines and Resources Canada, Open File, 85-2.

DAVIS E. E., CURRIE R. G., SAWYER B. S., and HUSSONG D. M. (1984) Juan de Fuca Atlas: SeaMARC II Acoustic Imagery, Earth Physics Branch, Energy Mines and Resources Canada, Open File, 84-17,

DEER W. A., HOWIE R. A., and ZUSSMAN J. (1966) *An Introduction to Rock Forming Minerals* (Pub. Longman Group), 322-326.

DELANEY J. R., KARSTEN J. L., and HAMMOND S. R. (1986) Petrology and tectonics of the Juan de Fuca Ridge, in *A Symposium on the Juan de Fuca Ridge System* Geological Association of Canada, Pacific Section, Programme and Abstracts, 23-25.

ERLANK A. J., and KABLE E. J. D. (1976) The significance of incompatible elements in Mid-Atlantic Ridge basalts from 45°N with particular reference to Nb/Zr, *Contrib. Mineral. Petrol.*, 54, 281-291.

ELTHON D. (1984) Plagioclase buoyancy in oceanic basalts; chemical effects, *Geochim. Cosmoch. Acta*, 48, 753-768.

FRANCHETEAU J., and BALLARD R. D. (1983) The East Pacific Rise near 21°N, 13°N and 20°S: Inferences for along strike variablility of axial processes of the mid-ocean ridge, *Earth Planet. Sci. Lett.*, 64, 93-116.

GHIORSO M. S., CHARMICHAEL I. S. E., RIVERS M. L., and O. SACK. R. (1983) The Gibbs free energy of mixing of natural silicate liquids; an expanded regular solution approximation for the calculation of magmatic intensive variables, *Contrib. Mineral. Petrol.*, 84, 107-145.

GOVINDARAJU K. (1984) 1984 compilation of working values and sample descriptions for 170 international reference samples of mainly silicate rocks and minerals, *Geostandards Newsletter*, 8, 3-15.

GROVE T. L., and BENCE A. E. (1977) Experimental study of pyroxene-liquid interaction in quartz-normative basalt 15597, Proc. Eigth Lunar Sci. Conf., 1549-1579.

HEY R., DUENNEBIER F., and MORGAN W. J. (1980) Propagating rifts on mid-ocean ridges, *J. Geophys. Res.*, 85, 3647-3658.

HEY R. (1977) A new class of 'Pseudofaults' and their bearing on plate tectonics: a propagating rift model, *Earth Planet. Sci. Lett.*, 37, 321-325.

HEY R. N., and WILSON D. S. (1982) Propagating rift explanation for the tectonic evolution of the Northeast Pacific - Pseudomove, *Earth Planet. Sci. Lett.*, 58, 167-188.

HICKSON C. J., and JURAS S. J. (1986) Sample contamination by grinding, *Can. Mineral.*, 24, 585-589.

HICKSON C. J. (1986) Quaternary volcanic rocks of the Wells Gray-Clearwater Area, East Central British Columbia, unpublished PhD thesis, University of British Columbia.

HOLCOMB R. T., and CLAGUE D. A. (1983) Volcanic eruption patterns along submarine rift zones, in *Proceedings Oceans '83, Vol. II: Technical papers (IEEE and MTS)*, 787-790.

HYNDMAN R. D., ROGERS G. C., BONE M. N., LISTER C. R. B., WADE U. S., BARRETT D. L., DAVIS E. E., LEWIS T., LYNCH S., and SEEMANN D. (1978) Geophysical measurements in the region of the Explorer Ridge off Western Canada, *Can. J. Earth Sci.*, 15, 1508-1525.

IRVINE T. N., and BARRAGAR W. R. A. (1971) A guide to the chemical classification of the common volcanic rocks, *Can. J. Earth Sci.*, 15, 1508-1525.

JENKINS R., and DEVRIES J. L. (1967) *Practical X-ray Spectroscopy*, (Second Ed.), Springer Verlag, New York.

KUO L. C., and KIRKPATRICK R. J. (1982) Pre-eruption history of phyric basalts from DSDP legs 45 and 46: Evidence from morphology and zoning patterns in plagioclase, *Contrib. Mineral. Petrol.*, 79, 13-27.

LICHTMAN G. S., NORMARK W. R., and SPIESS F. N. (1984) Photogeologic study of a segment of the East Pacific Rise axis near 21°N latitude, *Geol. Soc. Amer. Bull.*, 95, 743-752.

LISTER C. R. B. (1972) On the thermal balance of a mid-ocean ridge, *Geophys. J. R. Ast. Soc.*, 26, 515-535.

MACDONALD K. C. (1982) Mid-ocean ridges: Fine scale tectonic, volcanic and hydrothermal processes within the plate boundary zone, *An. Rev. Earth Planet. Sci.*, 10, 155-190.

MALACEK S. J., and CLOWES R. M. (1978) Crustal structure near Explorer Ridge from a marine deep seismic survey, *J. Geophys. Res.*, 83, 5899-5912.

MALAHOFF A., HAMMOND S. R., EMBLEY R. W., CURRIE R. G., DAVIS E. E., RIDDIHOUGH R. P., and SAWYER B. S. (1984) Juan de Fuca Ridge atlas preliminary SEABEAM bathymetry sheets 102 G8, 9 and 16 (1:50,000 map), Earth Physics Branch, Energy Mines and Resources Canada, Open File, 85-1.

MARSHAL M., and COX A. (1971) Magnetism of pillow basalts and their petrology, *Geol. Soc. Amer. Bull.*, 82, 537-552.

MCDAONALD K. C., and FOX P. J. (1983) Overlapping spreading centres: new accretionary geometry on the East Pacific Rise, *Nature*, 302, 55-58.

MELSON W. G., VALLIER T. L., WRIGHT T. L., BYERLEY G. R., and NELEN J. A. (1976) Chemical diversity of abyssal volcanic glass erupted along the Pacific, Atlantic and Indain Ocean sea-floor spreading centres, in *The Geophysics of the Pacific Ocean Basin and its margin* (eds. Sutton *et al.*), Geophys. Monogr. Ser. 19, 351-367.

MENARD H. W. (1978) Fragmentation of the Farallon plate by pivoting subduction, *J. Geol.*, 86, 99-110.

MICHAEL P. J., and CHASE R. L. (*in review*) The influence of primary magma composition, $H_2O$ and pressure on mid-ocean ridge basalt differentiation, *Contrib. Mineral. Petrol.*.

MICHAEL P. J. (*in review*) Concentration, behaviour and storage of water in the suboceanic mantle, *Geochim. Cosmoch. Acta.*

MORGAN W. J. (1971) Convection plumes in the lower mantle, *Nature*, 230, 42-43.

NICHOLLS J., RUSSELL J. K., and STOUT M. Z. (1986) Testing magmatic hypotheses with thermodynamic modelling, in *Short Course in Mineral Melts* (ed. C. M. Scarfe), Mineralogical Association of Canada.

PEARCE J. A., and NORRY M. J. (1979) Petrogenetic implications of Ti, Zr, Y and Nb variations in volcanic rocks, *Contrib. Mineral. Petrol.*, 69, 33-47.

PEARCE T. H. (1968) A contribution to the theory of variation diagrams, *Contrib. Mineral. Petrol.*, 19, 142-157.

PERFIT M. R., and FORNARI D. J. (1983) Geochemical studies of abyssal lavas recovered by DSRV *Alvin* from Eastern Galapagos Rift, Inca Transform, and Ecuador Rift 3. Trace element abundances and petrogenesis, *J. Geophys. Res.*, 88, 10,551-10,572.

RAFF A. D., and MASON R. G. (1961) Magnetic survey off the west coast of North America, 40°N to 52°N, *Geol. Soc. Amer. Bull.*, 72, 1267-1270.

RHODES J. M., and DUNGAN M. A. (1979) The evolution of ocean-floor basaltic magmas, in *Deep Sea Drilling Results in the Atlantic Ocean: Ocean Crust*, Maurice Ewing Series, American Geophysical Union.

RIDDIHOUGH R. P. (1977) A model for recent plate interaction off Canada's wset coast, *Can. J. Earth Sci.*, 14, 384-396.

RIDDIHOUGH R. P. (1984) Recent movements of the Juan de Fuca plate system, *J. Geophys. Res.*, 89, 6980-6994.

RUSSELL J. K., and NICHOLLS J. (1987) Early crystalliazation history of alkali olivine basalts, Diamond Craters, Oregon, *Geochim. Cosmoch. Acta*, 51(1), 143-154.

RUSSELL J. K., and NICHOLLS J. (1985) Application of Duhem's theorum to the estimation of extensive and intensive properties of basaltic magmas, *Can. Mineral.*, 23, 479-488.

SCHILLING J. G., KINGSLEY R. H., and DEVINE J. D. (1982) 1. Spatial petrological and geochemical variations (83°W-101°W), *J. Geophys. Res.*, 87, 5593-5610.

SCHILLING J. G. (1973) Iceland mantle plume, geochemical evidence along Reykjanes Ridge, *Nature*, 242, 565-571.

SCOTT S. D., CHASE R. L., MICHAEL P. J., SHEA G. T., BARRETT T. J., GORTON M., M. HANNINGTON, and PETER J. (1985) Explorer Ridge and Tuzo Wilson Seamounts: Update, (abstr.) *EOS*, 66, 925.

SEEMANN D. A. (1982) Bathymetry off the coast of British Columbia (1:1,000,000 map), Earth Physics Branch, Energy Mines and Resources Canada, Open File, open file 82-85.

SINTON J. M., WILSON D. S., CHRISTIE D. M., HEY R. N., and DELANEY J. R. (1983) Petrologic consequences of rift propagation on oceanic spreading ridges, *Earth Planet. Sci. Lett.*, 62, 193-207.

SMITH D., and LINDSEY D. H. (1971) Stable and metastable augite crystallization trends in a single basalt flow, *Amer. Min.*, 56, No. 1-2, 225-233.

SPARKS R. S. J., and HUPPERT H. E. (1984) Density changes during fractional crystallization of basaltic magmas: fluid dynamic implications, *Contrib. Mineral. Petrol.*, 85, 300-309.

SRIVASTAVA S. P. (1973) Interpretation of gravity and magnetic measurements across the continental margin of British Columbia, Canada, *Can. J. Earth Sci.*, 10, 1664-1677.

STAKES D. S., SHERVAIS J. W., and HOPSON C. A. (1984) The Volcano-tectonic cycle or the FAMOUS and AMAR valleys, Mid-Atlantic Ridge (36°47'N): evidence from basalt glass and phenocryst compositional variations for a steady state magma chamber beneath the valley midsections, AMAR 3, *J. Geophys. Res.*, 89 no. B8, 6995-7028.

STAUDIGEL H., and BRYAN W. B. (1981) Contrasted glass and whole rock compostions and phenocryst redistribution, IPOD sites 417 and 418, *Contrib. Mineral. Petrol.*, 78(3), 255-262.

STOUT M. Z., and NICHOLLS J. (1977) Mineralogy and petrology of the Quaternary lavas from the Snake River Plain, Idaho, *Can. J. Earth Sci.*, 14, 2140-2156.

THOMPSON G., BRYAN W. B., BALLARD R., HAMURO K., and MELSON W. G. (1985) Axial processes along a segment of the East Pacific Rise, 10°-12°N, *Nature*, 318, 429-433.

TIFFIN D. L., and SEEMAN D. (1975) Bathymetric map of the continental margin of western Canada, *Geol. Surv. Can.*, Open file.

TUNNICLIFFE V., BOTROS M., DEBURGH M. E., DINET A., JOHNSON H. P., JUNIPER S. K., and MCDUFF R. E. (1986) Hydrothermal vents of the Explorer Region, Northeast Pacific, *Deep Sea Res.*, 33, 401-403.